

AALBORG UNIVERSITY

NANOBIOTECHNOLOGY

3RD AND 4TH SEMESTER

Development of an affinity-based
impedimetric biosensor using gold
screen-printed electrodes

Author:
Daniel-Stefan CRISTEA

Supervisors:
Leonid GUREVICH

June 3, 2021



**AALBORG
UNIVERSITY**



Faculty of Engineering and Science
Department of Materials and Production
Nanobiotechnology
Skjernvej 4A
9220 Aalborg
<http://www.mp.aau.dk/>

STUDENT REPORT

Title:

Development of an affinity-based impedimetric biosensor using gold screen-printed electrodes

Project:

Master thesis Project

Project period:

September 2020 - June 2021

Participants:

Daniel-Stefan Cristea

Supervisor:

Leonid Gurevich

Number of pages: 80

Appendix: 3

Ended 03-06-2021

Abstract:

In this report, the use of screen-printed electrodes as a biosensing platform was studied by electrochemical techniques. Different surface cleaning methods are compared and all the functionalization steps are characterised using electrochemical impedance spectroscopy (EIS) and cyclic voltammetry. Ferrocyanide redox couple and two ferrocene derivatives, namely ferrocenecarboxylic acid and 1-1'-ferrocenedimethanol, were used to study the faradaic behaviour of the biosensor. Synthesis of 11-mercaptoundecanoic acid and mixed 11-mercaptoundecanoic acid/6-mercapto-1-hexanol SAMs is performed from solution. An initial optimization step was required to minimize the damage produced by the solvent on the working electrode. Different incubation times and ethanol concentrations were tested. Anti-NGAL monoclonal antibodies are attached to the monolayer surface through a two-step coupling reaction utilizing EDC as a cross-linker and NHS as a catalyst. The etching effect of cyanide ions on gold electrodes is observed when EIS and CV were employed in ferro-/ferricyanide solution. The electrostatic interactions between the redox probes and the electrode surface at different steps during functionalization are determined to have a great impact on the recorded EIS spectra. Furthermore, calibration curves were obtained by plotting the changes in charge transfer resistance after incubation with different AG concentrations. The LOD, LOQ and the dynamic linear range are determined for two biosensing approaches.

LIST OF ABBREVIATIONS

AB	Antibody
AC	Alternating current
AKI	Acute kidney injury
AG	Antigen
BSA	Bovine serum albumin
CPE	Constant phase element
CV	Cyclic voltammetry
DC	Direct current
EIS	Electrochemical impedance spectroscopy
ELISA	Enzyme-linked immunosorbent assay
IDE	Interdigitated electrodes
OCP	Open cell potential
POC	Point-of-care
LOD	Limit of detection
MAB	Monoclonal antibody
MCH	6-Mercapto-1-hexanol
MUA	11-Mercaptoundecanoic acid
NGAL	Neutrophil gelatinase-associated lipocalin
RC	Resistor-capacitor circuit
RL	Resistor-inductor circuit
RLC	Resistor-inductor-capacitor circuit
SAM	Self-assembled monolayer
SPE	Screen-printed electrode
SPR	Surface plasmon resonance
ssDNA	Single stranded DNA
WE	Working electrode

CONTENTS

Preface	1
1 Introduction	2
1.1 Biosensors characteristics	3
1.2 Classification	4
1.2.1 Biocatalytic biosensors	4
1.2.2 Affinity biosensors	5
1.2.3 Optical biosensors	5
1.2.4 Electrochemical biosensors	7
1.3 Electrical impedance	8
1.3.1 Complex impedance: cartesian and polar forms	8
1.3.2 Series and parallel impedance combinations	12
1.3.3 EIS applied on biological systems	12
1.4 Impedance biosensors: design and applications	18
1.4.1 Lab-on-a-chip approach	18
1.5 Self assembled monolayers	20
1.5.1 Self assembly mechanism	21
1.6 Neutrophil gelatinase-associated lipocalin as a bio-marker of renal function	24
2 Materials and Methods	26
2.1 Materials	26
2.2 Surface treatment and chloridization of SPEs	27
2.3 Surface functionalization of gold SPEs	28
2.3.1 Development of 11-MUA SAMs and mixed 11-MUA/6-MCH SAMs	28
2.3.2 Carboxyl terminal groups activation reaction, blocking of surface active sites and MAB attachment	29
2.4 Electrochemical measurements	31
2.4.1 EIS measurements using potassium ferro-/ferricyanide redox couple	31
2.4.2 EIS measurements using ferrocene derivatives	32
2.4.3 CV measurements	33
3 Results and discussion	35
3.1 Characterization of the surface cleaning methods	35
3.2 Electrochemical characterization of gold AT and BT SPEs	37
3.2.1 Chloridization of the pseudo-reference silver electrode	37
3.2.2 Redox behaviour of potassium ferro-/ferricyanide and ferrocene analogues	38
3.2.3 Electrochemical active surface area measurements	40
3.3 Optimization and characterization of 11-MUA SAM and 11-MUA/6-MCH mixed SAM using BT SPEs	42
3.4 Biosensor characterization using ferro-/ferricyanide redox couple	47

3.4.1	11-MUA SAM NGAL-biosensor	47
3.4.2	11-MUA/6-MCH mixed SAM NGAL-biosensor	50
3.4.3	The etching effect of cyanide ions	52
3.5	Biosensor characterization using ferrocene derivatives	55
3.6	NGAL-biosensor calibration: LOD and linear-range	60
4	Conclusion	63
5	Future perspectives	65
	Bibliography	66
A	Appendix	73
A.1	Rationalization of complex numbers	73
A.2	Chloridization of the pseudo-reference silver electrode	73
A.3	Equivalent circuits and data fitting	74

PREFACE

The use of screen-printed electrodes as a possible platform for the rapid detection of biomarkers by electrochemical measurements was studied in this report. Lab work and experiments were conducted at Aalborg University in the Departments of Materials and Production at the Skjernvej campus. The report was developed by a master student, as a master thesis over the course of the academic year 2020-2021 in the masters program Nanobiochemistry. The report consists of a theory part presenting general information and the relevant literature within the studied field and an experimental part showcasing the materials and analytical methods used and the contribution of the student within the field.

The IEEE referencing style was used throughout the report where in-text citations are shown as numbers inside brackets at the end of the cited paragraph. Citations link to a reference list placed at the end of the report where each cited material is sorted based on its appearance in the text. An abbreviation list containing the most commonly used abbreviation is also available. Figures reprinted or adapted from materials available in literature such as books and scientific papers were used with permission from the publishers.

I would like to express my gratitude to my supervisor, Leonid Gurevich, for the useful discussions and remarks regarding this report and for his support throughout the year. Furthermore, I would like to acknowledge the help of Thor Pedersen and his helpful advice.

INTRODUCTION

In general terms, a biosensor is a bioanalytical system, designed to specifically detect analytes by means of target-ligand interaction. This definition is broadly accepted in modern literature yet following IUPAC recommendations a biosensor is a type of chemical sensor which in turn is "a device that transforms chemical information, ranging from the concentration of a specific sample component to total composition analysis, into an analytically useful signal". Moreover the term biosensor is reserved to "chemical sensors in which the recognition system utilises a biochemical mechanism" [1]. In short, a biosensor is a type of chemical sensor which uses biological molecules to determine specific analytes in a sample. The history of the biosensor starts in 1906 when M. Cremer proposed that the change in acid concentration in an aqueous solution determines a change in the measured potential of that solution. This would later translate into the pH scale being introduced and the development of the first pH sensor [2].

In recent years, there has been a steady increase in research, development and manufacturing of novel biosensors, mainly for use in clinical diagnosis of diseases and for identification of biomarkers such as hormones or proteins, which are specific for certain conditions or disorders. All biosensors integrate two key components: the recognition element (DNA, enzymes or antibodies), which is involved in capturing the target analyte and the transducer, which translates the ligand-analyte complex formation into a signal that can be further processed and quantified. Biosensors are part of an important research topic that covers many areas, such as medical research, environmental surveillance, monitoring of biochemical processes, pollutants control etc. This subject has seen a steady increase in research interest since the last decade, with over 400 books and publications approaching this topic today. The increase in research comes from the possibility of applying the above-mentioned concepts of biosensing into developing a sensing platform able to detect any number of specific molecules, chemical products or contaminants. Some other key features of biosensors are the concept of miniaturization which seeks to reduce production costs while also requiring less sample volume and reagents. In diagnosis, biosensors are desirable since they can be used in operations at the point-of-care (POC), where fast results are desired [3], [4].

While biosensors excel in identifying analytes in pure samples, the difficulty arises when complex samples are used. This type of limitation is the main focus of current research which seeks to create more sensitive biosensors by eliminating non-specific interactions when using complex samples such as blood or urine. Biosensors regeneration is another area of great interest in the current research which seeks to further reduce the costs of operation by making biosensors reusable. Successful biosensor designs already exist under the form of commercially available biosensors used primarily in biomedical monitoring systems, in quality control and quality assurance in the food industry and as disposable biosensors for home use under the shape of pregnancy tests and glucose monitoring units [3], [5].

1.1 Biosensors characteristics

The general performance of a biosensor can be assessed by the experimental determination of a set of characteristics. This enables comparison between different immobilisation methods which might enhance the response of the sensor. Different sensing platforms can also be compared unless different performance criteria is used. In the case of immunosensors, specific performance indicators are commonly used such as the capture capacity which determines the yield of the overall bound biomolecules by measuring their specific activity. This is a way to determine the amount of surface active biomolecules compared to the total amount of immobilized biomolecules. This value is usually around 0.3 with a maximum of 1 which is hardly ever reached. The importance of determining this attributes comes from the possibility to identify weak spots or flaws in the biosensing design and to remedy the limiting factors [1], [6]. Standard performance criteria used to define most analytical systems and biosensors will be further detailed.

Selectivity is an important trait for all analytical systems. In biosensing terms, *selectivity* measures the degree of non-specific interactions, which ideally should be non-existent. A sensor with high *selectivity* would not produce any measurable signal in the absence of the target analyte. The response of the sensor should strictly correlate the concentration of the target analyte with the produced signal and should not be interfered by the presence of other molecules. This attribute can be enhanced by the use of antifouling agents. In the case of immunosensors, sandwich assays using capture and detection antibodies, which limit the chances of non specific interactions can increase *selectivity*. Impedimetric label-free immunosensors can not distinguish between specific and non-specific interactions [1], [3], [2], [7], [6]. The high selectivity of such sensors comes from the innate specificity of the antibodies. For bacteria or cell based biosensors *selectivity* is reduced [1]. Two methods to assess the degree of *selectivity* can be used. In the first method, calibration curves of different interfering agents concentrations are compared with standard curves obtained in the presence of the target analyte in pure samples. In the second method, different concentrations of the interfering substance is added to sample already containing the target analyte "at its mid-range of the expected value" [1]. In the first scenario selectivity is expressed as the ratio of signal with only the analyte alone and the signal with only interfering agent, both at equal concentration. For the first method, *selectivity* is obtained as the percentage of response variation [1].

The *sensitivity*, *limit of detection (LOD)*, *limit of quantitation (LOQ)* and *dynamic range* are obtained after the biosensor is calibrated. Calibration is done by plotting the background-corrected response of the biosensor at different analyte concentrations (usually a successive dilution of the target analyte). The *sensitivity* of the biosensor can be calculated from the slope of the linear region obtained in the calibration step. In literature, different terms are explained in a way that creates confusion, yet it is recommended to follow IUPAC terminology in this situation. According to IUPAC, *LOD* is the lowest analyte concentration which could be differentiated from the response to a blank solution/sample. On the other hand, *LOQ* sets the limit above which all response measurement should be treated with confidence. *LOQ* represent the minimum analyte concentration at which its response can be detected quantitatively. Sometimes *LOD* and *LOQ* could share the same value, yet *LOQ* is expected to be at least 10x the equivalent response of a blank sample making *LOQ* less prone to measurement errors or false positives. The performance criteria for an *LOQ* value could be selected to be more rigorous or flexible depending on the sensor performance

[1], [8]. The *dynamic range* is representative of the standard curve and represents the lower and upper limits for which different concentrations of analyte can be distinguished. In the case of the *LOD*, it could lay outside the linear range while the lower limit of the dynamic range should be within the linear range. This value gives the resolution of the biosensor. The *dynamic range* is used in biosensing when quantitative measurements are desired alongside analyte detection. [3].

The *stability* of a biosensor is an important trait that measures the susceptibility to other disturbances during operation. It is a measure of performance and high stability is expected in biosensing applications. *Stability* affects the *reproducibility* of a given measurement. A highly stable platform would give reproducible results in the same environmental conditions [1], [2].

1.2 Classification

Biosensors can be classified either by the type of biomolecules (enzymes, DNA, antibodies) integrated into the probing layer or by the transduction (optical, electrochemical) principle embedded in the sensor. By differentiating the recognition elements used in biosensing, biosensors can be divided into biocatalytic and affinity-based biosensors. The most common biorecognition elements used in biosensing are antibodies, enzymes, cells and nucleic acids. Protein and genetic engineering further developed the branch of biosensing by enabling the synthesis of peptides and oligonucleotide aptamers with enhanced affinity and specificity. While antibodies and nucleic acids require robust signal transduction in order to attain a measurable signal, enzymes on the other hand can be used for both recognition and signal transduction due to their inherited catalytic activity. Two types of biosensors making use of the aforementioned recognition elements will be further described [5], [7].

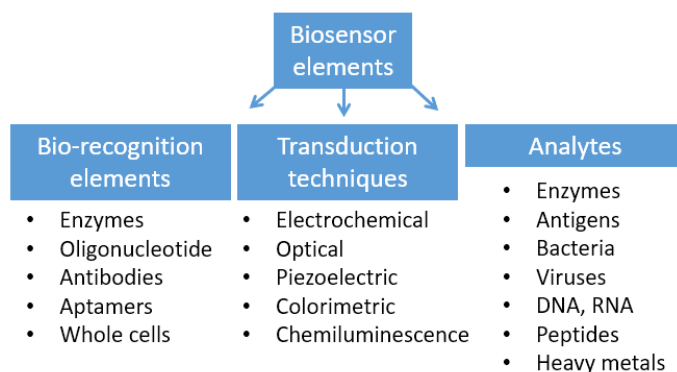


Figure 1.1: Some of the most widely used bio-recognition elements and transduction methods in biosensing. Adapted from [7] with permission from Elsevier.

1.2.1 Biocatalytic biosensors

Also known as enzyme-based biosensors were first introduced by Leland C. Clark and further developed by Updike and Hicks in 1967 [9]. Following their research, different recognition elements with biocatalytic activity were successfully used, such as whole cells or tissue for bio-activity monitoring. The working principle of such a biosensor is derived from the ability of enzymes to specifically recognize and bind the substrate molecule. The product obtained upon the enzyme-substrate interaction can be used

in signal transduction by either colorimetric assays or by electrochemical measurements. Enzymes also act as catalysts, increasing reaction rate which can be further characterized in terms of kinetics [10]. Some enzyme-based biosensors have been commercially available for quite a long time, such as the amperometric glucose biosensors available under the form of glucose pens or glucose display. By today's standards, the glucose biosensor is considered a mature and successful platform yet outgoing research still provides incremental improvements, mainly regarding packaging, shelf-life, sample handling and preparation. One of the first experiments to closely resemble a modern glucose biosensor was carried out by Lelan C. Clark in 1962. By using a glucose oxidase modified platinum electrode, Clark was able to indirectly measure a glucose solution concentration. Glucose reacts with glucose oxidase to produce gluconic acid; following this reaction glucose oxidase is reduced. The reduced form of the enzyme reacts with surrounding oxygen atoms to produce hydrogen peroxide and the oxidized form of the enzyme (natural state). The newly oxidized glucose oxidase can further react with other glucose molecules, maintaining the oxidation/reduction cycle, reacting with more oxygen if the glucose concentration is high. The accumulation of hydrogen peroxide increases when glucose concentration is low [2], [11], [12].

1.2.2 Affinity biosensors

Are part of an emerging group of biosensors that uses a wide range of biomolecules as recognition elements. The most common used biomolecules are antibodies, oligonucleotides, aptamers (DNA, RNA or proteins) and membrane proteins. Antibodies promote strong binding, they form stable complexes and have high selectivity under the right circumstances, which makes them the most widely used probes in so-called immunosensors. As in immunoassays, antibodies used in immunosensors are covalently attached to a solid substrate, in this case, the transducer. Different immobilization techniques have been developed over the years such as the silane coupling on glass substrates or SAMs (thiol-gold chemistry) mediated coupling on metal substrates [7]. One benefit of using ABs over other biorecognition elements is the high binding constant (K) that ABs have which promotes strong affinity and high selectivity. Oligonucleotides can also be used either to identify a complementary sequence (DNA hybridization) or under the form of aptamers selected from a large pool of random sequence DNA segments. DNA or RNA aptamers have specific a 3D structure, forming binding sites or recognition sites while ssDNA or RNA fragments rely on complementary base-pairing to the target oligonucleotide structure. Notable transduction techniques used in immunosensors include, but are not limited to, electrochemical, optical, microgravimetric and thermometric measurements [3], [10]

Biosensors can also be divided and classified depending on the signal transduction method that they integrate. There are many types of possible signal transduction methods used in conjunction with the aforementioned biorecognition elements. A shortlist of common transduction platforms used in biosensing is presented in fig. 1.1. To begin with, electrochemical biosensors will be further described since they are the main topic of this report followed by the optical sensing approach since the two of them are often described as having quite low detection limits and are frequently compared in this regard [7].

1.2.3 Optical biosensors

An additional important group of biosensing devices are optical biosensors. This type of biosensor takes advantage of how electromagnetic radiation interacts with a

biofunctionalized metal surface to achieve low LOD and high sensitivity. Different approaches for measuring an optical biosensor response can be applied, such as light absorption measurements or photometric measurements based on changes in light intensity before and after the sensing phase. There is a high degree of complexity when it comes to designing an optical biosensor and a high number of variations do exist.

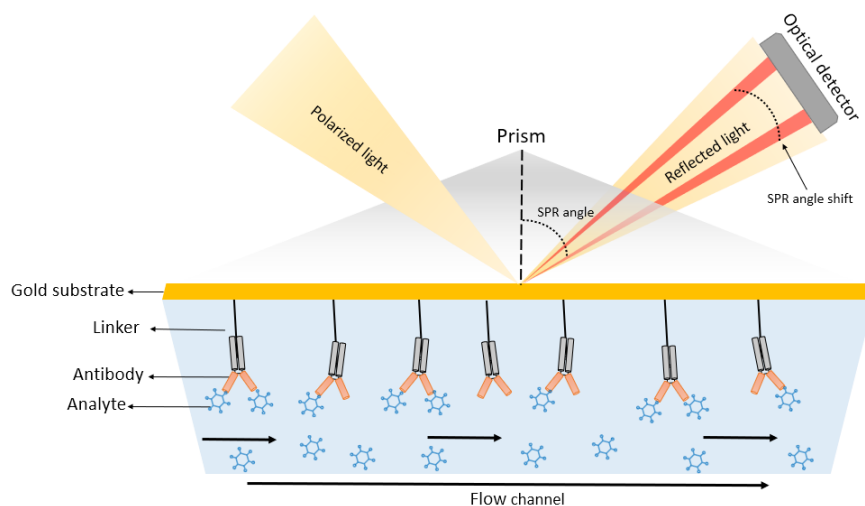


Figure 1.2: Schematic overview of an SPR biosensor. Antibodies are covalently attached to the surface of a gold-coated glass prism through an intermediate linker molecule. The antigen (analyte) is supplied through the help of a flow channel, on the biofunctionalized side of the prism. By shining polarized light through the glass prism, small changes in reflectivity can be noticed in the presence of the analyte. Adapted from [13] under the terms of Creative Commons CC BY license.

One common optical transduction method is the surface plasmon resonance (SPR). SPR occurs at the surface of metals such as gold when the incident electromagnetic wave is absorbed and re-emitted by the non-localized conduction electrons in the free electron gas. The adsorption profile of each metal is dependent on the size and the shape of the metal particles. In other words, SPR is characterised as the collective oscillation of conduction electrons at a metal-dielectric interface. In biosensors design, gold and silver nanoparticles can be used as transducer elements. By confining the surface plasmon in such a small area the so-called localised surface plasmon occurs, when the incoming incident light is of a higher wavelength than the nanoparticle dimensions. This leads to the excitation of conducting electrons which start to oscillate in different modes (dipole, quadrupole). An easy portrait of an SPR based optical biosensor is that of a thin gold chip onto which biomolecules are physically absorbed or covalently attached to an anchoring molecule. The whole complex is integrated into a microfluidics system. The shift in reflectivity is measured by shining a polarized light beam at a specific angle through a glass prism on the surface of the gold plate as presented in fig. 1.2. Reflectivity is then measured to assess the biosensor activity. Changes in reflectivity are observed when the analyte binds onto the biofunctionalized gold plate. SPR alongside other optical techniques enables quick, direct and sensitive label-free detection for a broad range of biomolecules and it is currently employed in a number of commercially available biosensing platforms such as the fully automated SPR sensors designed and produced by *BIACORE*[©] [7], [11].

1.2.4 Electrochemical biosensors

Electrochemical detection is a widely employed transduction method based on real-time monitoring of the electron transfer rate at the surface of the biosensor for faradaic driven transduction or the changes in capacitance for non-faradaic electrochemical biosensors. Electrochemical measurements are performed in the presence of redox-active species such as ferri/ferrocyanide or ferrocene for faradaic based sensors. The working principle of a faradaic electrochemical biosensor can be seen in fig. 1.3. The electrochemical measurements are carried out in an electrochemical cell using a standard three-electrode system composed of the reference electrode (platinum, carbon or silver/silver chloride), working electrode (gold, silver, carbon) and counter electrode (usually the same material as the working electrode). Electrochemical biosensors are suitable for POC operations since the measurable quantities such as the change in surface impedance or capacitance are sensitive enough to work with low sample volumes (μl) while maintaining their reliability. Electrochemical measurements are also characterized by having a low detection limit (LOD) while requiring very little sample preparation and reagents. Bryan et al. [14] were successful in designing an electrochemical biosensor for identifying a cardiovascular disease biomarker based on changes in R_{ct} with the LOD of 176 pM which is equivalent to $19\mu\text{g/ml}$ of C-reactive protein in the blood. Such a sensitive platform can prove suitable in identifying sparse but important biomarkers for certain disorders which might slip undetected by conventional laboratory techniques which in turn require expensive equipment, reagents and trained personnel. Different quantities can be measured by the use of voltammetry, amperometry or impedimetric methods [3], [15].

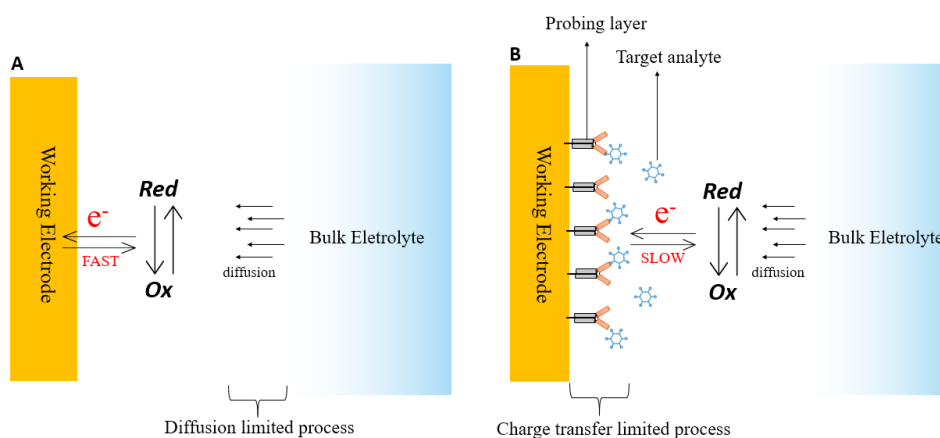


Figure 1.3: Schematic overview of an electrochemical biosensor. An unmodified electrode immersed in an electrolytic solution containing redox-active species (A). After applying a potential equal to the redox potential of the probe, charge transfer occurs at the interface. Assuming an equilibrium reaction under an ideal thermodynamic state, the limiting factor is the rate of diffusion of the bulk electrolyte to the interface. (B) An antibody modified electrode under the same conditions. The bio-layer hinders the electron transfer rate resulting in a charge transfer limited process. This behaviour is specific for faradaic driven biosensors.

Adapted from [7] with permission from Elsevier.

Most commonly cyclic voltammetry is used by applying a scanning potential to the counter electrode while measuring the current at the biofunctionalized (working) electrode. Upon antigen-antibody complex formation, a change in current is observed at the working electrode. Usually, the current decreases as a consequence of the analyte

binding to the probe layer, increasing the surface resistance while the electron transfer rate decreases. This behaviour is easily observed in a cyclic voltammogram when looking at the oxidation and reduction peaks or at the reduction in cathodic or anodic currents. The main takeaway of this method is that the antigen-antibody (AG-AB) complex formation limits the redox potential of the cell. Electrochemical impedance spectroscopy (EIS) is another powerful technique mainly used in immunosensors. It is used to probe the interfacial electrochemical properties of the working electrode by measuring the decrease in electron transfer rate at the electrode surface. The change in surface impedance is proportional to the concentration of the analyte. EIS relies on measuring the capacitive and resistive properties of the modified electrode surface by applying an AC potential to the system while varying the frequency over a broad range [10], [11]. Furthermore, electrochemical biosensors can take advantage of label-free detection, which further simplifies the system without affecting the LOD or sensitivity. While labelling proves to be useful especially in colorimetric or gene-specific APA sensors, in electrochemical biosensing it is not required since the intrinsic physical properties of the sensor, such as the change in impedance, can be easily detected. Label-free operation for an impedance immunosensor was demonstrated by Cecchetto et al. [16] by detecting the NS1-biomarker, a dengue specific protein, in serum by EIS measurements. In some cases, as for Flaviviruses detection (Dengue and Zika viruses), labelling proves destructive by hindering the AG-AB interaction. This proves that EIS and other electrochemical techniques are robust enough to detect low analyte concentrations despite missing labelling. The main drawback of this type of biosensors is the inability to reliably regenerate the probe layer making this biosensor suitable for single-use scenarios only. There have been attempts to regenerate the biorecognition layer of different electrochemical biosensors which mainly focuses on pH shock, the use of glycine/HCl solutions and detergents to overcome the binding energy of the complex, with moderate success [5], [14], [17], [18].

1.3 Electrical impedance

1.3.1 Complex impedance: cartesian and polar forms

The notion of electrical impedance is derived from the concept of electrical resistance, which in short can be described as the ability of an element within an electrical circuit to oppose (resist) the flow of electrical current. Electrical resistance is defined as the ratio between the applied voltage (\mathbf{V}) and current flow (\mathbf{I}) through a conductor. This relationship is mathematically expressed in eq. (1.1) also known as Ohm's law:

$$\frac{V}{I} = R \quad (1.1)$$

While Ohm's law can successfully portray the concept of resistance, it is considered somewhat limited as it only applies to a single circuit element, the resistor in DC circuits. With the current advancements in electronics, more complex circuits have become the new standard. As resistance is independent of the frequency of the applied AC potential and both voltage and current are in-phase throughout a resistor, a different measure is used instead, the electrical impedance (Z). Electrical impedance can be thought of as the unified measure of the tendency of a circuit to oppose the flow of current and it is applied strictly to AC circuits. Impedance takes on the form of a complex number (complex impedance) as it incorporates both the resistance which is the real part of the impedance, independent of the applied frequency and the inductive

or capacitive reactance (jX_L , jX_C) which are the imaginary components of the complex impedance, of a circuit element (inductor or capacitor) [4]. Complex impedance is used in the studies of multi-component AC circuits. The complex impedance contributions of different circuit elements are presented as phasors along a complex plane as seen in fig. 1.4, with resistance along the real axis and the inductive or capacitive reactances along the imaginary axis [19], [4]. The phasor representation for the complex impedance helps in highlighting the phase difference caused by a reactive circuit element. As impedance takes the theory of electrical resistance and applies it to AC circuits defined as linear or pseudo-linear systems where sinusoidal potentials and currents are used, it is apparent that Z possesses both magnitude and phase and it is dependent on the angular frequency (ω) of the applied AC potential. For AC circuits the I/V mathematical representation, as seen in eq. (1.2) and eq. (1.3), incorporates the alternating frequency as both the current and voltage are sinusoidal waves that are time dependant. Even more, in the case of I_t , the current signal response, is characterized by both its signal peak I_o and the phase shift Φ proportional to the applied AC potential. Both potential and current response can be expressed as cartesian or polar forms as seen ineq. (1.2) and eq. (1.3) [19], [20].

$$V_t = V_o \sin \omega t \text{ and } V_t = V_o e^{j\omega t} \quad (1.2)$$

$$I_t = I_o \sin(\omega t - \Phi) \text{ and } I_t = I_o e^{j(\omega t - \Phi)} \quad (1.3)$$

Of which V_t and I_t are the instant potential and instant current at a specific time t , V_o and I_o are the potential and current amplitudes (peak maximum), ω is the radial frequency expressed in radians/second (rad/s), t is the time (s), $j = \sqrt{-1}$, and Φ is the phase shift (rad). The relationship between ω and frequency is expressed as $\omega = 2\pi f$ where f is the frequency expressed in hertz (Hz) [7].

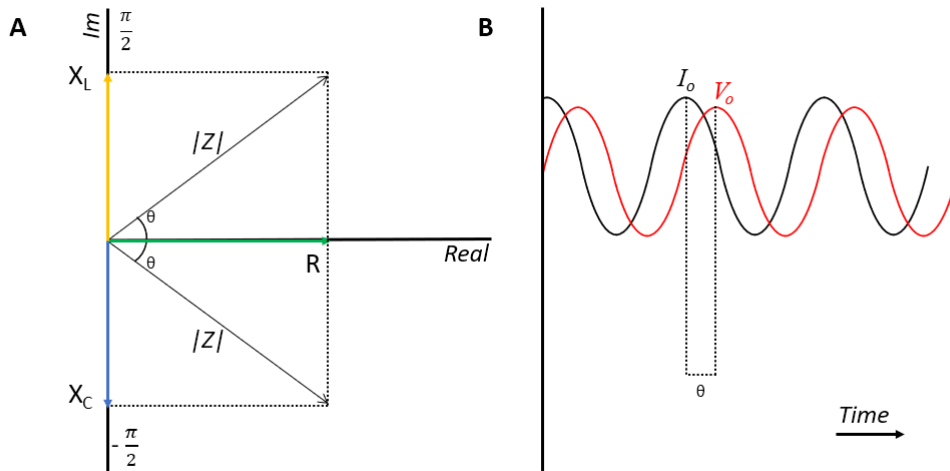


Figure 1.4: Graphical representation of the impedance complex plane and phase shift. A: phasor diagram of the impedance complex plane showcasing both the imaginary components X_L and X_C and the real component R . $|Z|$ is determined by applying Pythagoras's theorem in each respective quadrant. B: phase shift specific for an RC circuit where voltage lags the current with a phase shift of ϑ .

Adapted from [4] with permission from Springer Nature.

The ratio of the amplitudes of the applied AC potential and the current response together with the phase shift between the signal waveforms are used to determine the impedance of an electrical circuit. It can be seen in eq. (1.4) that impedance is represented as a complex number with both imaginary and real components where R and X are the resistance and reactance of a circuit element, expressed in cartesian form [4], [20], [19].

$$Z = R + jX \quad (1.4)$$

In the case of ideal resistors, the impedance is purely real as depicted in fig. 1.4, it is independent of the applied frequencies and it is called resistive impedance. On the other hand, ideal capacitors and inductors exhibit a purely imaginary impedance called reactive impedance where the main difference is the phase shift angle. Starting from eq. (1.1), eq. (1.2) and eq. (1.3) the impedance expression for a resistor can be obtained. As it can be seen in eq. (1.5) the impedance of an ideal resistor is proportional to its resistive value and both current and voltage are in phase ($\Phi=0$) [19], [20].

$$\begin{aligned} V = IR &\implies V = RI_o e^{j(\omega t - \Phi)} \implies \frac{V}{I} = \frac{RI_o e^{j(\omega t - \Phi)}}{I_o e^{j(\omega t - \Phi)}} \\ \frac{V}{I} = R &\implies Z_R = R \end{aligned} \quad (1.5)$$

Following the same approach, the impedance expressions for ideal resistors and capacitors can be determined and are dependant on the applied frequency. As shown in eq. (1.6) an inductor's impedance value increases in conjunction with frequency while the current through an inductor is phased shifted by 90° with respect to voltage. On the other hand, the current through a capacitor is phase-shifted by -90° as depicted in fig. 1.4 and the impedance is inversely proportional to the applied frequency as shown in eq. (1.7) [19], [20].

$$\begin{aligned} V = L \frac{dI}{dt} &\implies V = L \frac{d(I_o e^{j(\omega t - \Phi)})}{dt} \implies \frac{V}{I} = L \frac{j\omega I_o e^{j(\omega t - \Phi)}}{I_o e^{j(\omega t - \Phi)}} \\ \frac{V}{I} = j\omega L &\implies Z_L = j\omega L \end{aligned} \quad (1.6)$$

$$\begin{aligned} I = C \frac{dV}{dt} &\implies I = C \frac{d(V_o e^{j\omega t})}{dt} \implies \frac{V}{I} = C \frac{V_o e^{j\omega t}}{j\omega V_o e^{j\omega t}} \\ \frac{V}{I} = \frac{1}{j\omega C} &\implies Z_C = \frac{1}{j\omega C} \end{aligned} \quad (1.7)$$

The magnitude of the impedance also known as the absolute value of the impedance ($|Z|$) of a given circuit can be determined from fig. 1.4 by applying the Pythagorean theorem in each quadrant depending on the circuit elements. The impedance effect of two devices for RL and RC circuits for series combinations of components is determined as the square root of the sum of squares of the resistance and reactance of the circuit elements. The specific $|Z|$ expressions for RL and RC circuits are given in eq. (1.8) and eq. (1.9) respectively where X_L and X_C are the inductive and capacitive reactance of the circuit components. The phase angle (Φ) difference is given by eq. (1.10) and the sign of the phase angle shows whether the voltage leads or lags the

current. A negative phase angle is matched to a capacitive behaviour while a positive phase angle is representative of an inductive behaviour [4], [20].

$$|Z_{RL}| = \sqrt{R^2 + X_L^2} \quad (1.8)$$

$$|Z_{RC}| = \sqrt{R^2 + X_C^2} \quad (1.9)$$

$$\Phi = \arctan \frac{X}{R} \quad (1.10)$$

In RLC circuits the capacitive reactance contribution is subtracted from the inductive reactance of the system and the $|Z|$ expression for an RLC circuit is shown in eq. (1.11). As the reactance term is always positive, the lowest impedance is reached when the overall reactance of the system is equal to 0, in other words, the lowest impedance of an RLC circuit is reached when both inductive and capacitive effects are equal. At this point, the current is at its maximum and the impedance at its minimum. This behaviour is observed at the resonant frequency f_o as presented in eq. (1.12) [20], [4].

$$|Z_{RLC}| = \sqrt{R^2 + \left(\omega L - \frac{1}{\omega C}\right)^2} \quad (1.11)$$

$$f_o = \frac{1}{2\pi\sqrt{LC}} \quad (1.12)$$

In order to capture and express the change in phase angle together with the impedance magnitude at a particular frequency, the polar form of impedance is used. By using complex exponentials, dividing and multiplying impedance values to characterize the total impedance of a complex circuit is less challenging when compared to the cartesian coordinate approach. Combining series impedances is straightforward and both cartesian or exponential (polar) forms can be used since the only real operations are subtraction and addition. The real challenge comes from combining parallel impedance values where rationalization is required. Starting from eq. (1.4) the polar form of the complex impedance for a two terminal circuit can be deduced. By rewriting eq. (1.4) under the form of trigonometric functions of the phase angle, eq. (1.13) is obtained where $\sin \Phi Z = X$ and it represents the total reactance of the system and $\cos \Phi Z = R$ represents the resistive effect.

$$Z = \cos \Phi Z + j \sin \Phi Z \quad (1.13)$$

Furthermore, by applying the Euler relationship for trigonometric functions, $e^{jx} = \cos x + j \sin x$, to the above-mentioned expression, the polar form of complex impedance is obtained as shown in eq. (1.14), where the modulus $|Z|$ is equivalent to the ratio of current maximum to voltage maximum and the exponent $\exp(j\Phi Z)$ denotes the change in phase angle in the same expression [19].

$$Z = Z(\cos \Phi + j \sin \Phi) \implies Z = |Z|e^{j\Phi} \quad (1.14)$$

1.3.2 Series and parallel impedance combinations

The impedance contributions of different circuit elements can be determined as the total impedance of an electric circuit. The circuit elements arrangement dictates how impedance is calculated, however it follows the same rules as combining series or parallel resistances. In the case of a series arrangement, as depicted in fig. 1.5 the total impedance results in a complex function calculated as the sum of impedances of all the series circuit elements. An example for the total impedance of a two-element electrical circuit, in series, is shown in eq. (1.15) [21].

$$Z_{eq} = Z_1 + Z_2 \implies Z_{eq} = (R_1 + R_2) + j(X_1 + X_2) \quad (1.15)$$

Where the terms $(R_1 + R_2) = R_{eq}$ and $j(X_1 + X_2) = jX_{eq}$ describe the real and imaginary elements and their impedance contribution. Addition can be easily performed using either the complex impedance exponential or trigonometric functions. On the other hand, calculating the total impedance of two or more parallel circuit elements requires the conversion to real, rather than complex numbers, through rationalization. The mathematical approach to calculate parallel impedances is the same as calculating parallel resistances and it is shown in eq. (1.16) for two parallel circuit elements while using the cartesian notation. The rationalization of imaginary numbers results in lengthy algebraic equations which use relationships specific for complex variables to determine and separate real and imaginary components. A shortlist showcasing the most important operations for complex variables is presented in Appendix A. In the case of series and parallel combination of circuit elements, the total impedance is calculated in blocks as the sum of series components and the sum of parallel components [19], [20].

$$\frac{1}{Z_{eq}} = \frac{1}{Z_1} + \frac{1}{Z_2} \implies Z_{eq} = \frac{Z_1 Z_2}{Z_1 + Z_2} = \frac{(R_1 + jX_1)(R_2 + jX_2)}{(R_1 + R_2) + j(X_1 + X_2)} \quad (1.16)$$

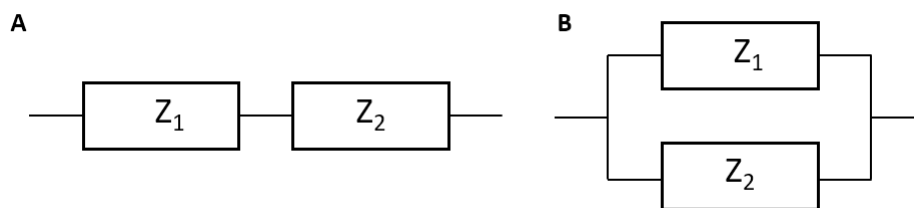


Figure 1.5: A: series arrangement of electrical circuit elements and their impedances B: arrangement of electrical circuit elements in parallel and their impedances.

1.3.3 EIS applied on biological systems

EIS is considered a powerful analytical tool used for the characterization of interfacial processes occurring at the electrode-electrolyte interface. Once changes occur at the surface of the electrode, such as the formation of the immune complex, a measurable change in impedance can be identified. Different behaviours, such as capacitive, inductive, or diffusion related, can be pinned down during EIS spectra analysis and can

be used to define the system. The data obtained during EIS is useful once validated [15].

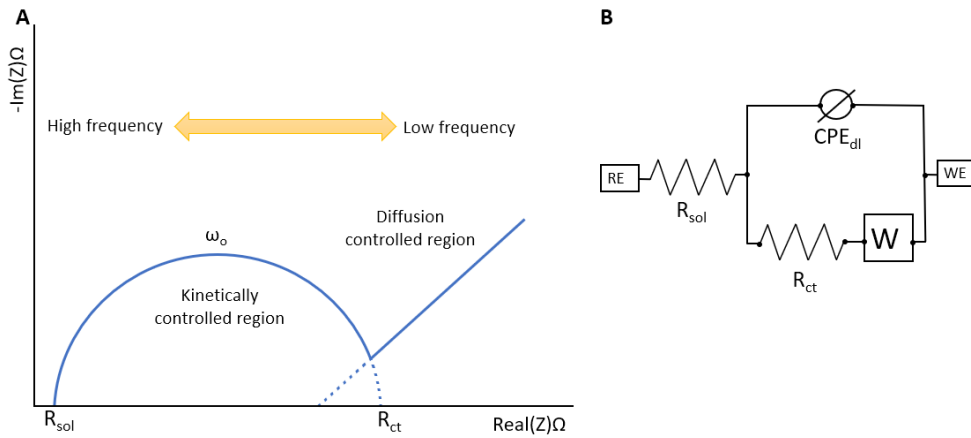


Figure 1.6: A: Nyquist complex plane diagram specific for the modified Randles equivalent circuit. The kinetically controlled region showcases the electrochemical reaction occurring at the surface of the electrode (the redox reaction rate, electron transfer rate, charging of the electric double layer) while the second region reveals the diffusion limited processes where ion migration to the electrode is the major impedance contribution. B: Randles equivalent circuit with mixed kinetics and charge transfer control. Adapted from [15] with permission from The Royal Society of Chemistry.

Data validation is done through modelling by fitting the spectra of a complex system to a suitable electrical circuit, also known as an equivalent circuit. The role of such a circuit is to integrate the spectra of a biological system and to describe it in terms of electrical circuit components. In the case of biological systems, such as biosensors based on biomolecules, the Randles equivalent circuit is most commonly used. The equivalent circuit components reflect the impedance contribution of the elements involved in the electrochemical reaction. The data extracted from an EIS experiment is commonly visualized in two distinct plots. The relationship between imaginary and real impedance contribution of the system is plotted against one and another in a Nyquist plot, also known as a complex plane impedance diagram. A typical Nyquist plot for a Randles circuit is shown in fig. 1.6. Equation (1.17) relates the imaginary term Z'' with the real term Z' that shape up the Nyquist plot and it is specific for the Randles equivalent circuit as it incorporates the solution resistance in series with the parallel arrangement composed of the charge transfer resistance and the double layer capacitance which represent the circuit time constant ($\tau = R_{sol}C_{dl}$) [3], [4], [15].

$$Z(\omega) = R_{sol} + \frac{Z_{R_{ct}} Z_{C_{dl}}}{Z_{R_{ct}} + Z_{C_{dl}}} = R_{sol} + \frac{R_{ct} \frac{1}{j\omega C_{dl}}}{R_{ct} + \frac{1}{j\omega C_{dl}}} = R_{sol} + \frac{R_{ct}}{1 + j\omega R_{ct} C_{dl}} \quad (1.17)$$

From eq. (1.17) the real and imaginary parts of the impedance can be extracted through rationalization. In order to express eq. (1.17) in terms of Z'' and Z' , the denominator must be converted from an imaginary to a real term by multiplying the fraction by the complex conjugate $1 - j\omega R_{ct} C_{dl}$. Following rationalization, the real

and imaginary elements Z' and Z'' can be separated as demonstrated in eq. (1.18) [7].

$$Z(\omega) = R_{sol} + \left[\frac{R_{ct}}{1 + j\omega R_{ct} C_{dl}} \right] \left[\frac{1 - j\omega R_{ct} C_{dl}}{1 - j\omega R_{ct} C_{dl}} \right] = R_{sol} + \frac{R_{ct} - j\omega R_{ct}^2 C_{dl}^2}{1 + \omega^2 R_{ct}^2 C_{dl}^2} \quad (1.18)$$

$$Z(\omega) = Z' + Z'' = R_{sol} + \frac{R_{ct}}{1 + \omega^2 R_{ct}^2 C_{dl}^2} - j \frac{\omega R_{ct}^2 C_{dl}^2}{1 + \omega^2 R_{ct}^2 C_{dl}^2}$$

The Bode plot shows the frequency dependence of the impedance. In a Bode plot, the impedance magnitude ($|Z|$) and the phase shift (Φ) are plotted as the frequency response of the electrochemical reaction. The Randles equivalent circuit consists of an electrolyte solution resistance or R_{sol} representing the bulk resistance of the electrolyte solution. This component is easily identified on a Nyquist plot as the first intersection of the semicircle with the real axis, at high frequencies, making R_{sol} a strictly real component as also expressed in fig. 1.6 [7], [15].

While R_{sol} could have a considerable contribution to the overall impedance of the system, modern potentiostats use a three-electrode configuration and can compensate for this resistance between the counter and reference electrode. The electrolyte resistance is still present between the working and reference electrode and appears as a small contribution during EIS experiments. This small resistive contribution comes from the uncompensated solution resistance which is a value measured during EIS. R_{sol} is independent of the applied frequency but is dependant on the solution concentration, pH, the geometry of the area where current flows, the applied potential and temperature. For an electrolyte solution under AC potential and no DC bias applied, R_{sol} can be calculated as shown in eq. (1.19) by using a two-electrode system [21].

$$R_{sol} = \rho \frac{l}{A} \quad (1.19)$$

Where ρ is the solution resistivity, A is the area over which charge is carried and l is the distance between the two electrodes in the electrolyte solution.

On the other hand, the double-layer capacitance, C_{dl} , arises as to the insulating layer contribution in series with the charge separation at the interface. A graphical representation for the charge separation at the interface and double-layer formation following the Stern model is shown in fig. 1.7. This approach combines the Helmholtz and Gouy–Chapman models for a better picture of the interface between a solid and an electrolyte solution. The Helmholtz model does not account for the ion migration through the liquid phase but it successfully portrays the double-layer formation while the Gouy–Chapman model improves the general idea of the electric double layer by introducing the charge distribution of ions as the diffuse layer. The Stern model improves over the Helmholtz and Gouy–Chapman models by accounting for adsorption of molecules on the surface and by realistically limiting solvent access to the surface which are not in intimate contact but separated by a distance on the order of a few nm. Once an electrical potential is applied, such as during EIS, charge separation occurs at the electrode–electrolyte interface. An excess of positive charges forms a highly ordered, immovable, ionic layer, at the interface, also known as the Stern layer. At the interface, between the two ionic layers, a solvent monolayer forms which act as the dielectric in a conventional, plate capacitor. The solvent monolayer is known

as the inner Helmholtz plane and at this level, the charge is stored under the form of an electric field [7], [15].

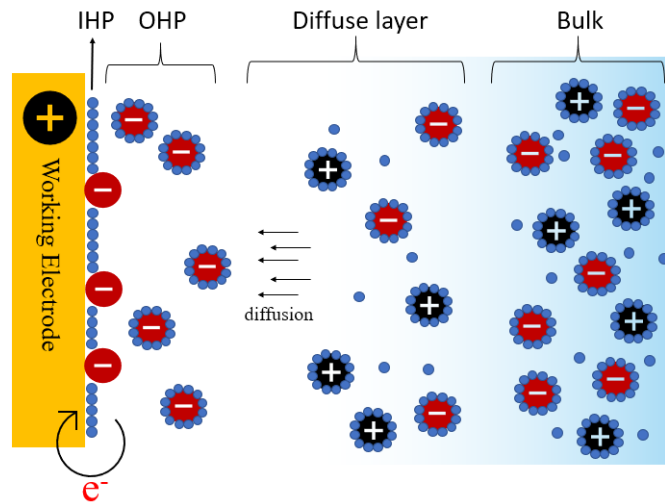


Figure 1.7: Schematic representation of the double layer formation at an unmodified working electrode during EIS measurements where IHP - the inner Helmholtz plane is represented by a solvent monolayer formed at the interface, OPH - the outer Helmholtz plane composed of solvated ions adherent to the interface and the diffuse double layer. The double-layer formation is modelled as a conventional plate capacitor in an equivalent circuit. Adapted from [7] with permission from Elsevier.

When EIS is performed, charge separation occurs at the interface, especially at high to mid frequencies, promoting the double-layer formation which can be charged or discharged, likewise a conventional capacitor. C_{dl} is dependent on the dielectric permittivity of the solvent molecules and of the bio-layer and the applied potential. An increase in applied electric potential attracts more counterions from the bulk electrolyte and increases the effective capacitance. Further increasing the layer thickness decreases the overall C_{dl} of the system as expressed in eq. (1.20).

$$C_{dl} = \frac{\epsilon_{dl}A}{\delta} \quad (1.20)$$

Where: $\epsilon_{dl} = \epsilon_o\epsilon_p$, ϵ_o is the effective permittivity of vacuum, ϵ_p is the effective permittivity of the insulating layer, A is the electrode area and δ is the thickness of the dielectric. In capacitance-based biosensors which are reserved to measure the impedance of the cell without charge transfer occurring at the WE, δ has a great effect over Z . Each modification step involving the WE will increase δ , decreasing the capacitance and subsequently increasing the resistive effect of the double layer. The recognition layer also changes the dielectric permittivity of the insulating layer further decreasing capacitance [7].

In the case of a faradaic biosensor, the overall impedance contribution of the double layer is limited by the parallel path through R_{ct} , which dominates in charge transfer related processes (redox reaction) [3]. Since C_{dl} is modelled as a capacitor under perfect circumstances which are unachievable under experimental conditions, a constant phase element (CPE) is used instead, when simulating EIS spectra for biological

systems. A CPE simulates the double layer behaviour while accounting for surface roughness and electrode imperfections. Electrode defects are a source of inhomogeneity and are introduced during electrode fabrication or during functionalization such as the imperfect SAM coverage. The impedance mathematical representation for CPE_{dl} , which is a placeholder of the double-layer capacitance in a equivalent circuit, is derived from eq. (1.7), and can be seen in eq. (1.21) [3], [7], [21].

$$Z_{CPE_{dl}} = \frac{1}{Y_o(j\omega)^\alpha} \quad (1.21)$$

The constant Y_o ($S \cdot s^\alpha$), in most cases, is analogous to the capacitance (C) and the dimensionless exponent α represent the constant phase where $-1 \leq \alpha \leq 1$ [21]. For a CPE substituting a capacitor the constant phase value ranges from 0.85 - 1. When $\alpha = 1$ the CPE will act as a pure capacitor and eq. (1.7) and eq. (1.21) become interchangeable. For $\alpha = 0$ a CPE will act as a pure resistor, while a negative value implies an inductive behaviour. The name of the circuit element is derived from the fact that the phase angle of the impedance vector for a CPE is a constant independent of the applied frequency. By applying an AC potential across a capacitor the measured phase shift between the current and potential waveforms is equal to -90° while the phase difference through a CPE substituting a capacitor is given by the relation $(-90^\circ \times n)$. When simulating EIS spectra of a bio-modified electrode the phase shift at mid-high frequencies is expected to be less than -90° due to surface roughness. The impedance mathematical expression for a simple faradaic reaction without mass transfer following the Randles equivalent circuit can be expressed in terms of a CPE substituting a capacitor, as seen in eq. (1.22) [4], [7].

$$Z(\omega) = R_{sol} + \frac{R_{ct}}{1 + (j\omega)^\alpha R_{ct} Y_o} \quad (1.22)$$

For a non-ideal electrode such as those used in biosensing in which the surface topology and characteristics vary due to the functionalization steps, the semicircle region on the Nyquist plot specific for the $R_{ct} - C_{dl}$ parallel arrangement has the aspect of a depressed semicircle with the centre region below the Z' axis. This indicates a shift in surface properties over the specific electrode area. Time constant dispersion over the electrode surface is the main influence leading to the CPE behaviour, where the time constant τ is the RC product of the parallel RC arrangement. Time constant dispersion is generated by reaction rates, current and potential variations along the electrode surface. The CPE behaviour is explained by the distribution of time constants which are specific for charge transfer processes occurring at different points on the electrode surface. As a result, a distribution of τ is present at the whole circuit scale. These surface variations can lead to either a 2-D, along the surface, distribution or a 3-D, in the normal direction to the surface, distribution, each with a different cause. In the case of 2-D distribution, different time constants are introduced due to grain boundaries between two crystallographic planes or by adsorption and formation of impurities layers with different properties from the bulk. As for a 3-D distribution, adsorbed species, surface roughness and changes in porosity along the x,y and z-axis introduce localized and different electric properties along the interface. In the case of impedance biosensors, attachment of biorecognition elements represents a 3-D distribution of different time constants which are also influenced by the 2-D distribution of surface defects. The double-layer capacitance can be calculated from the characteristic frequency ω_o as it can be seen in eq. (1.23), where the imaginary term Z'' is

at its maximum. The capacitance value can be used as a starting parameter during modelling when using a CPE element [20].

$$\omega_o = (R_{ct}C_{dl})^{-1} \quad (1.23)$$

R_{ct} or the charge transfer resistance is introduced as a parallel pathway to C_{dl} in faradaic biosensors. The semicircle region in fig. 1.6 is specific for a charge transfer limited process in which electrons flow from the solution through the working electrode given the fact that the solution contains redox-active species and the system is biased at the characteristic redox potential of those species [3]. For a plain, unmodified electrode, R_{ct} value is dependant on the conductive nature of the working electrode which in part is given by the electrode material. R_{ct} is also influenced by the solution conductance, by the redox reaction kinetics such as the rate of reaction and the electrolyte solution concentration. Upon a closer look at fig. 1.6, it can be noticed that the R_{ct} value can be extrapolated from the second intersection of the semicircle with the real axis as $R_{sol} + R_{ct}$ making it a real quantity [15]. The rather real identity of the charge transfer resistance is also shown in eq. (1.18). In faradaic biosensors, R_{ct} and occasionally C_{dl} are chosen as the response of the antibody-antigen interaction since they have the highest contribution in the overall impedance of the system. R_{ct} is a surface quantity and can be thought of as the opposition in charge transfer across the interface. Resistance emerges from a kinetically controlled electrochemical reaction at equilibrium under specific potential. For one-electron transfer processes, the electrons enter the metal electrode and metal ions diffuse into the electrolyte according to eq. (1.24) [7], [21], [22].



The presence of R_{ct} is strictly correlated by the presence of redox-active molecules undergoing reduction or oxidation and it is a faradaic component. R_{ct} represents the activation barrier for the electron transfer process when the standard or formal electrode potential is used as biasing potential. It is determined from the Butler–Volmer equation for an electrochemical reaction under equilibrium as shown in eq. (1.25), [22].

$$R_{ct} = \frac{RT}{nFi_0} \quad (1.25)$$

Where R is the gas constant, T is the temperature, F is Faraday constant and i_0 is the exchange current density. The electron transfer rate (k_0) can be calculated from the following relationship $i_0 = k_0FC$. A system reaches equilibrium when the bulk electrolyte concentration is equal to the surface concentration and the reduction and oxidation rates are uniform while the overpotential is negligible (the electrode reduction potential (E) is close or equal to the formal potential (E_o)). Lastly, the Warburg elements is introduced and used in equivalent circuit modelling as the contribution of the diffusion process [15]. The diffusion-controlled region can be identified on a Nyquist plot as a line with a 45°slope. On the other hand, in the Bode plot, the diffusion process has a phase shift of 45°. Its impedance contribution is small when

compared to other elements and it is present at very low frequencies. It is influenced by the applied potential, solution concentration and the redox reaction kinetics [21].

1.4 Impedance biosensors: design and applications

A biosensor is a complex system which in order to function properly, has to be designed from the ground up requiring expertise in nanotechnology and nanofabrication, chemistry and biology. For building an electrochemical immunosensor the following have to be taken into account: the electrode system and the electrochemical cell setup, the study of specific antibody-antigen interaction, the surface treatment and surface functionalization and the characterization methods. Moreover, once the biosensor has passed all the necessary requirements showing high affinity and specificity, low LOD and no cross-reactivity it can be commercially produced.

1.4.1 Lab-on-a-chip approach

The golden standard for electrochemical measurements is the electrochemical cell hosting the redox reaction and its components, the three-electrode system and the current or voltage regulator units, the potentiostat/galvanostat. In biosensing, this setup can be easily applied to study the biosensor response yet, the lab-on-a-chip formats are more suitable in terms of size, cost, and reproducibility. For capacitive biosensors, the most common lab-on-a-chip approach is the use of interdigitated electrodes (IDE) while for faradaic impedance biosensors, microelectrodes and screen printed electrodes (SPE) are commonly used. In the case of IDE chips, they come in the shape of gold, silver or platinum arrays patterned on Si or glass substrates with an approximate electrode length and electrode spacing between 5-10 nm to tenths of microns. The key feature of capacitive biosensors, which are a subclass of impedance biosensors, is that the analyte concentration is measured indirectly by measuring the capacitive effect of the bilayer on the IDEs, in other words, the change in capacitance of an IDE is caused by a change in dielectric permittivity between the electrodes, the formation of the AG-AB complex [3], [15], [23].

Screen printing of disposable microelectrodes is a versatile method in which pastes are deposited, layer-by-layer on a ceramic or plastic substrate with the help of a mobile mesh. The resulting SPEs can replace an electrochemical cell and are suitable for low volume operations. Another advantage of SPEs is that they are easily modifiable to meet specific requirements such as increased WE surface area or the use of different ink curing temperatures resulting in different surface characteristics. Many metal- and nonmetal-based inks can be used in SPEs fabrication, of which carbon, silver, gold and platinum inks are most commonly used. SPEs used in impedimetric immunosensors are commonly equipped with gold WEs and take advantage of gold-thiol chemistry by forming self-assembled monolayers (SAMs) when thiol compounds are used. SAMs form on the gold surface which upon activation will covalently bind the biomolecules to the electrode, preserving their bio-activity which results in a stable biosensing platform. The use of SPEs in impedance biosensors further simplifies the system by keeping the solution impedance contribution constant, by having the electrodes in a fixed position during EIS measurements. The ability of almost identical SPEs to be mass-manufactured in bulk also improves data comparison between the chips, while maintaining a low output signal drift between two sensors [24], [15], [25].

SPEs are currently available in a wide range of configurations and are directed not only for research purposes, as a biosensor platform, but can be obtained as already modified and ready to use biosensor for analytical purposes, mainly in environmental and food chain monitoring. Oxygen, sodium, alcohol and salinity sensors that make use of the SPE platform are developed and sold by Zimmer&Peacock either as disposable or multiple-use sensors. According to Zimmer&Peacock a drop in sensitivity of 5-10% is expected in subsequent analysis, which proves that further research and tuning of this platform could attain better results. As for biomedical applications of SPEs, commercially available modified SPEs for glucose monitoring already exist and are part of a multi-billion dollar market of disposable biosensors. Commercial integration of such sensors is attractive due to low cost and POC usage [26]. With the number of people suffering from chronic diseases, such as type 1 and 2 diabetes, the market share of disposable SPEs is rising. According to The World Health Organization (WHO), the global prevalence of diabetes in adults rose from 4.2% in 1980 to 8.5% in 2014, further consolidating the need for fast and accurate biosensors and biomonitoring units [27].

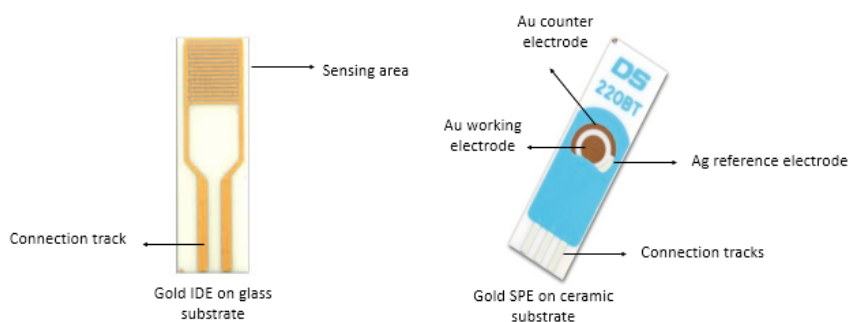


Figure 1.8: Models of lab-on-a-chip formats for electrochemical biosensing. For capacitive biosensors IDE are used with conjugated biomolecules in-between each digit. In faradaic driven impedance biosensors, SPEs are used where the working electrode is bioconjugated with the biorecognition elements.

Implantation and integration of impedimetric biosensors prove to be challenging from a biocompatibility standpoint. Current research trend towards wearable and implantable smart sensors with biomonitoring applications has proven that, indeed, continuous monitoring is possible and effective, yet it has to be complemented by classical analytical methods. In the case of indirect and continuous amperometric detection of glucose, implantable chips are readily available since 2005 and are produced by either Medtronic or Dexcom. These chips function by indirectly measuring the blood glucose concentration by detecting the level of hydrogen peroxide produced after the oxidation of glucose by glucose oxidase. One downside of such devices is the limited biocompatibility and the short life span on the order of days, after which the biosensor has to be replaced [11]. No equivalent impedance-based biosensor is commercially available at the moment however, wearable impedimetric sensing platforms are currently being studied. Wearable bioimpedimetric devices to estimate fat-free body mass or shifts in body fluids are currently being research [28]. Jung et al. [29] proposed a new contact resistance compensated impedance-based measurement technique to assess the percentage of body fat. The system is integrated on a wristband and enables instant skin impedance measurements which can be translated to body fat percentage by the integrated bio processor. The advantage of such a device is that

skin impedance measurement usually require a high contact surface area between the skin and the electrode however this was compensated through the placement of the electrodes (two voltage sensing and two current driving electrodes) and the novel contact resistance compensation function.

1.5 Self assembled monolayers

Self-assembled monolayers (SAMs) have been widely used as anchors and immobilization sites for many different recognition elements, in biosensing. Extensive research regarding the formation kinetics of SAMs on metal surfaces made it possible to exploit their unique properties in analytical applications. One key aspect of SAMs with applications in electrochemical biosensing is the ability to form a closely packed 2D stable molecular layer on the WE surface where the oriented attachment of recognition elements can take place. In the case of antibody attachment, the orientation of the macromolecule dictates the efficiency of the sensor. Greater efficiency is obtained by increasing the available surface area of the recognition element which can bind the analyte. This can be done through the covalent attachment of the macromolecule onto the SAM. The greater orientation of the recognition element increases the specific interface reactions while decreasing the non-specific interactions and the interference in the system [30], [31], [32]. Many coupling strategies have been employed for a favourable orientation of the antibodies attached to SAMs. Tsugimura et al [32] reported the lowest LOD (0.001 ng/ml) for a myoglobin impedimetric biosensor by covalently attaching the anti-myoglobin IgG to an alkanethiol SAM through an intermediary macromolecule, the protein G. The Fc region of the antibody is known to specifically bind the protein G which is grafted onto the SAM. This approach shows an increase in specificity when compared to the direct coupling of the antibody to the bifunctional SAM. By using the interaction between PrG and IgG, the antibodies orient both binding sites at the surface, further increasing the capture probability for the antigen thus lowering the detection limit. Another possibility for oriented attachment of antibodies on sensing surfaces has been proposed by Karyakin et al. [33]. The group focused on the direct attachment of antibody fragments onto gold electrodes via their native thiol groups which improved over the traditional approach of using linker molecules, by increasing the surface coverage and subsequently the binding capacity of the antibodies. On the other hand, the chemical process used for obtaining IgG fragments is more complex than the conventional approach of using full-length antibodies where no further purification steps are required. Another possible drawback of direct coupling of IgG fragments is the loss of biorecognition capabilities of the antibody as stated by the authors but this effect was not observed at the end of the study.

While bifunctional organic molecules such as 3-mercaptopropionic acid, cysteamine, 1-dodecanethiol, 11-mercaptopundecanoic and 12-mercaptododecanoic acid have been successfully employed in SAMs formation for biosensing applications, the insulating properties of the alkyl chains can have a great impact on the system response, especially in electrochemical sensing. The insulating properties of the SAMs are correlated to the alkyl chain length [23]. Chen et al. [34] proposed and developed a conductive thiophene-based organic linker that could self-assemble on gold-coated surfaces in 6 hours. The SAMs were characterized in terms of CV and EIS. According to the paper, the novel linker enhances charge transfer across the interface due to its molecular structure containing two thiophenes and due to the small dihedral angle between these moieties. This specialized SAM enables electrochemical sensing in the case of small

molecules when the binding event between an antibody attached to a conventional insulating SAM and the antigen would cause a very small change in impedance, on the order of the background noise signal, rendering such a biosensor superior for small biomarkers detection.

1.5.1 Self assembly mechanism

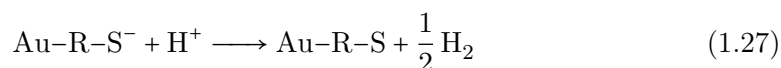
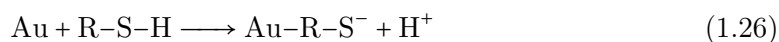
Self-assembly can be thought of as the ability of a disordered system, composed of either small particles or fragments, to spontaneously assemble into ordered units [35]. In general, self-assembly is driven by weak interactions between the involved chemical species but can be extended to strong covalent interactions as in the formation of polymer derived nanostructures by controlling the kinetics of the self-assemble mechanism or by template-assisted self-assembly [36]. Ordering of a multi-element system occurs via physical interactions between the particles or by external triggers. An important aspect of self-assembly as a tool in chemistry and surface modification is the potential to build entire systems without having to design each building blocks at a time. The formation of self-assembled structures can be observed in nature under the shape of protein folding, DNA transcribing and hybridization, target-ligand interactions and lipid membranes formations. Taking examples from nature, self-assembled systems can be build and employed in several fields such as nanoelectronics, drug delivery systems, material science and biosensors [35], [37].

It is well established by now that alkanethiols and thiol derivatives can form organised layers of molecules on the surface of metals, predominately on gold films with different crystallographic orientations (Au111, Au200, Au220). Other noble metals, such as platinum, palladium or silver have been successfully used as solid substrates for SAMs formation due to their outstanding chemical stability. The SAMs formations can occur spontaneously in dilute solutions or in gas phase by sublimation [30], [31], [38]. In the case of organothiols, due to the high affinity of the sulphur atoms to the gold surface, strong and stable covalent bonds are formed in a matter of minutes. In normal conditions gold is practically non-reactive and very stable, adsorbing very little atmospheric contaminants. It is not readily dissolved nor oxidized by common organic and inorganic solvents and it does not form a stable surface oxide layer. The aforementioned properties make gold the most used substrate for self-assembly. The formation of closely packed SAMs on metal films involves the diffusion of bifunctional molecules from solution to the interface where chemisorption takes place. The self-assembly process is not limited to the strong interactions between the head groups of the dissolved molecules and the metal surface and takes into account the electrostatic, Wan der Waals and entropic interactions between the monolayer, solvent and metal [31].

Thermodynamically driven self-assembly of amphiphiles on solid supports is a perfect example of SAM formation. The interactions of the hydrophilic and hydrophobic regions of the amphiphile with the solvent drive the self-assembly process. A thin film of surfactant deposited on water, also known as a Langmuir film, would self-assemble on a solid support once in contact to minimize the interaction between the solvent and the hydrophobic tail followed by a decrease in surface energy. This type of self-assembly was the subject of thorough research in the past decade and serves as the basic principle of thermodynamically driven self-assembly [35]. This kind of self-assembly behaviour arises from the need of the system to reduce its surface free energy thus an ordered system at equilibrium would counteract the decrease in entropy by a reduction in total free energy or the case of a Langmuir–Blodgett film (LB), a

reduction in surface tension. The change in surface free energy and the formation of a monolayer was showed to be dependant on the molecular backbone of the molecules used as building blocks. Successful deposition techniques for LB multilayers formation using long-chain fatty acids were carried out by Corkery [39] resulting in altering LB films of different orientation (X, Y and Z). In the case of surfactants, the number of hydrocarbons in the alkyl chain dictates the route of self-assembly. A surfactant molecule with more than 12 hydrocarbons can successfully form an insoluble monolayer. In the case of shorter molecules, micelles are formed where molecules rearrange their hydrophilic residues outside the micelle core, increasing their solubility. Spontaneous self-assembly of surfactants as a function of concentration is known to occur once the critical micelle concentration (CMC) threshold is reached. Once the concentrations exceed the CMC value, aggregates are formed under the shape of micelles. A long alkyl chain results in an insoluble crystals formation at the water-vapour interface as the monolayer collapses and the 3D structure is formed [40].

The SAM formation mechanism and kinetics of alkanethiols on gold, silver and mercury coated electrodes were studied by Cohen-Atiya and Mandler [41] by using in-situ charge transfer measurements on n-alkanethiol SAMs modified electrodes. The model proposed in this paper tries to elucidate the SH–Au bond formation between adsorbed alkanethiols and gold. The paper covers two possible routes which may lead to a chemisorbed alkanethiol on the gold surface. This model was suggested on the basis that most alkanethiols adsorbed on gold surfaces are thiolates (R-S^-) due to the deprotonation of the thiol group (R-S-H) [42]. This signals the loss of the hydrogen bond as observed by FTIR and Raman spectroscopy. The two routes of SAMs formation on gold as proposed in this report are the oxidative adsorption of the organosulfur compound, eq. (1.26) and the subsequent discharge/reductive elimination of hydrogen, eq. (1.27) [43].



By measuring the open cell potential (OCP) before, during and after the addition of n-alkanethiols in the electrolyte solution two distinct behaviours were observed. A short-lived negative shift of the OCP upon addition of n-alkanethiols was noticed which signals charge being transferred at the interface. This step represents the oxidative adsorption of the thiols.

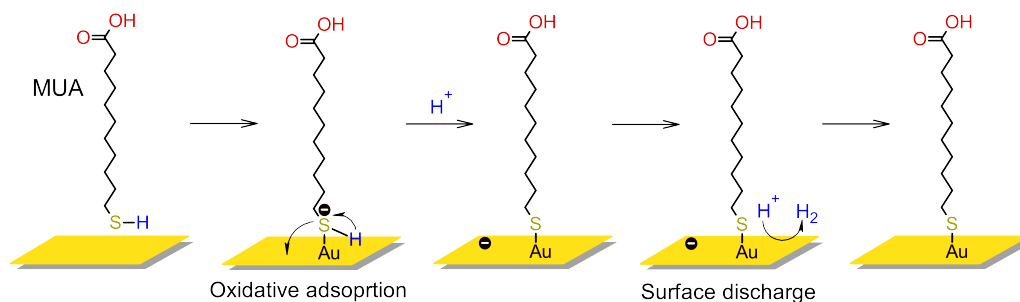


Figure 1.9: Surface reaction of chemisorbed 11-mercaptoundecanoic acid on a gold surface. Adapted from [31] with permission from Springer Nature.

The surface discharge takes place shortly after the oxidative adsorption and shifts the OCP value close to the starting value and signals the reduction of the thiolate proton to molecular hydrogen. In the case of the oxidative adsorption process, the hydrogen bond within the thiol functional group is weakened by a shift in electron density in the sulphur atom, closer to the interface. The increase in surface negative charge lowers the overpotential of the proton reduction step driving the reaction towards proton formation. The free proton is reduced to molecular hydrogen by the discharge of the gold surface. The discharge mechanism can be attributed to the molecular hydrogen formation as alkanethiols can self-assemble from gas-phase in an oxygen-depleted atmosphere [43]. Furthermore, the discharge process was shown to be dependant on the solvent proton concentration. A schematic representation of this surface reaction can be seen in fig. 1.9.

In terms of kinetics, the SAMs formation of thiols occurs in two successive steps as observed by AFM and STM imaging [43]. A schematic representation of alkanethiols SAMs formation kinetics is shown in fig. 1.10. The initial fast adsorption of molecules occurs within minutes of gold immersion in thiol solution. This step is governed by the diffusion process of the alkanethiols at the gold surface where the chemical affinity of the sulphur atom to the gold enables monolayer formation. This initial step is dependant on the thiol derivative solution concentration and on the head group-substrate interaction. The rate of thiol adsorption was revealed to be directly proportional to the solution concentration, highlighting a relationship between mass transport and bulk concentration. This behaviour can be explained on the basis of diffusion-controlled Langmuir adsorption [31], [44]. The second step is governed by the intermolecular interactions of the adsorbed species and results in an almost perpendicular arrangement of the adsorbed molecules where the tightly packed SAM is formed as a result of increased Wan der Waals forces between adsorbates [31], [42].

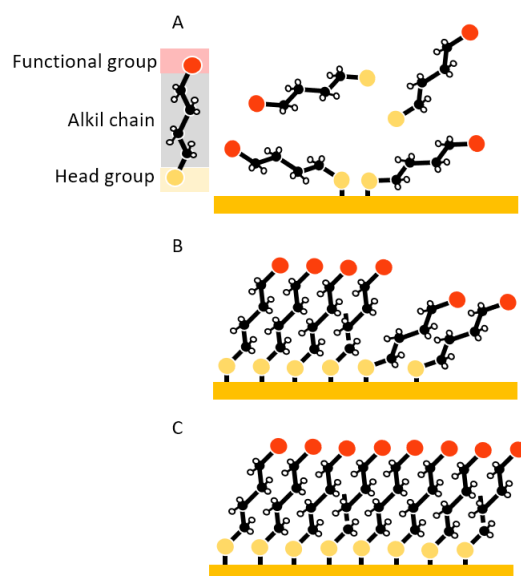


Figure 1.10: Different stages of monolayer formation: the fast initial adsorption step of alkanethiols from solution to the gold surface (A), rearrangement of adsorbed molecules by means of intermolecular interactions (B) and the final high-density and highly-ordered monolayer structure (C). Adapted from [45] with permission from the Royal Society of Chemistry.

The slow phase includes additional adsorption at defect sites, solvent expulsion by the monolayer and contaminants displacement [46]. The thickness and contact angles of the adsorbed films were observed to be 80-90% of the final values within minutes of immersion in alkanethiol solution as found out by Bain et al. [46]. Using contact angle (CAM) and optical ellipsometry measurements, the group investigated the slow and fast timescales of SAMs formation on thin gold films. The length of the molecules used to form SAMs was found to alter the wetting properties of the films. Monolayers formed by shorter chained molecules, ($n < 8$ where n is the number of carbons) had progressively lower contact angles suggesting a re-orientation of the adsorbed species, where methylene groups sit at the surface resulting in a higher degree of disorder within the monolayer. This behaviour was not observed in the case of long alkanethiols ($n > 10$). The reaction rate of chemisorbed alkanethiols was also determined to be dependant on the solvent. Dimethylformamide (DMF) and acetonitrile (ACN) were used as solvents in alkanethiol SAMs preparation by Schneider and Buttry and the resulting SAMs were characterized in terms of desorption and readsorption by CV scans and by quartz crystal microbalance (QCM). The solvent and the alkanethiol concentration were found to influence the stability of the SAM during potential cycling in both supporting electrolyte solutions and the final packing of the adsorbed layer. In the case of ACN solutions, a slow initial step with a final coverage of 50% was identified. Following this phase, a spontaneous multilayer film develops. As stated by the authors this is a possible side effect of the small initial coverage in chemisorbed species which leads to high surface energy promoting physisorption. The following step involves competing interactions between chemi- and physisorbed thiols at the end of which a stable closely packed monolayer is formed. In the case of DMF solutions, the CV scans show fast desorption and readsorption of the thiol derivatives when compared to the slow process in acetonitrile, yet a complete monolayer was never formed. These results hint at a possible influence of the alkanethiol solubility in different solvents and the self-assembly kinetics as better SAMs were obtained in ACN even if a better solubility was achieved in DMF.

1.6 Neutrophil gelatinase-associated lipocalin as a biomarker of renal function

NGAL or lipocalin-2 is a small 25-kDa protein that is continuously secreted by neutrophils under normal circumstances however recent studies promote the use of NGAL as a biomarker of kidney function. Different pathologies have been associated with high NGAL expression [47], [48]. First and foremost in the case of acute kidney injury (AKI), high levels of NGAL are secreted by damaged tubular epithelial cells. An increase in NGAL expression has also been linked to diabetes-induced nephropathy and urinary tract infections yet significantly lower level when compared to AKI [47], [48]. NGAL monitoring in healthy individuals should not exceed values in the range of 9-49 ng/ml however different ranges were reported based on sex and age with lower clinical significance in infants and young children. A positive AKI diagnosis can be proposed for adults with NGAL levels exceeding 100 ng/ml in urine [49], [50]. NGAL levels can be monitored either from urine or plasma however, urine detection was deemed more appropriate due to not being invasive and the fact that urine contains lower amounts of other proteins. Currently, NGAL evolution in patients is not monitored continuously because sandwich enzyme-linked immunosorbent assay (ELISA) is the most common detection method. In the case of AKI, a fast increase in NGAL concentration was observed in the first hours post-injury. While ELISA is highly accurate and sensitive

it takes too much time to obtain a positive AKI diagnostic [48]. An impedimetric immunosensor could prove suitable for fast NGAL levels assessment at POC. Furthermore, continuous detection is also possible using electrochemical techniques which in turn could provide a more accurate and fast medical response.

MATERIALS AND METHODS

2.1 Materials

All materials used in this report are reagent grade. All aqueous solutions and buffers were prepared using DI water provided by the in-house filtration system. All antibody and antigen suspensions use 121°C autoclaved 1xPBS.

Table 2.1: List of materials and chemicals used throughout the project including biofunctionalisation of the SPEs, electrochemical measurements and buffers.

Materials list		
Material	Supplier	Description
220 AT SPE	Metrohm	High temperature
	DropSens	
220 BT SPE	Metrohm	Low temperature
	DropSens	
<i>1-ethyl-3-(3-dimethylaminopropyl) carbodiimide hydrochloride (EDC)</i>	Sigma	98%
<i>2-(N-morpholino)ethanesulfonic acid (MES)</i>	Sigma	98%
<i>6-Mercapto-1-hexanol</i>	Aldrich	97%
<i>11-Mercaptoundecanoic acid</i>	Sigma-Aldrich	95%
<i>Anti-NGAL MAB</i>	R&D Systems	5µg/ml
<i>Bovine serum albumin</i>	-	0.1% (w/v)
<i>Ethanolamine</i>	Sigma-Aldrich	1M solution
<i>di-Sodium phosphate</i>	MERCK	-
<i>Ethanol (EtOH)</i>	-	anhydrous
<i>Ethanol (EtOH)</i>	-	70%
<i>Ferrocenecarboxylic acid</i>	Alfa Aesar	98%
<i>1,1-Ferrocenedimethanol</i>	Acros Organics	98%
<i>Potassium ferricyanide</i>	Sigma	99%
<i>Potassium hexacyanoferrate(II) trihydrate</i>	Sigma-Aldrich	98.5%
<i>Potassium hydroxide (KOH)</i>	Fluka	-
<i>Lipocalin-2/NGAL</i>	R&D Systems	-
<i>N-Hydroxysuccinimide (NHS)</i>	Aldrich	98%
<i>Monopotassium phosphate</i>	VWR	-
<i>Sodium chloride (NaCl)</i>	VWR	-
<i>Sulphuric acid (H₂SO₄)</i>	-	0.05 M

The SPEs used to develop the NGAL biosensor have been acquired from Metrohm DropSens and consist of a gold working electrode with an area of 12.5 mm², a gold counter electrode and a silver pseudo-reference electrode printed on a ceramic substrate with silver contacts. Two SPEs models were used throughout the project incorporating the same materials but different ink curing temperatures. Model 220AT

(high temperature) and 220BT (low temperature). All electrochemical measurements were performed using the Reference 600 high-performance, research-grade potentiostat/galvanostat aquired from Gamry. UV cleaning was carried out in a BioForce Nanosciences UV-Ozone cleaner.

2.2 Surface treatment and chloridization of SPEs

The chips were rinsed with ethanol and DI water prior to the electrochemical surface cleaning procedure. A total of three cleaning procedures were tested. UV-Ozone cleaning was initially employed in order to remove all organic contaminants yet it was proven to affect the stability of the insulating material to the point where visible cracks would appear revealing contact traces, after SAMs formation, affecting the biosensor response. It was also established that gold films can form a stable oxide layer upon UV-Ozone exposure which could not be washed away by water or organic solvents [43]. The other two cleaning methods tested were HCL dipping and electrochemical cleaning in dilute H_2SO_4 . After rinsing the electrodes surface, each chip was subjected to 10 cycles of cyclic voltammetry (CV) in the presence of 60 μ l 0.05 M H_2SO_4 in order to obtain clean gold surfaces. The presence of surface oxides and high amounts of impurities at the surface can hinder the monolayer formation and can negatively affect the biosensor response. On the other hand, a clean gold electrode provides reproducible characterization results and helps in the formation of a closed-packed SAM. The lower and upper potential limits used in the cleaning step were -0.1 and 1.6 V at a scan rate of 100 $mV s^{-1}$. This electrochemical cleaning technique is widely used as it removes both organic and inorganic contaminants, especially oxides, and provides information regarding the surface characteristics of the working electrode. Possible surface gold crystal orientations and the degree of contamination can be approximated from such CV scan [51]. The HCl dipping method is as straightforward as it sounds and it requires the immersion of the SPEs in 1M HCl solution for up to a minute. All cleaning procedures were compared by electrochemical measurements (CV and EIS).

In order to increase the stability and reproducibility of the electrochemical cell during EIS and CV measurements, the silver pseudo-reference electrode was converted to an Ag/AgCl electrode by means of anodic polarization in an aqueous KCl solution. A second attempt for depositing a thin silver chloride layer onto the silver reference electrode was made by increasing the immersion time in HCl by up to 10 minutes. This would in turn clean the WE surface while also forming a [Ag/AgCl] layer on the silver surface. As for the electrochemical anodization procedure, SPEs were subjected to 5 CV scans in the presence of 60 μ l 1 M KCl where the potential was applied across the silver pseudo-reference electrode. An Ag/AgCl saturated KCl (VWR) electrode was used as the reference electrode. CV parameters are shown in table 2.2. Initially, 10 CV scans were employed yet the AgCl formation was observed to decrease after the first 3 cycles after which both the anodic and cathodic currents were on the order of nA, indicating that a stable and insulating AgCl film was formed and no oxidation or reduction reactions occur. The aim of this step was to deposit a thin layer of silver chloride onto the surface of the silver pseudo-reference electrode in order to obtain an Ag/AgCl electrode which is known for its excellent long term potential stability, especially in solution. Following the anodic oxidation step, the electrodes were rinsed with DI water and dried using nitrogen gas. At this point, SPEs were ready for surface functionalization including SAMs formation and bioconjugation of the MAB onto the SAMs.

Table 2.2: CV parameters used for chloridization of the silver pseudo-reference electrode.

Parameter	Value
Scan limit 1	0.5 V
Scan limit 2	-0.005 V
Scan rate	100 mV s ⁻¹
Step size	10
Cycles	5
Max current	10 mA

2.3 Surface functionalization of gold SPEs

Surface modification of the SPEs follows a standard protocol that seeks the immobilization of antibodies onto alkanethiols SAMs. The first step involves the formation of thiol terminated SAMs on the surface of the gold WE with free carboxyl head-groups, thanks to the gold-thiol chemistry, onto which monoclonal Anti-Lipocalin-2 / NGAL antibodies were covalently attached through the formation of an amide bond. Two types of SAMs were employed for antibody attachment. 11-Mercaptoundecanoic (11-MUA) and 6-mercapto-1-hexanol (6-MCH) were used in the SAMs fabrication. Both MUA SAMs and MUA+MCH mixed SAMs were prepared from ethanolic solutions. In the initial stages of this report, it was observed that higher density SAMs are formed, in solution, by mixing ethanol and water in a 4:1 ratio as opposed to anhydrous ethanol. Even better monolayers were obtained at a 1:1 water to ethanol ratio. This behaviour was examined by Lacour et al. [52] on GaAs(100) substrate by FTIR analysis. The higher density was proposed to be achieved thanks to the water-mediated hydrocarbon chains interactions through Van der Waals forces which leads to a higher degree of orientation. In addition, water-mediated interactions between carboxyl groups lead to lateral hydrogen bonding further increasing SAM stability. Based on this observation 80% and 50% ethanol was used as a solvent for 11-MUA and 6-MCH instead of anhydrous ethanol.

2.3.1 Development of 11-MUA SAMs and mixed 11-MUA/6-MCH SAMs

A 2 mM MUA solution was prepared by dissolving 95% MUA powder in 50 ml 80% ethanol. In the case of mixed SAMs, an equimolar mixture of both MUA and MCH was prepared to a final concentration of 2mM in 80% ethanol. As the concentration of the thiol molecule influences the adsorption rate and the kinetics of SAM formation a 2 mM alkanethiol solution seems fitting for this particular application. The solution is dilute enough to prevent multilayer formation yet concentrated enough to promote a fast adsorption step. The pre-treated (cleaned and dried) electrodes were incubated at room temperature in MUA and MUA/MCH ethanolic solutions for 18, 4 and 2 hours in order to observe the effect of immersion time on the insulating properties of the SAM. Incubation time is an important parameter in SAMs formation as time affects the degree of orientation and density of the SAMs which means this parameter could be tuned in further experiments. Approximately 2.7 ml of alkanethiol solution is enough to cover the whole electrode surface area without exposing the rest of the chip. The reaction takes place in 10 ml falcon tubes. After SAM formation, the electrode surface was thoroughly rinsed with ethanol and DI water in order to remove the physisorbed and excess thiols after which it was dried using nitrogen gas.

2.3.2 Carboxyl terminal groups activation reaction, blocking of surface active sites and MAB attachment

The following step involves the attachment of the antibodies onto the SAM through a standard two-step coupling procedure involving EDC and NHS chemistry. Carbodiimide compounds ($\text{RN}=\text{C}=\text{NR}$), especially EDC, provide crosslinking capabilities to carboxylic acids in aqueous solution and therefore is used in the coupling of anti-pocalin-2/NGAL MAB to the 11-MUA SAMs through an amide bond. EDC is used in combination with NHS in the covalent coupling of large biomolecules to surface modified with activated carboxyl groups. This mechanism involves a two-step reaction, the activation of the acid residue and the subsequent formation of an amide. Antibody immobilization was achieved by converting the $-\text{COOH}$ head group of 11-MUA SAMs to activated esters which serve as the leaving group in the crosslinking reaction. The *o*-acylisourea ester (active ester) is displaced by the primary amine through nucleophilic attack in order to form an amide bond with the original $-\text{COOH}$. NHS is included in EDC crosslinking reaction to improve efficiency and yield by creating a stable amine-reactive intermediate. NHS behaves as a catalyst in the coupling reaction by preventing hydrolysis of the amine-reactive ester. The coupling reaction involving EDC is regarded as a zero-length crosslinking reaction since no other chemical group or residue is formed between the reactants. EDC couples NHS to the carboxylic groups of the SAM to form NHS-esters considered to be more stable than the urea intermediate which forms in the absence of NHS [53], [54] [55]. The crosslinking reaction involving all the previous steps is shown in fig. 2.1.

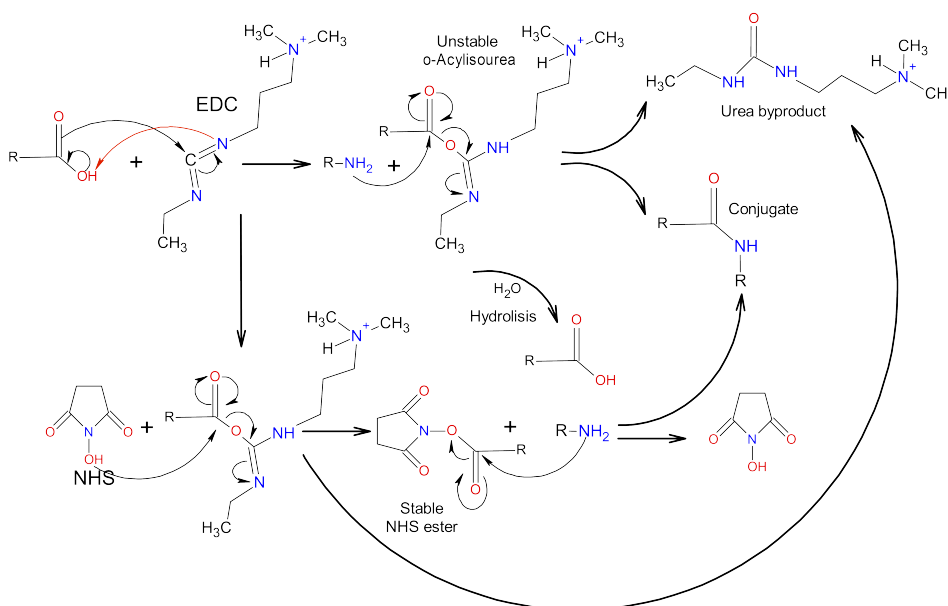


Figure 2.1: Two step reaction for activating the terminal carboxyl groups and coupling of biomolecules onto bifunctional SAMs. Without NHS catalysing the amide bond formation, the *o*-acylisourea intermediate can undergo hydrolysis decreasing the yield of antibody attachment. *O*-acylisourea can also undergo structure rearrangement to form *N*-acylurea when the carbodiimide concentration is much higher than the reacting carboxyl. NHS is included in order to create a two-step reaction in which the main pathway is the amide bond formation.

Adapted from [55].

The electrodes were incubated in 400 mM EDC and 200 mM NHS (2:1 ratio) aqueous

solution for 30 minutes by depositing a 15 μl droplet of coupling solution onto the WE. The coupling solution was prepared by dissolving 98% NHS crystals and 98% EDC power in 250 μl MES buffer (pH 5). Each solution was prepared individually to ensure proper dissolution and to prevent cross-reactivity. After mixing, the coupling solution containing EDC and NHS was used right away since EDC is unstable in aqueous solutions and it is highly reactive at pH 5 with a half-life of 3.7 hours [56]. For each coupling step, fresh solutions were prepared every time to ensure a high MAB attachment yield.

After the surface activation steps the SPES were rinsed with 1x PBS and subsequently incubated with 5 $\mu\text{g}/\text{ml}$ MAB suspension, for two hours, at room temperature. Once the reaction was completed, the WE was rinsed with 1x PBS in order to remove the MAB suspension excess. The next step in the coupling procedure was to quench the unreacted NHS-esters with 15 μL 1M ethanolamine (pH 9) solution for 10 minutes. Lastly, the surface-active sites were blocked with 15 μl of 0.1% BSA solution for 20 minutes. BSA is one of the most widely used antifouling agents in immunoassays, including ELISA protocols. BSA works by preventing non-specific interactions when complex samples are used [57]. The SPEs were rinsed multiple times with 1x PBS to ensure that all the BSA excess is removed. In the case of antigen detection, MAB modified electrodes were incubated with different concentrations of lipocalin-2/NGAL suspension in 1x PBS for 30 minutes. After the antigen-antibody complex formation, the electrodes were rinsed with 1x PBS and EIS measurements were performed. Whenever possible all electrochemical measurements were performed on freshly bio-functionalized chips. When storage was required, the modified SPEs were stored at 4°C with a 50 μl droplet of 1x PBS on the WE surface in order to prevent protein aggregation. A schematic representation of all the steps used in the biosensor fabrication is shown in fig. 2.5.

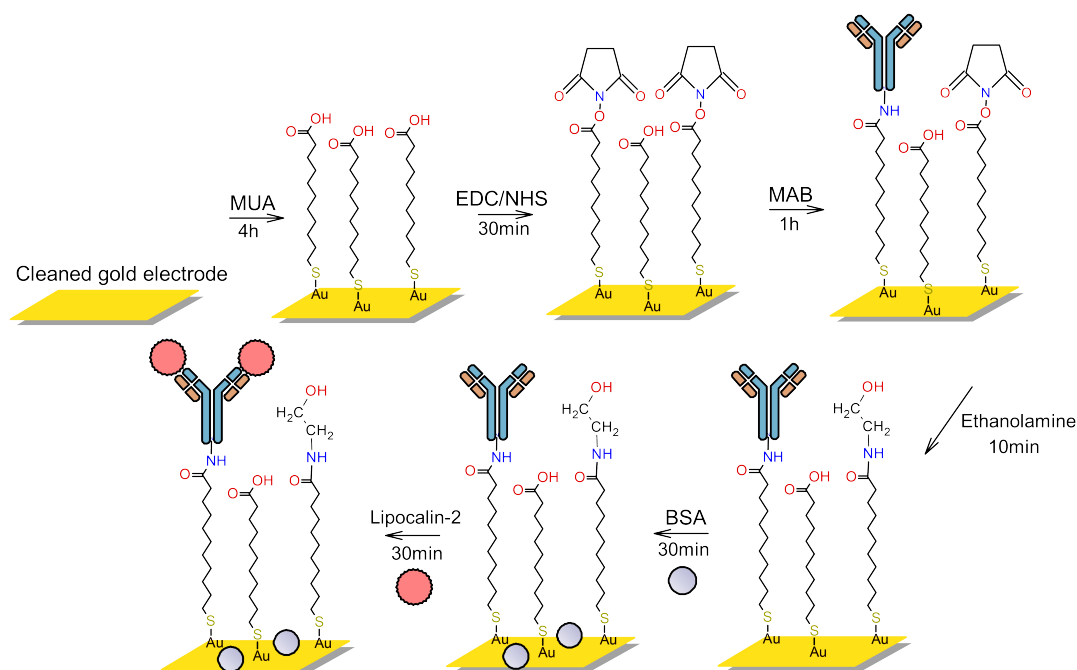


Figure 2.2: Individual steps during the development of the lipocalin-2/NGAL impedimetric biosensor.

2.4 Electrochemical measurements

2.4.1 EIS measurements using potassium ferro-/ferricyanide redox couple

EIS measurements were used as a characterization technique, at different stages, during the development of the biosensor. The evolution of the biosensor was monitored during each modification step by impedance measurements where the change in charge transfer resistance (R_{ct}) was used to define and compare the system under different conditions during functionalization. All measurements were optimized for low noise. The main parameters used during EIS measurements are shown in table 2.3.

Table 2.3: EIS measurements parameters and settings.

Parameter	Value
Initial freq.	100 kHz
Final freq.	0.1 Hz
AC voltage	10 mV RMS
Points decade	2
DC voltage	0.100 V vs E_{ref}
Area	12.5 mm ²

Since this protocol follows the faradaic behaviour of the biosensor, all electrochemical measurements were performed in an aqueous electrolyte solution. The electrolyte solution contains an equimolar concentration of $K_4[Fe(CN)_6]^{-3}$ and $K_3[Fe(CN)_6]^{-4}$. Potassium ferri- and ferrocyanide salts were dissolved in 1xPBS to a final concentration of 5 mM/L. The electrolyte solution was prepared fresh at the beginning of each day. The use of a redox probe during electrochemical measurement enables charge transfer across the working electrode-solution interface. The change in surface properties introduced at different functionalization steps can therefore be monitored. During EIS measurements, a consistent and noticeable drift, especially at low frequencies, could be detected. To overcome this, the system was stabilized by measuring the OCP for 500 s in the presence of redox couple solution [58]. At the end of the OCP measurement, the SPEs display a constant potential revealing that the system has reached a steady-state. The measurements were performed in 50 μ l redox probe solution. The impedance spectra were fitted using the simplex algorithm and the Randles equivalent circuit with mixed kinetics and charge transfer control. The equivalent circuit is shown in fig. 2.3.

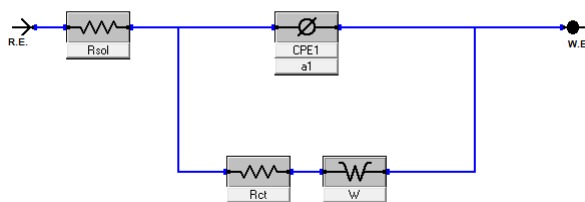


Figure 2.3: Randles equivalent circuit used for EIS data fitting. Components in order: solution resistance (R_{sol}), double layer capacitance as CPE, charge transfer resistance (R_{ct}) and Warburg diffusion element (W).

The impedance spectra were processed using the Gamry Echem Analyst software. All specific electrochemical surface parameters (C_{dl} , R_{sol} , R_{ct}) were extrapolated from the impedance spectra by the fitting functions.

2.4.2 EIS measurements using ferrocene derivatives

Similar EIS measurements were carried out using ferrocenecarboxylic acid (FCA) and a more water-soluble analogue, ferrocenedimethanol (FDM), as redox probes. Since ferrocene by itself is hardly soluble in water (less than 0.1 mg/ml) the electrolyte solution was prepared by initially dissolving 98% FCA powder in anhydrous ethanol. Due to the hydrophilic carboxyl group, a dilute aqueous FCA solution can be prepared if the powder is properly solubilized in an organic solvent before the addition of water or aqueous buffer. The solution was vortexed until all FCA powder was dissolved after which 1x PBS was added to a final concentration of 5mM FCA. The aqueous solution was sonicated for 30 minutes in an ultrasonic bath. This solution served as a stock. The final ethanol concentration, after dilution was 2%. After a few hours, an orange precipitate appears at the bottom of the container for the stock solution since FCA is not fully soluble in water. Before each measurement was performed the dilute 1mM FCA solution was vortexed and once per day, the solution was sonicated to prevent the buildup of the precipitate. Precipitation of FCA is less pronounced at 1mM concentration when compared to the 5mM stock solution. FDM aqueous solution was prepared by dissolving 98% FDM powder in warm 1x PBS. The solution was vortexed and sonicated for 15 minutes. No precipitation occurred in this solution, even after prolonged storage due to the increased solubility of the molecule in aqueous media. EIS measurements were carried out in dilute 1mM FCA and 1mM FDM aqueous solutions in a similar fashion as explained in the previous section. For data fitting of ferrocene EIS spectra, a modified Randles equivalent circuit was used and it is shown in fig. 2.4.

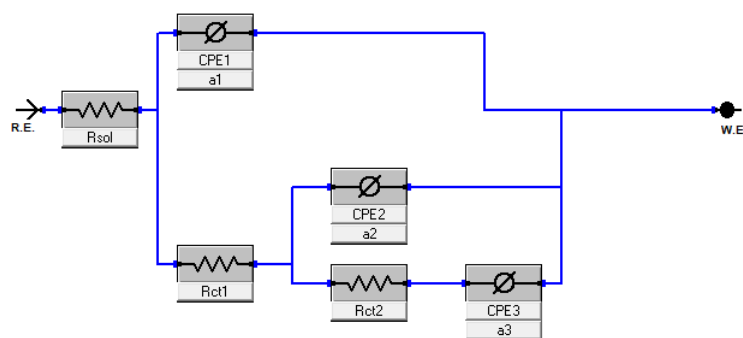


Figure 2.4: Randles equivalent circuit used for EIS data fitting. Components in order: solution resistance, double layer capacitance as CPE_1 , charge transfer resistance at the SAM-electrode interfacier (R_{ct1}), capacitive effect at the SAM-solution interface (CPE_2), charge transfer resistance through the monolayer (R_{ct2}) and the diffusion process (CPE_3) with phase upper and lower limits ($0.4 < a < 0.5$) [59].

This specific circuit contains two RC time constants domains. The first RC arrangement integrates the double layer capacitive effect and the charge transfer resistance at the electrode-monolayer interface, at high frequencies while the second RC arrangement integrates the monolayer capacitive behaviour and the charge transfer resistance

through the SAM, at the monolayer-electrolyte solution interface [59], [60]. The first semicircle region was also attributed to an RC parallel arrangement between the solvent double-layer and the polarization resistance of the electrode [61]. This equivalent circuit was used to accommodate the appearance of a second semicircle at high frequencies, in the spectra obtained using ferrocene derivatives.

2.4.3 CV measurements

CV was employed as characterization and as a surface cleaning method as previously mentioned. CV scans of potassium ferri-/ferrocyanide redox couple and ferrocene derivatives were carried out at different steps during the surface functionalization. CV was also employed to study the electrochemical characteristics of 220 AT and 220 BT electrodes prior to any modification. CV parameters used during SPEs characterization are shown in table 2.4. CV was also employed to study the potential shift of different reference electrodes configurations, before and after chloridization. The formal reduction potential of each redox probes was used as a DC bias potential during EIS measurements and was determined from cyclic voltammograms.

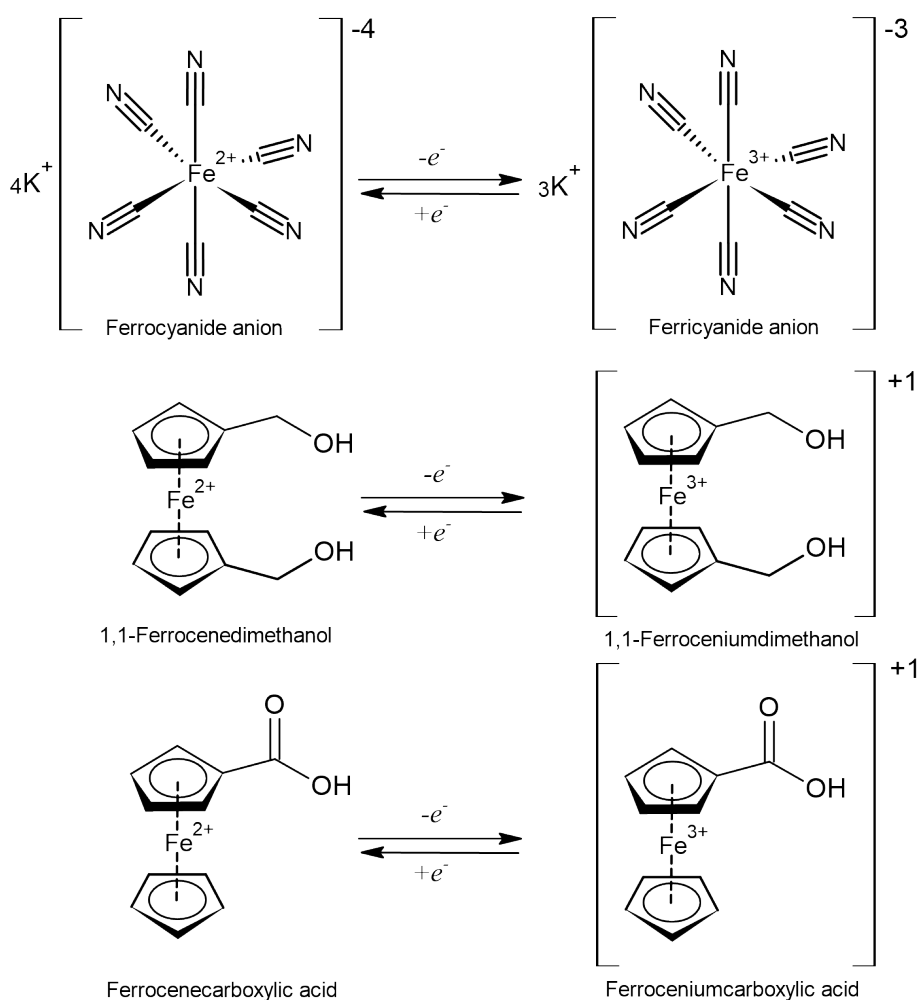


Figure 2.5: Reversible redox reactions of ferri-/ferrocyanide redox couple and two ferrocene analogues (ferrocenedimethanol and carboxyferrocene) used in electrochemical sensing.

Table 2.4: CV parameters used during SPEs electrochemical characterization.

Parameter	Value
Scan limit 1	0.4 V
Scan limit 2	-0.2 V
Scan rate	100 mV s ⁻¹
Step size	10
Cycles	5
Max current	10 mA

RESULTS AND DISCUSSION

3.1 Characterization of the surface cleaning methods

The first stage in the development of the biosensing platform was the surface cleaning of the working electrode. Three different cleaning procedures were employed and compared in order to find the most suitable method. Cleaning voltammograms in H_2SO_4 for both SPEs types can be seen in fig. 3.1 **A** for the AT and **B** for BT models. Both SPEs were treated within the same potential range, yet it can be observed that the electrochemical behaviour of each electrode is different. Both SPEs present a high oxygen evolution at high applied potentials, which is to be expected in an aqueous solution. The onset of the oxygen evolution for the BT model is roughly around 1.4 V while the water electrolysis occurs much faster for the AT model with an onset around 1.2 V. The measured current is expected to be higher for the AT chip since the oxygen evolution starts at a lower potential, which seems to be the case pointing towards a faster electron transfer rate. An interesting observation regarding the oxide formation during electrochemical cleaning is that gold oxide formation and subsequent reduction are visible for the BT SPEs while the AT model does not exhibit an obvious electrochemical response other than the electrolysis of water at high potential.

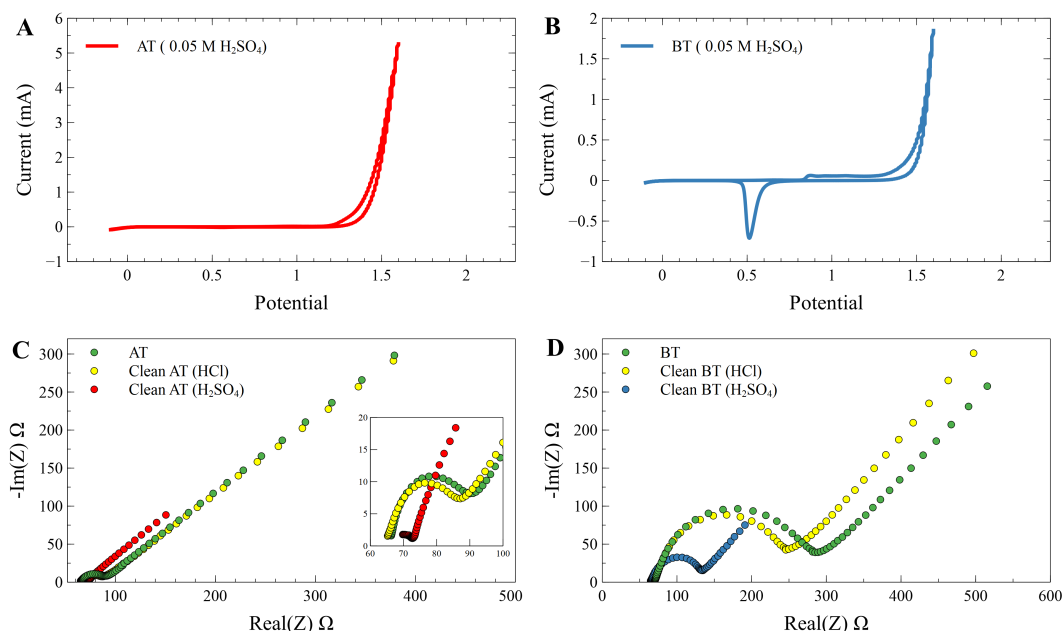


Figure 3.1: Cycling voltammograms of AT (**A**) and BT (**B**) SPEs during potential cycling in 0.05 M H_2SO_4 . EIS spectra of AT (**C**) and BT (**D**) before (green dots) and after the surface cleaning process including potential cycling in H_2SO_4 (blue and red dots) and HCl dipping (yellow dots). AC amplitude: 5mV (rms). Frequency range $10^5 - 0.1$ Hz.

This difference in behaviour might be explained by the rather different temperatures used in the ink curing process. Since the AT model is cured at a higher temperature, it is probable that the ink contains fewer oxides. On the other hand, the BT model is manufactured at lower temperatures which would point towards a higher degree of surface contaminants and adsorbed molecules. This could be the case since the measured signal amplitude (current) for the gold oxide formation and reduction to metallic gold for the BT SPEs are 65 μA and 815 μA respectively, while these peaks are absent for the AT electrode. The same electrochemical behaviour was observed for both electrodes by Butterworth et al. [51].

The efficiency of two cleaning methods namely HCl dipping and potential cycling in H_2SO_4 , was determined by EIS measurements as seen in fig. 3.1 C and D. Regarding the UV-ozone treatment, no data is available since in combination with the ethanol used as a solvent during monolayer formation, the insulating layer of the SPEs would crack rendering the SPEs inoperative. Data on the effect of different organic solvents on the SPEs is not widely available, yet the substrate separation was not observed during monolayer formation when the SPEs was previously cleaned using one of the other two methods. The efficiency of the UV cleaning procedure was assessed and discussed in a number of papers that proposed a below-average cleaning efficacy for electrochemical applications [43], [62]. Since other and probably better alternatives do exist, the UV-ozone treatment was not further used. The EIS spectra shown in fig. 3.1 C and D would suggest a moderate degree of surface contamination out of the box, especially for the BT electrodes. A broader semicircle region with a much higher R_{ct} value is observed for the untreated BT SPE when compared to the untreated AT model. R_{ct} decreases slightly after HCl dipping, from 202 Ω for the out of the box SPE, to 163 Ω , for the BT model. This difference is even less pronounced for the AT electrode where R_{ct} decreases from 30 Ω to 24 Ω . As mentioned before, this difference between electrodes should come from the manufacturing process. As the AT electrodes is produced at high temperature a cleaner and smoother surface is obtained which in turn is reflected by a lower impedance and a faster electron transfer. It can be observed that a cleaner surface is obtained after potential cycling in H_2SO_4 for both electrodes. The charge transfer resistance for the AT electrode is practically non-existent after this treatment and the electron transfer rate increases for both models. The whole electrochemical process is diffusion-controlled for the AT electrode while R_{ct} decreases to 83 Ω for the BT SPE. This indicates that overall, the electrochemical stripping with H_2SO_4 produces cleaner surfaces when compared to HCl dipping.

This is in agreement with the results obtained by Fischer et al. [62]. The group successfully used different inorganic compounds for electrochemical surface cleaning such as reducing agents or peroxides yet potential cycling using H_2SO_4 was found to be the most robust approach as shown by XPS analysis. Chloride compounds such as HCl were found to etch the gold surface more aggressively than H_2SO_4 . This was not observed in this report since no potential was applied during HCl treatment. Cl atoms can also end up embedded in the gold surface, changing the electrochemical behaviour of the gold electrode [63]. Peroxide treatment tends to produce thick oxide layers while reducing agents produce less clean surfaces when compared to H_2SO_4 aqueous solution [62].

Similar results were also reported by Carvalhal et al. [64]. The group focused on the impact of electrode pretreatment on the 3-MPA monolayer formation. After comparing different types of electrode cleaning methods (mechanical, chemical and electrochemical) the final conclusion was that potential cycling in sulphuric acid yields a

much cleaner surface when employed in combination with mechanical cleaning using alumina slurry and chemical treatment in piranha solution. Their results are also representative of the SPEs format since the group focused on monolayer formation on polycrystalline gold electrodes. The reductive desorption of 3-MPA monolayers was carried out in a basic environment where each reduction peak is proportional to the monolayer surface coverage. Their results suggest that a more closely packed monolayer, with higher surface coverage, is formed when the electrochemical cleaning method is employed.

3.2 Electrochemical characterization of gold AT and BT SPEs

3.2.1 Chloridization of the pseudo-reference silver electrode

The chloridization procedure seeks to deposit a stable AgCl layer onto the silver reference electrode. Cyclic voltammetry was employed to test the stability and eventual drift of the electrochemical cell following this procedure. CVs of both SPEs (AT and BT) were recorded in 5 mM potassium ferri-/ferrocyanide redox couple and PBS solution at a scan rate of 100 mVs^{-1} as shown in fig. 3.2. The electrochemical behaviour of the redox couple was compared by experimenting with both the onboard reference electrode and the external KCl saturated Ag/AgCl reference electrode. After the anodic treatment of the pseudo-reference electrode, a colour change was noticed and attributed to the formation of a thin AgCl film. Pictures with the electrodes before and after the electrochemical treatment can be seen in fig. A.1

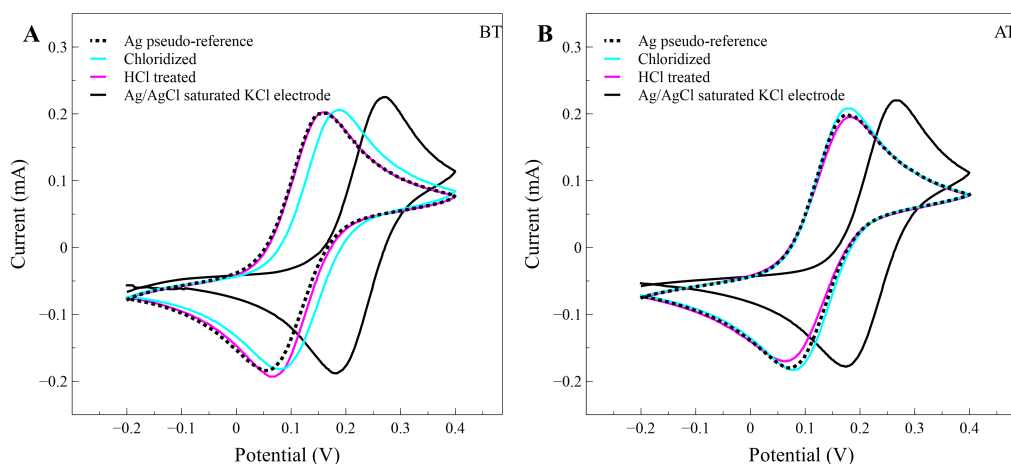


Figure 3.2: Cycling voltammograms of BT (A) and AT (B) SPEs during potential cycling in 5 mM ferri-/ferrocyanide solution. The electrochemical behaviour of each SPE was tested using the on board Ag-reference electrode (dotted lines), after chloridization using potential cycling in KCl (cyan lines), after HCl treatment (magenta lines) and using a saturated 3M KCl Ag/AgCl external reference electrode (solid black lines).

From fig. 3.2 A and B it can be observed that despite the chemical treatment of the silver pseudo-reference electrode, there is still a noticeable potential shift when compared to the external Ag/AgCl reference electrode. Upon a closer look in table 3.1, it can be observed that after the electrochemical anodization of silver in KCl, the potential shift of ferrocyanide oxidation to ferricyanide (E_{pa}) drops to 82 mV for

both electrode models. This method is more consistent when compared to the HCl treatment which seems to have less of an impact (2 and 8 mV decrease in potential shift).

Table 3.1: Electrochemical characteristics of BT and AT SPEs obtained after potential cycling in 5 mM potassium ferri-/ferrocyanide redox couple in 1X PBS.

Electrode	E_{pa} (mV)	E_{pc} (mV)	ΔE (mV)	E'_o (mV)	Shift (mV)
BT					
Internal(Ag)	158.1	52.4	106	105	107
Internal (KCl)	184	84.4	99.4	134	82
Internal (HCl)	161.1	64.4	97.6	113	105
External	266	181	85	223	-
AT					
Internal(Ag)	174.1	68.4	105.6	121	92
Internal (KCl)	184	84.4	100	128	82
Internal (HCl)	182.1	62.4	121.6	123	84
External	266	173.3	89.7	221	-

The biggest potential shift post chloridization is seen for the BT SPE while the AT SPE seems to have a less pronounced drift out of the box. Metrohm, the SPEs manufacturer, acknowledges a potential shift of roughly -131 mV for the onboard silver reference electrode, yet both the AT and BT models exhibit less drift than anticipated, before and after any chemical treatment. While the chloridization treatment seems to improve the electrochemical behaviour of potassium ferri-/ferrocyanide redox couple for both electrodes, the changes in the potential shift are minimal. When compared to the untreated silver pseudo-reference electrode, the potential shift narrows by approximately 25 mV for the BT electrode and merely 10 mV for AT electrode. There was no incentive to modify the onboard silver pseudo-reference electrode from an electrochemical standpoint since the drift was still present post chloridization. Nonetheless, the biosensor was developed using the silver pseudo-reference electrode. The reversibility of the redox reaction can also be determined from fig. 3.2. A ΔE value of roughly 105 mV was determined for both electrodes. While for a redox reaction to be fully reversible the electron transfer has to occur extremely fast and the peak separation should be around 59 mV at 25 °C, as described by the Nernst equation [65]. The peak-to-peak separation for both AT and BT SPEs is not ideal, yet it is still, to some extent, a reversible process as shown by both CV scans. A small difference between the anodic and cathodic peak currents is observed in the voltammograms hence the increase in ΔE when compared to a classical electrochemical cell. Nonetheless, the electrochemical behaviour of both electrodes is within expectations and is consistent enough for biosensing applications.

3.2.2 Redox behaviour of potassium ferro-/ferricyanide and ferrocene analogues

The electrochemical behaviour of the other two redox probes, namely ferrocenecarboxylic acid (FCA) and 1,1'-ferrocenedimethanol (FDM), was assessed, on gold BT SPEs, by potential cycling. CV scans of all three redox probes used in the experiments are shown in fig. 3.3. The redox response of ferro-/ferricyanide was determined in the previous section, yet here it is compared against two ferrocene derivatives. The parameters obtained for each CV scan are shown in table 3.2. The reversibility of the system is assessed from the difference in potential between the anodic and cathodic peaks or

ΔE . For a fully electrochemically reversible couple the ΔE value should be close to 59 mV in ideal circumstances, yet this is not always observed. Values of ΔE of 106, 71.9 and 65.7 mV are obtained for the ferro-/ferricyanide couple, carboxyferrocene and ferrocenedimethanol. We can assume that the electron transfer rate is faster for the ferrocene analogues, resulting in a smaller peak to peak separation. In this case, all three redox probes behave as reversible from an electrochemical standpoint with ferrocenedimethanol displaying the best reversibility out of the three.

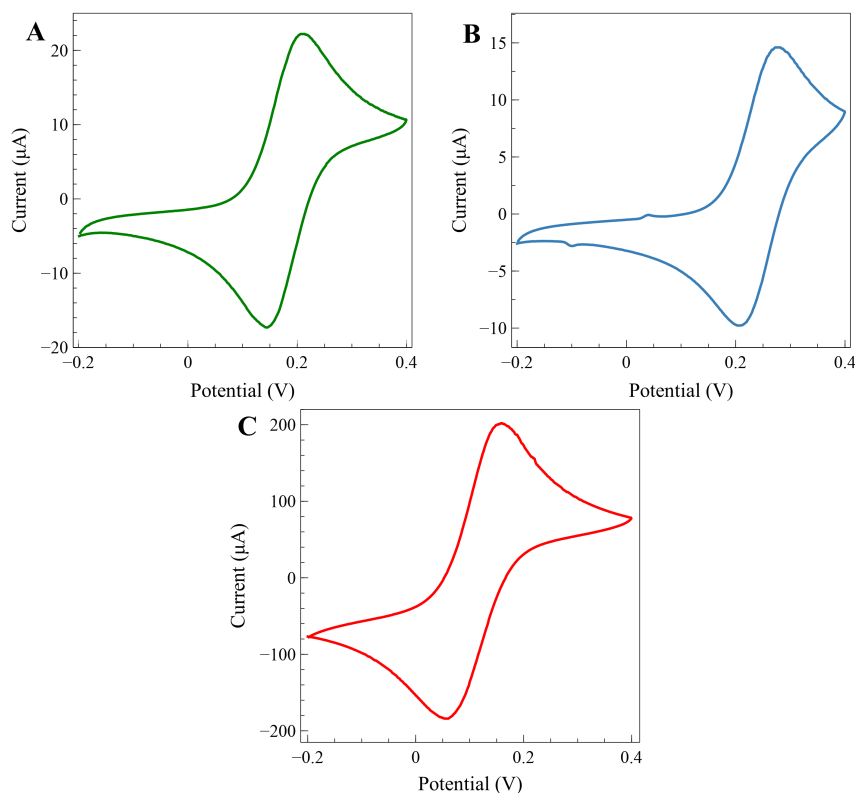


Figure 3.3: CVs of 1mM 1,1'-ferrocenedimethanol (A), 1mM ferrocenecarboxylic acid (B) and 5mM ferro-/ferricyanide (C) in 1x PBS aqueous solutions. Scan rate: 100 mV s^{-1} .

The formal reduction potential, E'_o , was calculated for each redox reaction, in the same potential range. The values are shown in table 3.2. E'_o was calculated so it could be used as bias potential during EIS measurements. This was done to maintain the equilibrium between the forward and backward reaction rates thus maintaining the ratio between oxidized and reduced species. For a reversible redox reaction, the formal reduction potential can be calculated from a CV scan with the help of eq. (3.1).

$$E'_o = \frac{E_{pa} + E_{pc}}{2} \quad (3.1)$$

An important remark is that while ferrocene analogues were measured at 1mM concentration, the ferro-/ferricyanide solution concentration was 5mM. While the electron transfer kinetics generated from a redox reaction is not affected by the bulk concentration, the amount of current will be different due to mass transport and diffusion

mechanisms. This can be seen in fig. 3.3 where the anodic current generated by ferrocyanide is tenfold higher when compared to the two other compounds. This should not affect any of the results reported so far since reversibility and E'_o are not related to the bulk concentration but are influenced by charge transfer kinetics.

Table 3.2: Electrochemical characteristics of BT SPEs obtained after potential cycling using three redox probes.

Redox probe	E_{pa} (mV)	E_{pc} (mV)	ΔE (mV)	E'_o (mV)
Potassium ferro- /ferricyanide	158.1	52.4	106	105
FCA	278	206.1	71.9	242
FDM	207.9	142.2	65.7	175

3.2.3 Electrochemical active surface area measurements

The electrochemical active surface area (ECSA) of both electrodes was determined by potential cycling in 5mM potassium ferro-/ferricyanide redox couple solution by plotting the response of the anodic peak current against the square root of different scan rates (10, 20, 40, 80, 120, 160, 200, 300 and 400 mV s^{-1}). The electrochemical active surface area is usually different from the measured geometrical area (GA) of the working electrode. The difference comes from the non-homogeneous surface topology, in this case, the surface roughness. Since both electrodes are obtained from a paste-like precursor, the surface is expected to be more porous when compared to thin-film electrodes obtained by vapour deposition methods. In this case, a comparison between the AT and BT models is made on the basis of ECSA and the roughness factor (RF). The surface characteristics of the electrodes could have been determined by AFM imaging however due to the high variability in surface topology it was not possible. In fig. 3.4 the linear relationship between the anodic peak current and the square root of the scan rate can be observed. From the slope of the linear fit ($y = mx + b$) ECSA was calculated as described in eq. (3.2) also known as the Randles-Sevcik equation.

$$I_{pa} = (2.69 \times 10^5) n^{\frac{2}{3}} A_{eff} D^{\frac{1}{2}} \nu^{\frac{1}{2}} C_o \quad (3.2)$$

Where n is the number of electrons transferred during the redox reaction, A_{eff} is the electrochemically active surface area and D and C_o are the diffusion rate coefficient and the bulk concentration of the redox probe. Both electrodes exhibit a linear behaviour at low and high scan rates with R^2 values approaching unity. From a D value of 7.6×10^{-6} [66], $n = 1$ and a bulk concentration of 5 mM redox probe solution, the slope of both fitted regression lines were calculated and shown in fig. 3.4. The A_{eff} of the BT model was found to be around 16.27 mm^2 and 14.66 mm^2 for the AT electrode vs the specified GA of 12.5 mm^2 . This further confirms that due to the differences in the manufacturing process, both electrodes inherit a different surface topology.

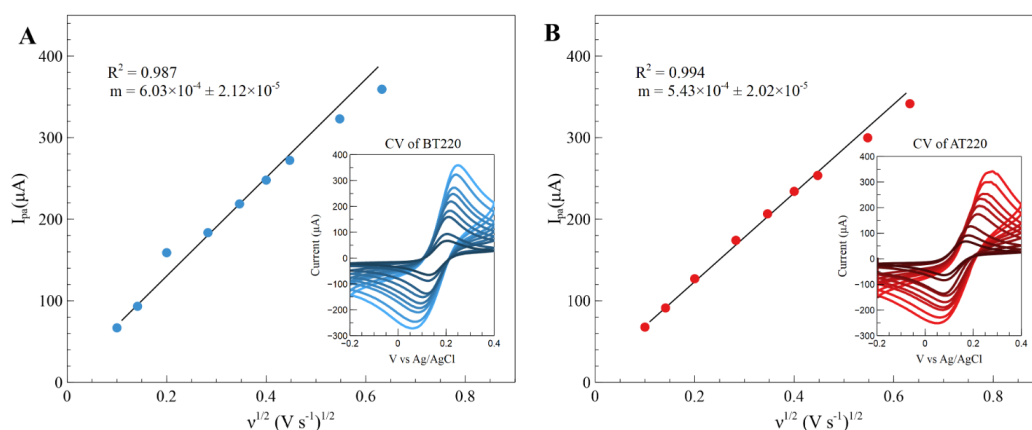


Figure 3.4: Linear regression showcasing the relationship of the anodic peak current (I_{pa}) and the square root of the scan rate as described by the Randles–Sevcik equation. Insets show the CV response of BT (A) and AT (B) electrode in 5 mM potassium ferro-/ferricyanide solution in 1x PBS at different scan rates.

The geometrical surface area was calculated from the diameter of the working electrode (4 mm) and is roughly 12.5 mm^2 . The difference between ECSA and GA comes from the surface defects and surface roughness. The roughness factor (RF) of both electrodes was calculated using the ECSA and GA values as explained in [67]. The RF values of 1.17 and 1.3 were calculated for the AT and BT electrodes. This indicates an increase in surface roughness of approximately 11% for the BT electrode over the AT one. The difference in both ECSA and RF between the two electrodes would suggest a faster electron transfer which is directly proportional to the RF values. Since an increase in surface defects leads to an increased surface area one would expect a faster electron transfer for the BT electrode [64]. However, this is not the case as seen in fig. 3.1. The R_{ct} value is greater for the BT electrode than for the less rough AT, which actually shows a faster charge transfer indicated by the low impedance. This would suggest that the electrodes are more different than previously anticipated and that a difference in chemical composition might influence the electrochemical behaviour of both electrodes. Similar results were reported by Kadara et al [26]. The group compared carbon-based SPEs from different manufactures in terms of electrochemical characteristics and surface topology. While most electrodes show a relation of proportionality between ECSA and electron transfer rates, one outlier was identified. On the basis of STM imaging and electrochemical measurements, it was suggested that the polymeric binder used in the pastes would hinder the electron transfer process despite the high ECSA value. This is in line with the results reported after the cleaning procedure. This might also be the case for the gold SPEs used in this report. Nonetheless, the increased ECSA and RF of the BT SPEs would later be reflected in more binding sites for the alkanethiols used during monolayer formation. On this assumption, a more compact and insulating layer would be expected in the case of the BT SPEs thus increasing the MAB surface coverage. Following this assumption and due to the fact that most work regarding the biosensor optimization was done on 220 BT SPEs, this particular model was chosen as the biosensing platform.

3.3 Optimization and characterization of 11-MUA SAM and 11-MUA/6-MCH mixed SAM using BT SPEs

11-MUA monolayers were obtained using cleaned BT SPEs and different immersion times in ethanolic solution. The monolayers were characterized using EIS measurements. The degree of surface coverage is inversely proportional to the electron transfer rate during the redox reaction suggesting that a faster charge transfer occurs when an incomplete monolayer is formed due to pinholes or imperfections.

Impedance spectra of 11-MUA SAMs obtained at different immersion times can be seen in fig. 3.5. These measurements would suggest an increase in R_{ct} proportional to the immersion time. It was expected that a more insulating layer would form after a longer immersion. Metrohm suggests that organic solvents have the ability to break the SPEs under certain conditions (long exposure and immersion time). This happened a number of times during this step. These measurements were performed in order to observe if closed packed monolayers could be obtained after a faster immersion time in 80% ethanol solution or after a longer exposure at a lower ethanol concentration (50%). This optimization step was performed to limit the number of SPEs being damaged during SAM preparation without sacrificing the monolayer coverage on the WE.

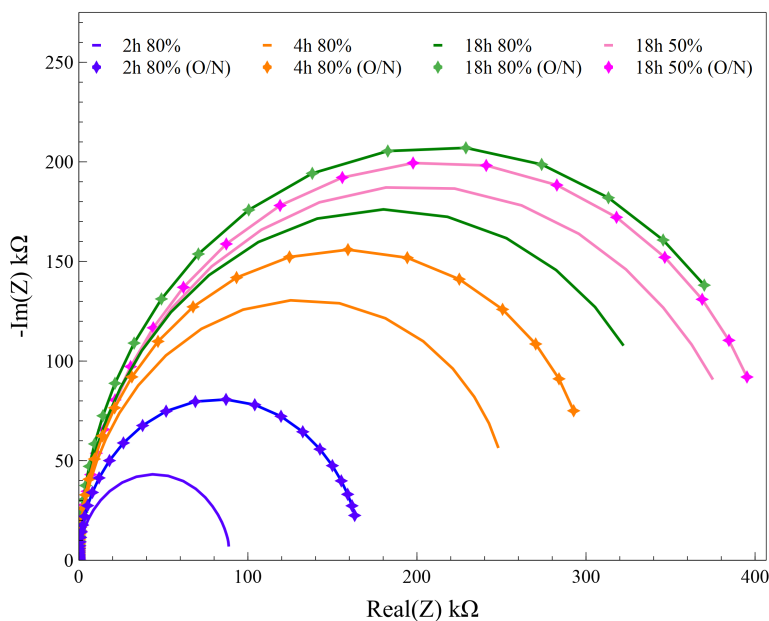


Figure 3.5: Nyquist plots of 11-MUA monolayers formed from 80% and 50% ethanolic solution on BT SPEs. The plots highlight the insulating properties of SAMs obtained at different incubation times. SAMs formed after 2h (blue), 4h (orange) and 18h (green) incubation times in 80% ethanol are shown as lines and the same SAMs were measured after 24h to assess stability and are shown as starred lines with their corresponding colors. SAMs obtained after 18h of incubation in 50% ethanol are also shown (magenta lines). The EIS measurements were carried out in 5 mM potassium ferro-/ferricyanide solution in 1x PBS. AC amplitude: 10 mV (rms). Frequency range $10^5 - 0.1$ Hz.

As it can be observed in table 3.3 the fitting data suggests that a highly insulating monolayer is formed after only two hours of immersion. Yet a two- and a threefold increase in R_{ct} is observed after 4 and 18 hours of incubation in 80% ethanol 11-MUA solution. From fig. 3.5 it can be noticed that the semicircle region for the 2h 11-MUA SAM is complete and would most likely move towards a diffusion-controlled regime if the measurement would have been carried at even lower frequencies. This would indicate a small but limited charge transfer across the interface which in turn would deplete the redox probe in the immediate proximity to the surface. This behaviour is not observed for the 4 and 18 hours immersion times, where the semicircle region is not complete, indicating a high charge transfer resistance even at low frequencies. This indicates that a much slower electron transfer occurs for these two SPEs which is indicative of a closely packed monolayer that limits the current flow at the WE thus no diffusion-limited process is present. In other words, the oxidation and reduction reactions, of the redox couple, occur much slower due to limited surface access. Even if after 4 hours, the charge transfer resistance reaches 264.1 k Ω indicating an increase of roughly 189.7% over the 2 hours sample, it appears that there are still some unoccupied sites onto the gold surface or that the monolayer is still undergoing reorientation from the laying down phase. The R_{ct} value reaches 365.9 k Ω after 18 hours which is equivalent to a 35% increase over the R_{ct} of the SAM obtain after 4 hours. This implies that 18 hours was a good starting point for developing the biosensing platform however, due to the organic solvent (ethanol) used in this step, more often than not, SPEs would be damaged in different forms: either the substrate layers would peel off or the binder used in the ink would loosen, cracking the WE thus negatively impacting the performance of the sensor. To overcome these shortcomings, different incubation periods were tested. As it can be observed from the fitting results shown in table 3.3 and the Nyquist plots in fig. 3.5, the change in R_{ct} from 2 to 4 hours of incubation is far greater than from 4 to 18 hours, suggesting that most if not all adsorption sites are occupied after only 4 hours of immersion in 11-MUA solution. After 18 hours of incubation in 80% ethanol, more than half of the SPEs would be damaged. Nonetheless, some SPEs would also break after 4 hours in 80% ethanol, yet this seemed the most appropriate approach at this ethanol concentration. The only trade-off is a very small decrease in surface coverage when compared to SAMs obtained after a longer immersion.

Another attempt was made using an 11-MUA solution containing 50% ethanol. The Nyquist plots for this experiment are also shown in fig. 3.5 as magenta lines. The results were surprisingly good for such low ethanol concentration. Not only all the SPEs incubated in this solution were not damaged but also the 11-MUA coverage was higher and more reproducible when compared to 4 hours of incubation in 80% ethanol, the maximum time allowed at this concentration without damaging the SPEs. The R_{ct} difference between freshly made 11-MUA SAMs after 18 h of incubation in 80% and 50% ethanol is 32.8 k Ω which is equivalent to an 8.4% increase in monolayer coverage for the 50% solution. These results suggest that an ordered and insulating SAM can be formed in solution, at high water content, without damaging the SPEs. EIS spectra for SAMs obtained in 50% ethanol and lower incubation times are not shown since there was no incentive to lower the reaction time and obtain less stable SAMs since after 18 h SPEs remain intact.

Another reason for why SAMs were obtained from 80% and 50% ethanol and not anhydrous ethanol solution, aside from the reduction in SPE deterioration is due to the influence of solvent polarity on the quality of the monolayer. Since it is important for charge transfer to occur in faradaic biosensors for quantitative measurement,

Table 3.3: Fitting values of the Randles equivalent circuit elements of 11-MUA monolayers obtained at different immersion times and different ethanol concentrations (80 and 50%).

Immersion time	$R_{sol}(\Omega)$	$R_{ct}(k\Omega)$	$C_{dl}(\mu F cm^{-2})$	$\theta\%$
2h-80%	24.5	92.15	2.52	99.891
2h-80% (O/N)	31.75	168.6	2.4	99.940
4h-80%	25.4	264.1	2.48	99.962
4h-80% (O/N)	25.6	316.7	2.5	99.968
18h-80%	24.4	356.9	2.7	99.971
18h-80% (O/N)	24.8	419.5	2.68	99.976
18h-50%	24.4	389.7	1.7	99.973
18h-50% (O/N)	24.8	401.5	1.5	99.975

SAMs defects are not desirable even if they promote electron transfer processes to occur. Monolayer defects promote instability and affect the reproducibility of the sensor by having a negative effect on the MAB coverage. To overcome this aspect, a water and ethanol mixed solution was used as a solvent for 11-MUA and 6-MCH. Following Dubowski et al. [52] study on water-mediated mixed monolayer formation on GaAs(100) surface, it was concluded by FTIR analysis that 11-mercapto-1-undecanol (-OH terminated) and the longer 16-hexadecanoic acid (-COOH terminated) form tightly packed SAMs in the presence of water molecules. This is believed to come from the water-mediated lateral hydrogen bonding between the terminal functional groups, especially in the case of carboxyl terminates SAMs such as 11-MUA. An increase in SAM thickness was observed by the group, until 40% water content after which the degree of disorder in the monolayer increased [52]. Carvalho et al. [64] suggested that competition is established between SAM and gold oxide formation during 3-MPA monolayer evolution on polycrystalline gold electrodes when aqueous 3-MPA solution was used. This would suggest that while the presence of water favours the formation of a closely packed monolayer, the low solubility of organo-sulfur compounds in water hinders the intermolecular interactions when the water concentration is too high, leading to monolayer defects or gold oxide formation on the electrode. In this report, SAMs were successfully obtained even at high water concentration (50%) without apparent downsides. It is possible that gold oxide can form alongside the self-assembled structure and it can contribute to the measured impedance. However, this protocol was used in order to accommodate the fact that SPEs are not designed to be used in combination with organic solvents.

CV scans before and after 11-MUA SAM formation on BT SPEs were also recorded and are shown in fig. 3.6. No reduction or oxidation peaks are present in the interrogated voltage range after 11-MUA SAM formation. This behaviour suggests that an ordered and highly insulating monolayer is formed after only two hours of incubation. The impedance data is in agreement with the electrochemical behaviour of 11-MUA SAMs during potential cycling. Similar results were reported in [34], [68] and [69].

The C_{dl} values shown in table 3.3 are representative for 11-MUA SAMs. The capacitive effect comes from the insulating behaviour of the SAM which corresponds to a dielectric material between conducting media, similar to a conventional plate capacitor. Once the majority of the surface sites are occupied by adsorbed species, C_{dl} decreases from around 20-60 $\mu F cm^{-2}$ for a bare gold surface to a value dependant on the adsorbed molecule. The decrease is proportional to the number of carbon atoms

in the alkyl chain [69]. C_{dl} values obtained after the equivalent circuit fitting are close to or within the expected range, which is between 1-5 $\mu F cm^{-2}$ for 11-MUA SAMs chemisorbed on gold electrodes according to S. Campuzano et al. [70].

Assuming that charge is transferred only through monolayer defects, such as pinholes, the SAM percentage coverage was calculated from eq. (3.3) for each incubation time and the results are shown in table 3.3 [69]. After only two hours of incubation, more than 99 % of the surface area is covered by the monolayer. This indicates even faster chemisorption than initially anticipated. These results are in accordance with other similar studies regarding 11-MUA SAMs formation on gold electrodes [69], [70].

$$(1 - \theta) = \frac{R_{ct(blank)}}{R_{ct(11-MUA)}} \times 100 \quad (3.3)$$

As stated by Chen et al. [34] the minimum amount of time required to form an effective thiol based SAM on gold surfaces is 6 hours, while E. B Bahadir and M. K. Sezgintürk [68] observed that a stable and insulating 11-MUA SAM can be obtained after only two hours of incubation. The latter successfully employed 11-MUA SAMs obtained after 2 hours of incubation in the development of an impedimetric biosensor for the detection of vascular endothelial growth factor with a linear detection range between 1 and 6 ng/ml. Another important remark is that the monolayer is affected not only by the incubation time but also by its concentration in solution, the area and topology of the gold surface and the thiol molecule itself. Ulman [43] proposed how the length of the molecule affects monolayer formation. It was suggested that for long-chain alkanethiols such as 11-MUA, the chemisorption process is much faster when compared to shorter thiol derivatives, such as 3-Mercaptopropionic acid or 2-mercaptoethanol, which are often used in biosensing applications. Regarding the solution concentration, a fast adsorption, on the order of minutes, was observed at 1 mM n-alkanethiol concentration while the process slows down considerably at μM concentrations [43]. This implies that the 2 mM 11-MUA solution used during SAMs formation is concentrated enough to provide fast adsorption yet sufficiently dilute to not promote multilayer formation [43], [46], [31]. The intermolecular interactions are also stronger for longer chained organo-sulphur compounds which translate in a faster reorientation of the surface and a more stable SAM [42]. This all indicates that a stable and insulating SAM could be obtained after only 4 hours of incubation, yet later throughout the project, it was found out that by reducing the ethanol concentration to 50%, all of the SPEs would survive this step without being damaged, even after prolonged incubation (18h). All things considered, the biosensor was developed using 50% ethanolic, 11-MUA and 11-MUA/6-MCH solution and an incubation period of 18 hours.

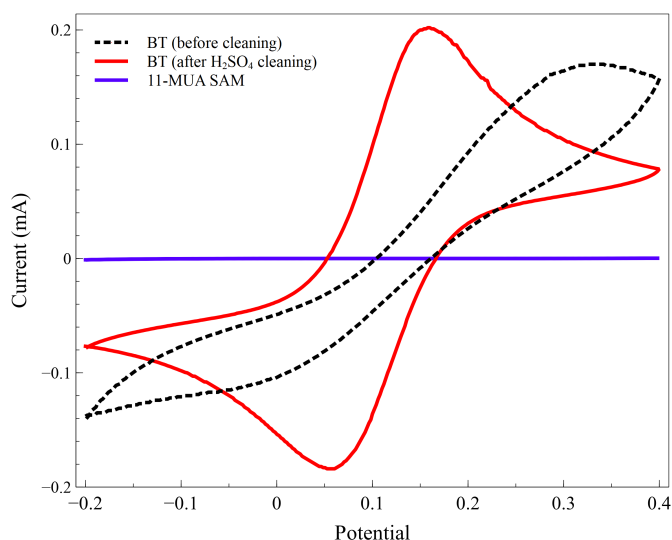


Figure 3.6: CV scans of ferro-/ferricyanide redox couple in 1x PBS on BT electrodes before cleaning (black dotted line), after electrochemical cleaning in H₂SO₄ (red line) and after incubation in 2mM 11-MUA solution for 2 hours (blue line). Scan rate: 100 mV s⁻¹.

Since the SAM formation occurs within minutes of incubation while the reorientation of the molecules takes longer, on the order of hours to days [43], the second set of impedance measurements was performed after storing the SAM modified SPEs for 24 hours at 4 °C with a 50 μ l drop of PBS onto the WE. The complex impedance plots are compared with the ones from freshly prepared SAMs in fig. 3.5. An increase in charge transfer resistance is seen for SAMs obtained at different incubation times, after 24 hours. This could be explained by the possible transition of select nucleation sites from the stripped phase to the closed packed phase [52]. An increase in R_{ct} of 77.45, 52.7 and 62.6 k Ω is observed, corresponding to the SAMs obtained after 2, 4 and 18 hours of incubation in 80% ethanol solution. This corresponds to a percentage increase of 84 %, 19.9% and 17.4%. The R_{ct} increase for each SAM suggests a surface rearrangement of thiols to a more compact structure. An increase of 11.8 k Ω was measured for SAMs obtained in 50% after 24h storage. This is equivalent to a 2.9% increase in R_{ct} . This could be caused by a number of reasons such as the electrostatic repulsion between the carboxyl functional groups and the chemisorbed and slightly negative mercaptan functional group [42]. Based on the fact that 11-MUA has a pKa value of 4, its carboxyl-terminal group is deprotonated while in PBS which has a pH value of 7.4 [71]. This would explain the impedance increase over time while stored in 1x PBS on the basis of charge induced rearrangement. A second possibility is the rearrangement of the alkyl chain due to hydrophobic interactions while the carboxyl groups become solvated. This mechanism was studied by Li et al [72] by molecular dynamics simulations of adsorbed alkanethiols in water. In this study, carboxyl terminated SAMs were compared with methyl terminated SAMs. The presence of a dense water layer at the SAM surface was found for the hydrophilic SAM. While water molecules are expelled from within the monolayer due to hydrophobic interactions, water molecules were found to form a thick layer in the vicinity of the carboxyl groups. Hydrogen bonds between water and COOH further reduce surface free energy assisting in the formation of a closed packed structure.

These results suggest that a stable 11-MUA SAM can be obtained from solution at different incubation times and that the monolayer does not undergo oxidation. SAMs can undergo oxidation when exposed to air or aqueous solutions [73]. Oxidation of the SAMs due to environmental factors would decrease the R_{ct} measured during EIS since thiolated species would leave the surface under the form of sulfonates or sulfianes leaving behind pinholes which promote electron transfer. This was not observed after 24 hours suggesting that 11-MUA forms stable monolayers on gold SPEs.

In the case of 11-MUA/6-MCH mixed SAM formation, the same incubation time of 18 hours was used in order to make the comparison between the two monolayers more facile. 6-MCH can be used either as a spacer during monolayer formation from ethanolic solution or as a blocking agent, after MAB attachment, from aqueous solution [16], [74]. In this report, 6-MCH was used as a spacer in order to reduce the steric hindrance of the antibodies after surface attachment.

3.4 Biosensor characterization using ferro-/ferricyanide redox couple

3.4.1 11-MUA SAM NGAL-biosensor

EIS was employed to study the electrochemical behaviour of the biosensor at different stages during manufacturing. EIS spectra were acquired either in potassium ferro-/ferricyanide, ferrocenedimethanol or carboxyferrocene aqueous solutions containing 1x PBS. Being able to observe the changes in electrochemical behaviour at each functionalization step provides a vast amount of information about the system. In fig. 3.7 all the functionalization steps on BT electrodes are overlaid and presented as complex impedance plots. The circuit elements values are reported in table 3.4. Each step is compared in terms of charge transfer resistance and effective capacitance. R_{ct} increases from 54 Ω , for the blank electrode, to 317.89 k Ω after 4 hours of incubation in 2mM 11-MUA 80% ethanolic solution. This indicates that a highly insulating SAM forms on the surface of the SPEs. Following chemical activation of the carboxyl-terminal groups, a decrease in impedance can be observed after incubating the electrodes in EDC/NHS activation solution, for 30 minutes. R_{ct} decreases to 25.44 k Ω after this step. The decrease in R_{ct} is believed to be caused by the formation of NHS active esters at the surface of the monolayer, due to the two-step coupling reaction, as showcased in fig. 2.1. This behaviour was studied by Liu et al [75] using EIS and CV measurements. The groups suggested that different reaction intermediates would either hinder or favour the electron transfer process. This behaviour was found to be highly influenced by the redox probes, the activation conditions and the terminal group of the monolayer. The highly insulating behaviour of the SAM comes from the deprotonation of the surface carboxyl groups at measuring conditions (temperature and pH). The ordered nature of the monolayer makes it possible that the electrode surface gets screened by the partial negative charges thus impeding the redox probes from reacting at the surface. This behaviour relies on the type of redox probes used in the experiment. The negatively charged $[\text{Fe}(\text{CN})_6]^{-3/-4}$ ions are repelled from diffusing towards the electrode surface by the $-\text{COO}^-$ terminal groups. The use of EDC without NHS leads to the formation of positively charged O-acylisourea intermediate. The presence of O-acylisourea favours the electron transfer by electrostatic attraction between the charged surface and the redox probes. Liu et al [75] reported a big decrease in impedance when only EDC is used and only a slight decrease when sulfo-NHS is used together with EDC. This small decrease is caused by the sulfonate

functional group which gives the molecule a net negative charge, yet the electron transfer was not impeded as much by the sulfo-NHS ester as by the 11-MUA SAM alone. In this report, the behaviour is somewhat similar to what was observed by this group. The decrease in R_{ct} is caused by the formation of uncharged NHS esters which favour the electron transfer at the surface, yet not as much as the positively charged O-acylisourea. It is actually possible that some O-acylisourea forms during the activation step which further enhances the electron transfer kinetics. Similar behaviour was observed in [68] and [58], yet [76] reported an increase in R_{ct} after this step while also using ferro-/ferricyanide couple as redox reporters. The reverse behaviour is observed if positively charged redox probes or amine-terminated SAMs are used as described in [77].

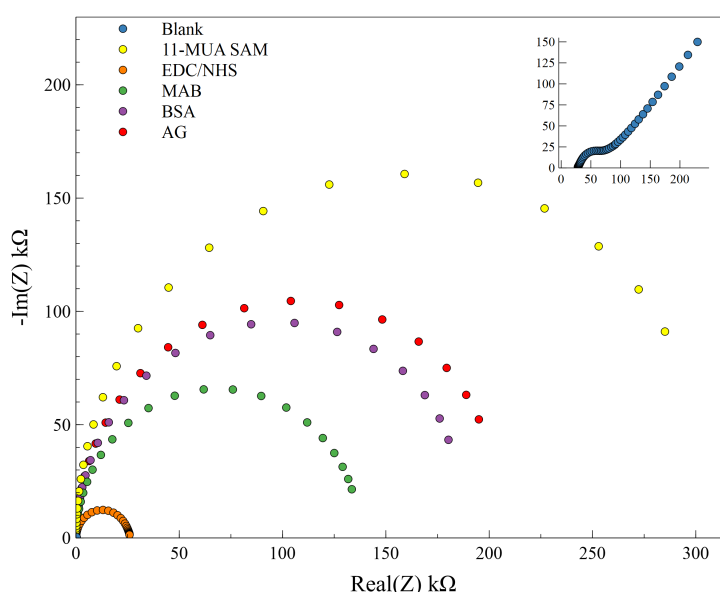


Figure 3.7: Nyquist plots showcasing different steps during BT SPEs functionalization as dots with different colors, blank BT SPE (blue), 11-MUA SAM (yellow), EDC/NHS coupling (orange), MAB attachment (green), BSA blocking (purple), incubation with 100 ng/ml lipocalin-2/NGAL (red). The spectra were obtained in 5mM ferro-/ferricyanide redox couple. AC amplitude: 10 mV (rms). Frequency range $10^5 - 0.1$ Hz.

After surface activation, an increase in R_{ct} is observed at each individual step. The R_{ct} reaches 135.23 k Ω after incubation with anti-NGAL MAB for 1 hour. This increase corresponds to the formation of amide bonds between the activated SAMs and a primary amine on the antibody surface. As antibodies are attached to the electrode surface they further impede the flow of electrons, yet not as much as the 11-MUA SAM. This could be caused by an excess of positive charges on the antibodies surface which attract ferrocyanide ions at the surface of the electrode as opposed to 11-MUA SAMs alone which are highly insulating. Most electrochemical biosensors are developed using short-chained alkanethiols, such as 3-mercaptopropionic acid, which do not hinder charge transfer kinetics nearly as much as a longer alkanethiol molecule. While using shorter alkanethiols an impedance increase is observed after antibody attachment when compared to a bare SAM [17]. In this report the impedance decreases after

EDC/NHS activation only to increase after MAB incubation, however, not exceeding the impedance measured for 11-MUA SAMs alone. This result is in line with [68] and [58] which employed a similar protocol using 11-MUA SAMs.

Table 3.4: Fitting values of the Randles equivalent circuit elements at different stages during the development of the biosensor using ferro-/ferricyanide redox couple.

Functionalization step	$R_{sol}(\Omega)$	$R_{ct}(k\Omega)$	$C_{dl}(\mu F cm^{-2})$
Blank	28	0.054	25.22
11-MUA SAM	24	317.89	3.16
EDC/NHS	25	25.44	3.02
MAB attachment	25.6	135.23	3.1
BSA blocking	24.4	192.01	2.7
AG detection	24.8	215	2.68

An increase in R_{ct} to 192.01 k Ω was measured after incubation with 0.1% BSA. This indicates that BSA was adsorbed at the electrode surface blocking most of the surface unspecific active sites. The electron transfer rate further decreased after incubation with 100 ng/ml lipocalin-2/NGAL for 30 minutes, highlighting that MAB was successfully attached to the monolayer surface and that it maintained its biorecognition ability. R_{ct} increases from 215 k Ω after AG incubation. This is equivalent to a 12% increase in measured R_{ct} .

The double-layer capacitance was also determined at each step. As it can be seen in table 3.4, the capacitance value decreases from 25.22 $\mu F cm^{-2}$, which is representative for a bare gold surface, to 3.16 $\mu F cm^{-2}$ after 11-MUA SAMs formation. The following steps further reduce the capacitance of the system pointing towards an increase in thickness of the dielectric material between electrode and electrolyte. In this case, the dielectric is composed of the SAM, attached MABs, adsorbed BSA and NGAL. This behaviour is representative for an impedance-based immunosensor [76], [78]

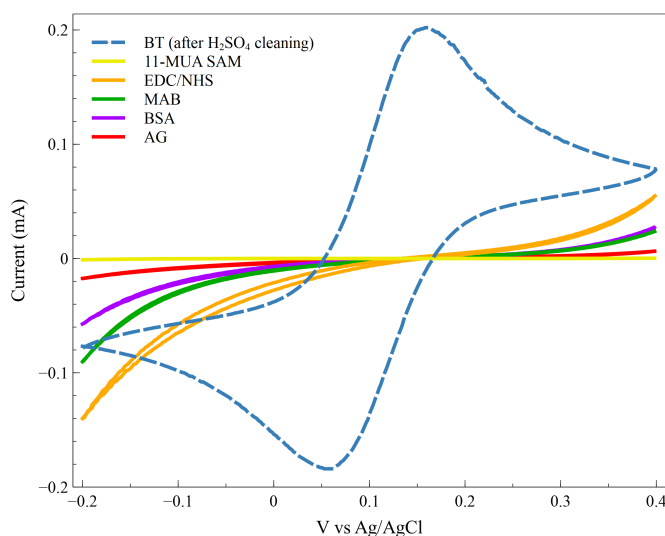


Figure 3.8: CV scans of ferro-/ferricyanide redox couple in 1x PBS on BT electrodes at each functionalization step. Scan rate: 100 mV s^{-1} .

CV scans of BT electrodes at different steps during the development of the biosensor can be seen in fig. 3.8. After 11-MUA SAMs formation no charge is transferred in the interrogated potential range. An increase in current is observed after EDC/NHS activation step yet, no reduction or oxidation peaks are present. Further modification steps similarly decrease the observed current as impedance increases during EIS measurements. This is in agreement with data obtained during EIS experiments.

3.4.2 11-MUA/6-MCH mixed SAM NGAL-biosensor

The same biosensing approach was applied using a mixed alkanethiol SAM. Each step during functionalization is shown in fig. 3.9. The equivalent circuit parameters obtained after fitting the spectra with a Randles equivalent circuit is shown in table 3.5. The behaviour of the mixed SAM biosensor is similar to the one observed for the 11-MUA SAM sensor. The R_{ct} of the mixed SAM was calculated to be $273.89 \text{ k}\Omega$. This is roughly a 16% decrease when compared to 11-MUA SAM. This indeed is representative of an 11-MUA/6-MCH mixed SAM. Since 6-MCH is a shorter molecule than 11-MUA and does not have a bulky carboxyl functional group, an impedance decrease is expected.

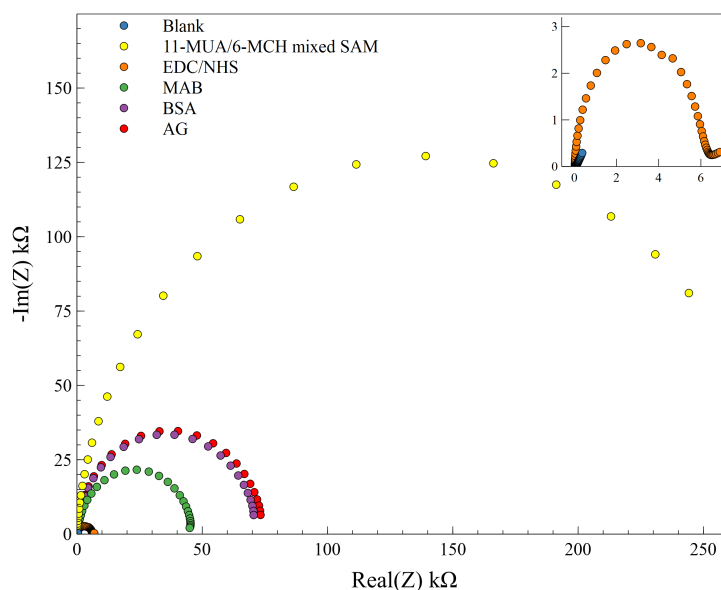


Figure 3.9: Nyquist plots showcasing different steps during BT SPEs functionalization as dots with different colors, blank BT SPE (blue), 11-MUA/6-MCH mixed SAM (yellow), EDC/NHS coupling (orange), MAB attachment (green), BSA blocking (purple), incubation with 100 ng/ml lipocalin-2/NGAL (red). The spectra were obtained in 5mM ferro-/ferricyanide redox couple. AC amplitude: 10 mV (rms). Frequency range $10^5 - 0.1$ Hz.

Each subsequent step follows the same pattern as previously observed on 11-MUA SAMs. The R_{ct} decreases to 5.91 k Ω after EDC/NHS activation reaction. R_{ct} increases to 46 k Ω after MAB attachment and to 71.19 k Ω after BSA blocking. Only a small increase in R_{ct} is observed after incubation with 100 ng/ml NGAL solution. The increase is equal to 3.93 k Ω which translates to a 5.5% change in measured R_{ct} . The increase in R_{ct} after AB-AG complex formation is less than half of the signal measured for 11-MUA SAM biosensor.

The inferior performance of this approach could be attributed to a low number of antibodies attached to the 11-MUA SAM. Since carboxyl functional groups react with primary amines in the MAB structure to form amide bonds during the activation step, a lower -COOH surface coverage translates into fewer crosslinking sites. This could be explained by a low surface coverage of 11-MUA in comparison to 6-MCH. Since both thiols are chemisorbed simultaneously from solution, a competing interaction between 11-MUA and 6-MCH occurs. The chemisorption kinetics are influenced by the length of the molecules, the functional group and the solvent [43]. Since 6-MCH has a shorter alkyl chain, the adsorption rate of 6-MCH is faster and higher surface coverage is expected for this molecule. Nonetheless, the incubation time, solvent to water ratio and alkanethiols concentration can be tuned to obtain a more representative monolayer [79]. It was reported that by introducing different functional groups in a monolayer, the highly ordered structure is disturbed [43]. Another possible adverse effect is the formation of discrete domains instead of mixed layers as stated by A. M. Jonas et al. [80], yet this usually occurs during thiol exchange reaction where chemisorbed species are displaced by different molecules. Steric effects also play an important role during this functionalization step. Several studies proposed equal initial adsorption

for alkanethiols with similar adsorption rates followed by a displacement step that favours smaller molecules with less bulky functional groups [79]. Cecchetto et al. [16] successfully employed such mixed monolayer in an impedimetric biosensing platform for the detection of NS1 protein, a specific dengue biomarker. One key difference between the protocol presented in the literature and the one employed in this report is the solvent. As reported in the paper, anhydrous ethanol was used as a solvent while in this report the SAMs were obtained in a solution containing water and ethanol (1:1 ratio). This could cause a drop in sensitivity since 6-MCH is much more soluble in aqueous solutions as opposed to 11-MUA (2.35 mg/ml for 6-MCH as opposed to 0.011 mg/ml for 11-MUA) [81]. All this would explain the formation of 6-MCH islands with greater coverage than 11-MUA, instead of a mixed alternating layer, thus hindering the surface attachment of MAB.

Table 3.5: Fitting values of the Randles equivalent circuit elements at different stages during the development of the biosensor using ferro-/ferricyanide redox couple.

Functionalization step	$R_{sol}(\Omega)$	$R_{ct}(k\Omega)$	$C_{dl}(\mu F cm^{-2})$
Blank	28	0.054	25.22
11-MUA/6-MCH SAM	25.6	273.89	3.58
EDC/NHS	25	5.91	1.28
MAB attachment	31.6	46.01	2.08
BSA blocking	33.2	71.19	3.2
AG detection	29.57	75.12	3.05

3.4.3 The etching effect of cyanide ions

While each step could be differentiated using potassium ferro-/ferricyanide, two problems were identified when measuring impedance using this redox couple. The first issue is related to surface changes, induced by the use of ferrocyanide solution while the second problem is related to signal stability. When EIS or CV measurements were taken on blank electrodes some type of chemical reactions occurs at the surface of the gold electrode, hindering the monolayer formation. This resulted in a drastic decrease in measured impedance after 11-MUA incubation compared to SAMs obtained on electrodes that never got into contact with the aforementioned solution. Before functionalization, electrodes that were never measured using the redox couple will be further referred to as intact electrodes. Impedance data supporting this claim can be seen in fig. 3.10 where EIS was measured at each functionalization step on a BT SPE which got in contact with ferrocyanide solution before SAM formation. The difference in R_{ct} of 11-MUA and 11-MUA/6-MCH SAMs of intact and ferrocyanide pre-treated electrodes is shown in fig. 3.11. As it can be observed if EIS was performed on blank SPEs before functionalization, using ferro-/ferricyanide redox solution, the SAMs become compromised. In this case, the measured R_{ct} of the monolayer is two orders of magnitude lower when compared to SAMs obtained on gold surfaces that were not reacted with the redox probe solution. This decrease is consistent and is present at each functionalization step. Interesting enough is the fact that the sensor still can detect the antigen presence in this undesirable state.

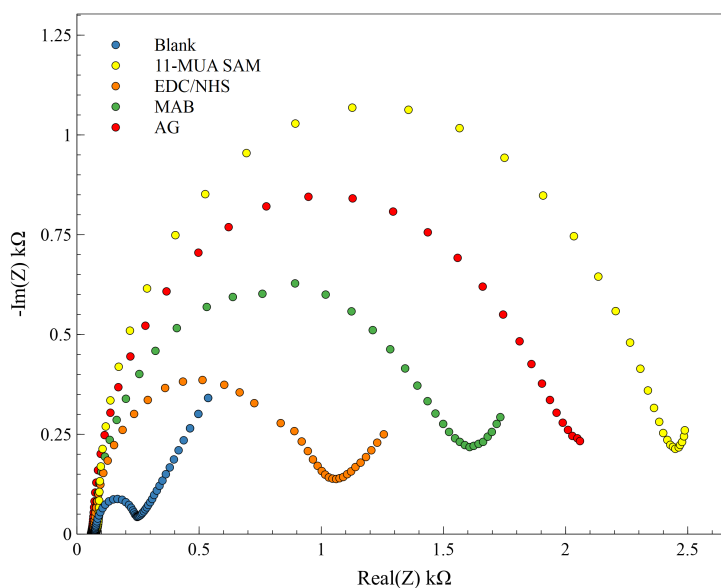


Figure 3.10: Nyquist plots showcasing the effect of ferro-/ferricyanide redox couple on BT SPEs. Different steps during functionalization are shown as coloured dots, blank BT SPE (blue), 11-MUA SAM (yellow), EDC/NHS coupling (orange), MAB attachment (green), incubation with 100 ng/ml lipocalin-2/NGAL (red). The spectra was obtained in 5mM ferro-/ferricyanide redox couple. AC amplitude: 10 mV (rms). Frequency range $10^5 - 0.1$ Hz.

There is not much insight into what chemical reaction causes this behaviour, yet some research focused on this particular problem Vogt et al. [82] studied the stability of ferrocyanide redox couple using as model interaction the hybridization and dehybridization of thiolated DNA. Results obtained from SPR, QCMB and EIS were compared. Some important observation was that any EIS measurement, on blank chips, would hinder the chemisorption of thiol-DNA onto the gold electrode and that signal stability is decreased by CN^- ions through surface etching. Consecutive EIS measurements would give different results while SPR and QCMB measurements showed only small variations. The stability of ferrocyanide probes was studied by Ribeiro et al. [83]. The group reported high RSD (relative standard deviation) values for ferrocyanide due to the surface accumulation of cyanide species.

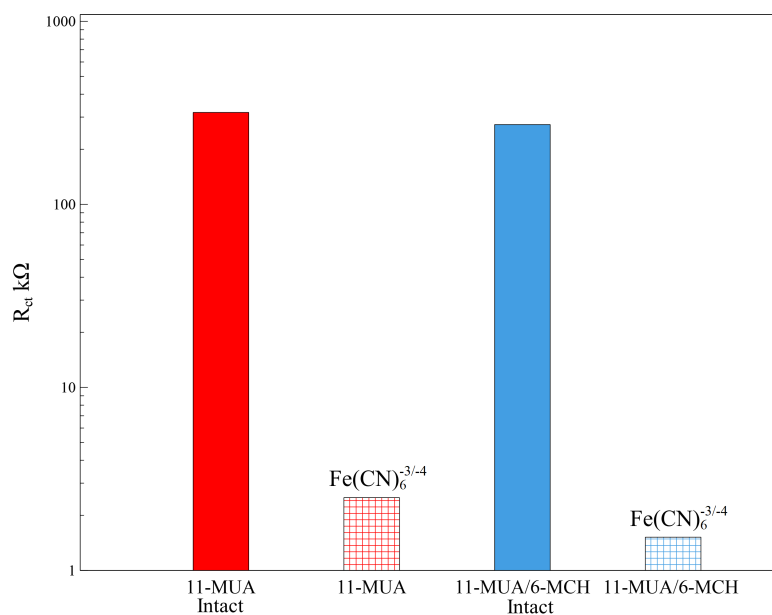
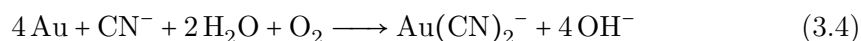


Figure 3.11: Bar charts showcasing the effect of ferro-/ferricyanide redox couple as a function of R_{ct} on 11-MUA SAMs and 11-MUA/6-MCH mixed SAMs. R_{ct} is expressed in a logarithmic scale to make comparison more facile.

The authors stated that CN^- ions formed as an intermediate, during redox reaction would adsorb at the gold surface, initially affecting the gold-thiol chemistry, leading to a decrease in adsorbed thiols. Shortly after, stable cyanide-gold complexes form, over time. The etching occurs when cyanide complexes leave the electrode surface. The etching behaviour is observed as a decrease in R_{ct} after many consecutive measurements. One possible reaction involved in the etching effect is the gold cyanidation reaction, a redox process also called the Elsner reaction shown in eq. (3.4) [82]:



X. Hua et al.[84] suggested that solubilized metallic gold takes part in the redox reaction and associates itself with free CN^- ions under applied external potential. An increase in gold-related chemical species (Au^- , Au_3^+ and $\text{Au}(\text{CN})_2^-$) was observed at 0.8 V, however, small amounts of gold and cyanide ions were also detected under OCP. Based on cumulative association constants of complex Au ions, a five-step model interaction between ferrocyanide and gold ions was proposed. This model suggests that during ferrocyanide oxidation reaction the formation of $\text{Au}(\text{CN})_2^-$ is more favourable due to a higher cumulative constant (stability) than $\text{Fe}(\text{CN})_6^{-4}$. The model suggests that the formation of $\text{Au}(\text{CN})_2^-$ ions is believed to arise from a competition between Au^{3+} , Fe^{2+} and Fe^3 ions. Taking this into account there was not possible to assess the performance of the biosensor using this redox probe. With all the new research focusing on alternative redox probes for electrochemical sensing, better impedimetric biosensors may be developed in the near future. To further assess the characteristics of the NGAL-biosensor, such as linear range, LOD and sensitivity, two ferrocene derivatives, namely ferrocenecarboxylic acid and 1,1'- ferrocenedimethanol were used as redox probes.

3.5 Biosensor characterization using ferrocene derivatives

Similar EIS and CV measurements were carried out using FCA and FDM. This was done in order to increase the reproducibility of the biosensor. Complex impedance plots of 11-MUA modified BT SPEs at different stages during functionalization are shown in fig. 3.12 for FCA and fig. 3.13 for FDM. The fitting results for each set of measurements are shown in table 3.6. Fitting examples and fitting results are also shown in A.3

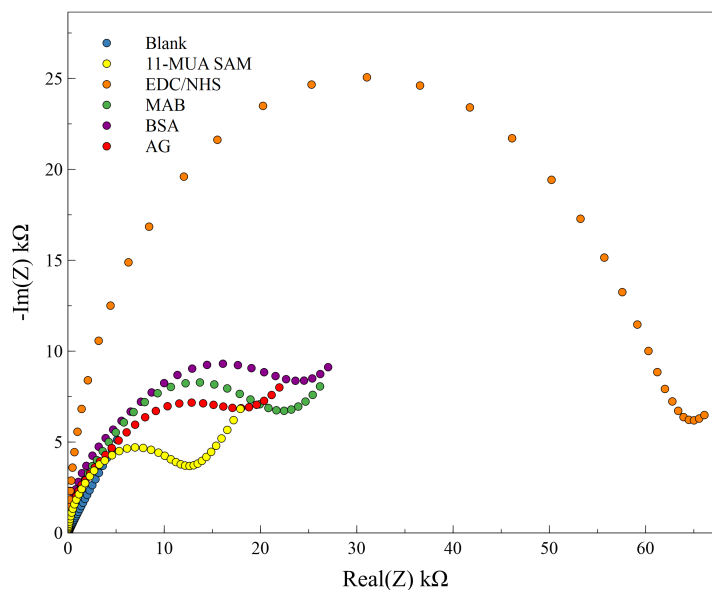


Figure 3.12: Nyquist plots showcasing different steps during BT SPEs functionalization as dots with different colors, blank BT SPE (blue), 11-MUA SAM (yellow), EDC/NHS coupling (orange), MAB attachment (green), BSA blocking (purple), incubation with 100 ng/ml lipocalin-2/NGAL (red). The spectra were obtained in 1mM FCA. AC amplitude: 10 mV (rms). Frequency range $10^5 - 0.1$ Hz.

In the case of both ferrocene redox probes an impedance increase is observed after 11-MUA SAM formation however, the charge transfer resistance of the monolayer is much smaller in this case than when measurements are performed using ferrocyanide. This could be caused by a decrease in electrostatic repulsion between the monolayer and ferrocene derivatives which are not negatively charged as opposed to ferrocyanide ions. During EDC activation reaction, an increase in R_{ct} is observed. This might be caused by the electrostatic repulsion between the positively charged activated surface (O-acylisourea and NHS-esters) and the redox probes. This seems like a plausible explanation since the opposite behaviour was observed for ferrocyanide. After MAB attachment the impedance drops from 62.9 to 22k Ω for FCA measurements and from 12.5 to 4.6 k Ω for FDM measurements. The percentage decrease is similar for EIS measurements using both FDM and FCA and it is around 63-65 % decrease R_{ct} . A small decrease in R_{ct} is observed after BSA blocking for FCA and FDM measurements. R_{ct} decrease from 22.2 to 21.8 k Ω when measuring in FCA and from 4.64 to 4.05 k Ω when measuring in FDM. The decrease could be caused by a change in electrode surface charge. BSA has an isoelectric point of 4.7 which indicates that most of the acidic

residues will be in the deprotonated state, thus BSA has a negative net charge at physiological pH. This will cause a change in oxidation and reduction reaction rates which seem to favour the electron transfer kinetics thus the small decrease in impedance. Regarding the capacitance values shown in table 3.6, a substantial increase is observed after BSA incubation. This could be explained by a change in permittivity with the addition of BSA at the electrode surface. 11-MUA SAMs have been determined to have a dielectric constant in the range of 1.9-2.4 at room temperature [85]. BSA, on the other hand, does not have a constant dielectric value due to its heterogeneous charge distribution. In the case of peptides and proteins, the dielectric constant varies from 6-7 inside the protein and up to 20-30 at the protein surface. Values as high as 40 have also been reported while $\epsilon=4$ is considered an optimal value [86]. This could explain the increase in capacitance after BSA incubation. A small increase was also observed after this step on BT SPEs measured in ferrocyanide solution.

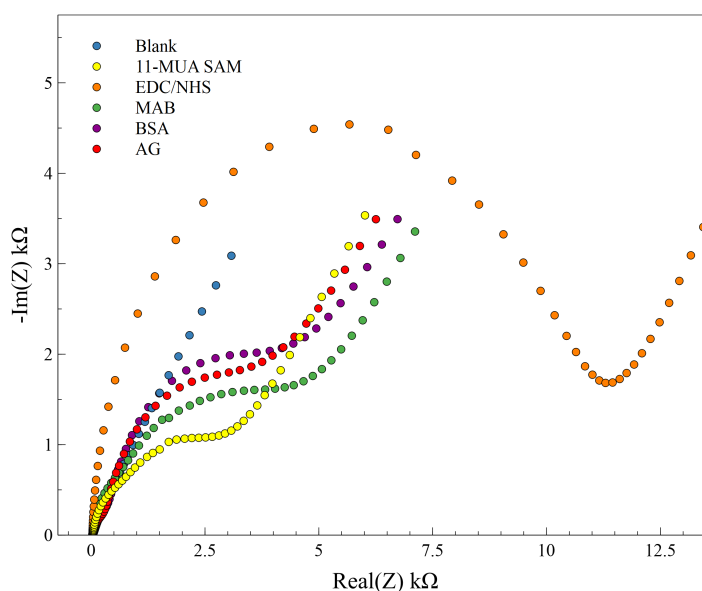


Figure 3.13: Nyquist plots showcasing different steps during BT SPEs functionalization as dots with different colors, blank BT SPE (blue), 11-MUA SAM (yellow), EDC/NHS coupling (orange), MAB attachment (green), BSA blocking (purple), incubation with 100 ng/ml lipocalin-2/NGAL (red). The spectra were obtained in 1mM FDM. AC amplitude: 10 mV (rms). Frequency range $10^5 - 0.1$ Hz.

A decrease in R_{ct} was observed after incubation in 100 ng/ml AG suspension on measurements performed in FMD and FCA solutions. R_{ct} decreases from 21.8 to 17.6 kΩ for BT SPEs measured in FCA and from 4.05 to 3.5 kΩ for measurements performed in FDM. The decrease is equal to -19.2% for FCA and -13.5% for FDM. This behaviour could also be caused by electrostatic interactions between the bound AG and the redox probes, however, an initial hypothesis was that weakly bound BSA gets washed away or desorbs during the last incubation step. To test this assumption a second set of experiments was performed on modified BT SPEs following the same protocol, only omitting the BSA incubation step. EIS measurements of these SPEs are shown in fig. 3.14 for FCA and fig. 3.15 for FDM.

Table 3.6: Fitting values of the Randles equivalent circuit elements at different stages during the development of the biosensor using FCA and FDM.

Functionalization step	$R_{sol}(\Omega)$	$R_{ct}(k\Omega)$	$C_{dl}(\mu F cm^{-2})$
FCA			
Blank	32.76	0.537	17.4
11-MUA SAM	33.99	11.36	5.37
EDC/NHS	33.54	62.92	0.6
MAB attachment	31.6	22.2	4.18
BSA blocking	32.0	21.8	17.6
AG detection	34.57	17.683	16.8
FDM			
Blank	29.2	0.020	14.4
11-MUA SAM	35	2.82	8.8
EDC/NHS	30	12.51	4.4
MAB attachment	29	4.64	9.4
BSA blocking	31.6	4.05	17
AG detection	37.7	3.54	15.8

Fitting values of equivalent circuit elements of BT SPEs at each functionalization step, without BSA blocking, are shown in table 3.7. The same behaviour was observed during these experiments. An initial increase in R_{ct} is seen after 11-MUA monolayer formation. An even greater increase in R_{ct} was measured after the functional carboxyl group activation with EDC/NHS. Following the MAB attachment the measured R_{ct} drops to 29.5 k Ω for FCA measurements and 6.66 k Ω for FDM measurements. After AG incubation the R_{ct} drops to even further to 22.182 k Ω , indicating a decrease of -24.8% for the SPEs measured in FCA. An R_{ct} decrease to 4.75 k Ω which is equivalent to a percentage decrease of -28.6% for the SPEs measured in FDM. This set of experiments were employed to determine if weakly bound BSA could be washed off during the AG incubation step. Since a decrease was measured in the absence of BSA, the change in R_{ct} could be attributed to the MAB-AG complex formation. Another possible explanation that would cause a decrease in R_{ct} is the desorption of the monolayer during the washing step. This hypothesis was not further addressed since no decrease in R_{ct} was observed when ferrocyanide solution was used during EIS measurements. Similar behaviour was reported by M. C. Rodríguez et al. ?? after developing an aptamer-based impedimetric biosensor for the detection of lysozyme. The proposed interaction for the decrease in impedance was the switching of surface charges from negative, in the unbound state, to positive in the bound state. This behaviour arises from the negatively charged phosphate backbone of the aptamer which repels the ferrocyanide ions from reacting at the surface. After the addition of lysozyme, surface charge switching occurs due to a surplus of positive charges in the protein structure. A linear decrease in R_{ct} was reported in 5-25 $\mu g/ml$ range. This could also be the case for the interaction between anti-NGAL MAB and NGAL where the surface charges play an important role in the signal transduction step. This set of experiments were employed to determine if weakly bound BSA could be washed off during the AG incubation step. Since a decrease was measured in the absence of BSA, the change in R_{ct} could be attributed to the MAB-AG complex formation. Another possible explanation that would cause a decrease in R_{ct} is the desorption of the monolayer during the washing step. This hypothesis was not further addressed since no decrease in R_{ct} was observed when ferrocyanide solution was used during EIS measurements. Similar

behaviour was reported by Rodríguez et al. [87] after developing an aptamer-based impedimetric biosensor for the detection of lysozyme. The proposed interaction for the decrease in impedance was the switching of surface charges from negative, in the unbound state, to positive in the bound state. This behaviour arises from the negatively charged phosphate backbone of the aptamer which repels the ferrocyanide ions from reacting at the surface. After the addition of lysozyme, surface charge switching occurs due to a surplus of positive charges in the protein structure. A linear decrease in R_{ct} was reported in 5-25 $\mu\text{g/ml}$ range. This could also be the case for the interaction between anti-NGAL MAB and NGAL where the surface charges play an important role in the magnitude of the recorded signal

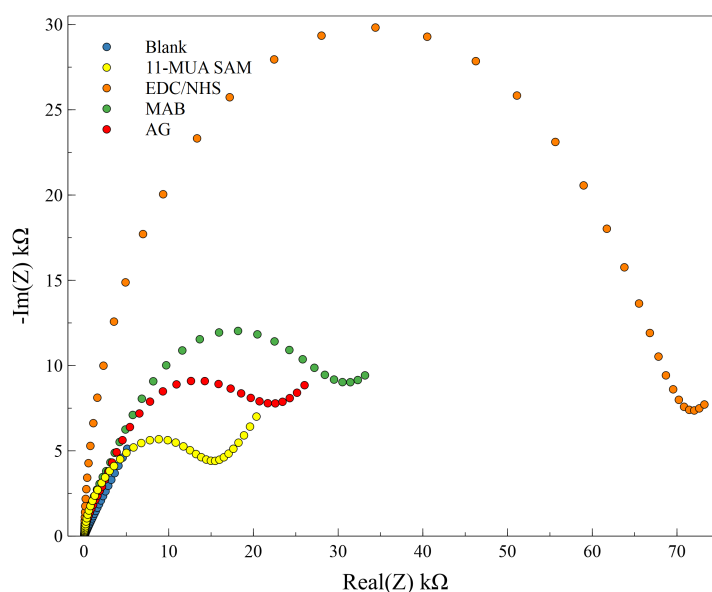


Figure 3.14: Nyquist plots showcasing different steps during BT SPEs functionalization as dots with different colors and omitting the BSA blocking step. Blank BT SPE (blue), 11-MUA SAM (yellow), EDC/NHS coupling (orange), MAB attachment (green), incubation with 100 ng/ml lipocalin-2/NGAL (red). The spectra was obtained in 1mM FAC. AC amplitude: 10 mV (rms). Frequency range $10^5 - 0.1$ Hz.

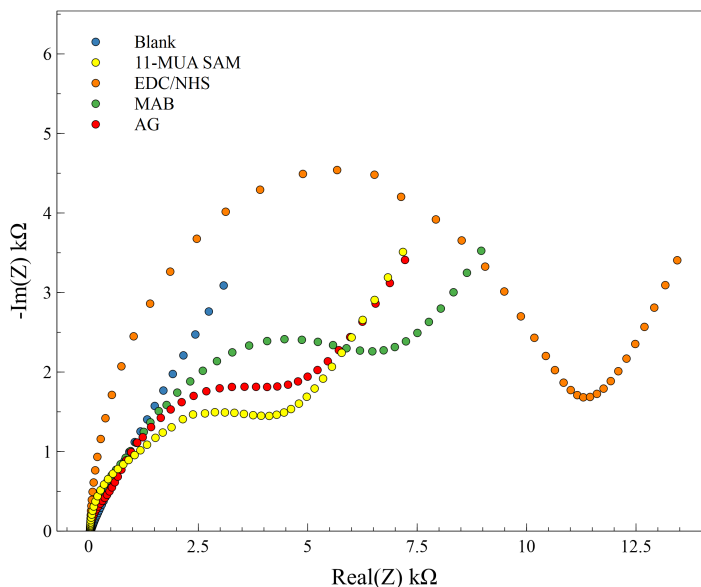


Figure 3.15: Nyquist plots showcasing different steps during BT SPEs functionalization as dots with different colors and omitting the BSA blocking step. Blank BT SPE (blue), 11-MUA SAM (yellow), EDC/NHS coupling (orange), MAB attachment (green), incubation with 100 ng/ml lipocalin-2/NGAL (red). The spectra were obtained in 1mM FDM. AC amplitude: 10 mV (rms). Frequency range $10^5 - 0.1$ Hz.

Table 3.7: Fitting values of the Randles equivalent circuit elements at different stages during the development of the biosensor using FCA and FDM omitting the BSA blocking step.

Functionalization step	$R_{sol}(\Omega)$	$R_{ct}(k\Omega)$	$C_{dl}(\mu F cm^{-2})$
FCA			
Blank	32.76	0.537	17.4
11-MUA SAM	29.17	14.3	5.1
EDC/NHS	33.98	75.9	0.7
MAB attachment	27.05	29.5	5.7
AG detection	27.38	22.182	7.74
FDM			
Blank	29.2	0.020	14.4
11-MUA SAM	27.1	4.2	8
EDC/NHS	30.5	12.11	4.1
MAB attachment	28.5	6.66	11.18
AG detection	27.9	4.75	12.4

CV was also employed to study the functionalization steps and response using FDM. Overlaid CV scans of BT SPEs at different stages during functionalization are shown in fig. 3.16. A decrease in peak current is observed after 11-MUA SAM formation which explains the increase in R_{ct} observed during EIS measurements. The redox peaks

disappear completely after EDC/NHS reaction. This suggests that the amino-reactive NHS-esters intermediates formed during the activation reaction drastically hinder the redox reaction of FDM. This explains the high impedance measured after this step. Following the MAB attachment to the surface, the measured current increased. BSA also seems to have a somewhat blocking effect which is to be expected yet the measured current is similar as before this step, however the peaks seems to have shifted towards a more positive potential. Only a small reduction in the anodic and cathodic currents was observed after AG incubation.

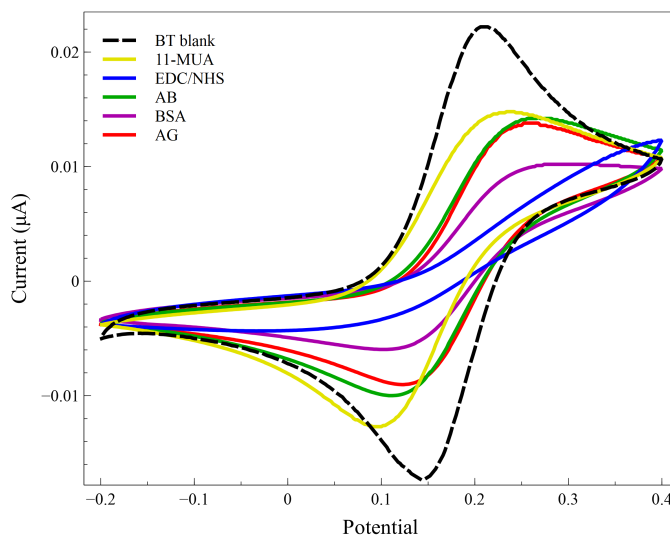


Figure 3.16: CV scans of FDM in 1x PBS on BT electrodes at each functionalization step. Scan rate: 100 mV s^{-1} .

3.6 NGAL-biosensor calibration: LOD and linear-range

The reproducibility, LOD and linear-range of the biosensor were investigated with and without BSA as a blocking agent. Standard curves were obtained including eight NGAL concentrations ranging from 10-800 ng/ml and can be seen in fig. 3.17 and fig. 3.18. Duplicate measurements were performed following the same protocol. The response of the biosensor was calculated as the percentage change in R_{ct} after incubation with a specific concentration of AG. The mean of duplicate experiments was calculated and plotted against the AG concentration to determine the working linear concentration range and LOD. The standard errors (SE) were calculated from the standard deviation of the mean. Small SE values were reported for the biosensor when BSA was not used.

The LOD of the biosensor was determined from the fitted regression curves. LOD was calculated as three times the ratio of signal to noise ($\frac{S}{N} = 3$) as suggested by IUPAC [1]. It was determined that the LOD for the biosensor using BSA as a blocking agent could not be calculated following this protocol, since the biosensor has an apparent response to a blank solution. This would point towards the fact that BSA gets washed away during the AG incubation step or that the MAB-AG complex is hindered by the presence of BSA.

A low detection limit was observed when no BSA was used, at around 18 ng/ml NGAL as it can be seen from fig. 3.18. When looking at both dynamic ranges it can be observed that when BSA is used, the changes in R_{ct} after incubation with consecutive NGAL concentrations are very small. This would indicate a poor performance for the biosensor when BSA is used. For example, a decrease in R_{ct} of -27.7% was observed after incubation with 10 ng/ml NGAL. After incubation with 100 ng/ml, a decrease of -28.5% was measured. The difference in signal between both measurements would be only -0.8% indicating a poor biosensing performance and the possibility that BSA gets washed away during this step. False-positives were observed several times when incubating in blank solution. This would affect the reproducibility of the sensor and the MAB specificity would be hindered. Better results were observed when a second washing step was employed after BSA incubation. During this step, the electrodes were washed in 0.05% Polysorbate 20 1x PBS solution (PBST). This surfactant is used in most common ELISA protocols to wash away any weakly bound or adsorbed macromolecules or blocking agents while also creating a temporary film, blocking the unspecific adsorption sites [88].

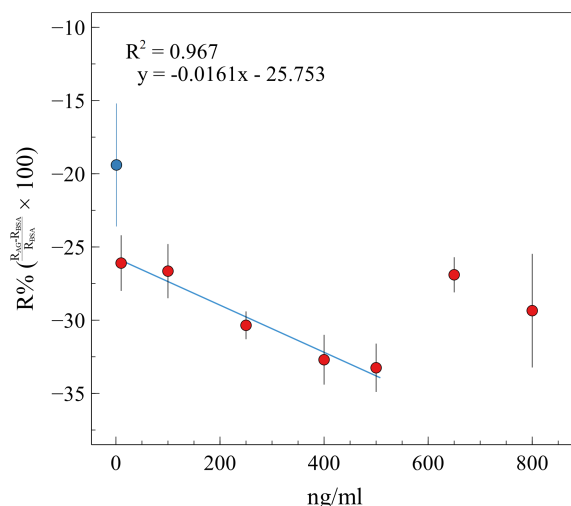


Figure 3.17: Standard curve of anti-NGAL SPEs biosensor. The biosensor response was calculated as the percentage change in R_{ct} after AG incubation. Red dots represent an AG concentration while the blue dot represents the blank response of the sensor. The measured concentration range was 10-800 ng/ml NGAL in 1xPBS. EIS measurements were carried out in FDM.

On the other hand, when no BSA was used, the sensitivity of the biosensor increases and consecutive NGAL concentrations are easier to distinguish. LOQ was also calculated for this sensor at around 24.4 ng/ml. LOQ is used to determine the lowest amount of analyte detected with utmost certainty [8]. Both sensing approaches seem to have an upper detection limit of 500 ng/ml after which linearity is not maintained for measurements carried out in FDM. Sensitivity was determined from the slope of the fitted regression curve. The biosensor has a sensitivity of $-0.0381 R_{ct} \% ng^{-1} ml^{-1}$

Control measurements were also employed for both sensing approaches. A decrease in R_{ct} was observed for the BSA blocked chips even when no AG was present. This indicates that when blocking agents are used the reproducibility and validity of the

experiments is affected. No changes in R_{ct} were observed for chips without BSA when incubated with only PBS. Taking into account the aforementioned observations, the linear range and LOD determined for BSA blocked chips could not be trusted, however better reproducibility and stability are observed without BSA. In turn, assays carried out in complex samples without blocking agents could suffer from false negatives since the specificity of the MAB was not assessed.

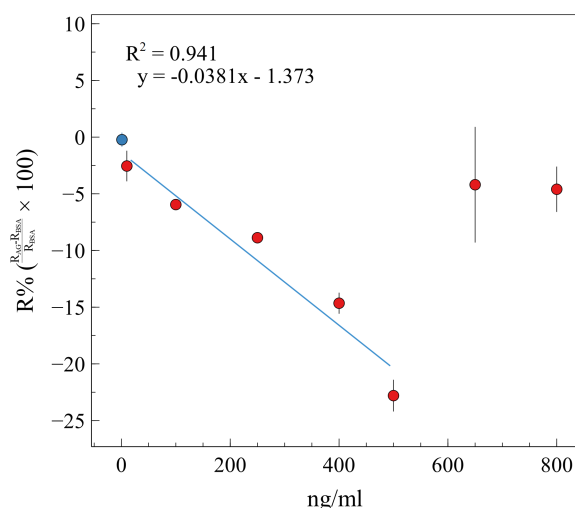


Figure 3.18: Standard curve of anti-NGAL SPEs biosensor, without the BSA blocking step. The biosensor response was calculated as the percentage change in R_{ct} after AG incubation. Red dots represent an AG concentration while the blue dot represents the blank response of the sensor. The measured concentration range was 10-800 ng/ml NGAL in 1xPBS. EIS measurements were carried out in FDM.

Commercially available NGAL detection kits are available with a LOD of 10 ng/ml (Alere Triage NGAL assay) used either as confirmation for acute kidney injury (AKI) or diabetic nephropathy prevention in patients with type 1 diabetes [47]. ELISA kits designed to assess NGAL urine or plasma levels are also available with assay ranges of 10-1000 pg/ml [89]. Neves et al. [49] successfully employed a voltammetric biosensor for the quantitative assessment of NGAL in urine with a LOD of 0.096 ng/ml NGAL and LOQ of 0.321 ng/ml NGAL. The biosensor successfully detected NGAL in urine at 0, 50 and 250 ng/ml. Since AKI is diagnosed in patients with NGAL levels above 100 ng/ml the biosensor is capable of detecting the biomarker at clinically significant levels. The same could be stated for the biosensor developed in this report which has a dynamic linear range between 10-500 ng/ml however it was not tested in NGAL spiked urine or plasma. Cho et al. [47] reported NGAL detection by electrochemical techniques using a similar protocol as in this report. The LOD of 3.93 ng/ml was reported for square wave voltammetry measurements while a lower 1.74 ng/ml LOD was achieved using EIS measurements. All things considered, it is possible that a reproducible and clinically significant NGAL amount can be detected quite fast by electrochemical techniques.

CONCLUSION

The development steps of an affinity-based impedimetric biosensor, based on gold SPEs, were studied by EIS and CV measurements. Two different, gold SPEs were initially proposed and studied as the biosensing platform however only one model was utilized (220 BT SPE) in the end. Out of three cleaning methods tested, potential cycling in H_2SO_4 gave the best results. The anodic oxidation of the pseudo-reference electrode in the presence of KCl was carried out in order to increase the stability and reproducibility of the electrochemical cell. Only a small shift in potential during CV, before and after this step was observed. ECSA and surface roughness was determined for both SPEs.

One critical step during the development process of the biosensor was the monolayer formation from the solution. SPEs are susceptible to being damaged from prolonged contact with organic solvents such as ethanol which was used as a solvent for 11-MUA. To overcome this problem, an optimization step was required. Different incubation times and different ethanol concentrations were tested to find the most suitable conditions for the SPEs without compromising the integrity of the SAM. By using EIS it was observed that an insulating monolayer is formed after 18h in 50% ethanolic solution. The functional carboxyl groups of the SAM were activated to amino-reactive NHS-ester by EDC/NHS chemistry. This enables the covalent attachment of antibodies onto the WE through an amide bond. The potential applications of a mixed 11-MUA/6-MCH SAM were also studied, yet unsatisfactory results were obtained. Each functionalization step was captured by EIS proving that antibodies are successfully attached to the WE surface and that their biorecognition activity was maintained after incubation in NGAL suspension, however, the ferrocyanide redox couple initially employed to study the faradaic behaviour of the biosensor proved to hinder the monolayer formation thus affecting the reproducibility of EIS measurements. To get around this, two ferrocene derivatives, FCA and FDM, were used as redox mediators during EIS and CV. EIS spectra of both FAC and FDM gave further insight into the redox probe interactions with the biofunctionalized electrode. It was proposed that the electrostatic attraction or repulsion between FCA or FDM molecules and surface charges introduced at different stages during functionalization influence the complex impedance spectra. This was suggested to be the cause of the impedance decrease after AG incubation. While ferrocyanide EIS spectra were studied using a modified Randles equivalent circuit, a different circuit arrangement was proposed for FCA and FDM spectra which accommodates the appearance of two semicircle regions in the Nyquist plots. The equivalent circuit proved to offer strong fitting results yet further experimentation is required to fully understand the interfacial reactions that lead to the formation of two RC regions.

Lastly, the biosensing characteristics such as LOD and linearity were determined in duplicates using FDM. A good linear range within clinical relevant values was reported when BSA is not used during the blocking step. The LOD of 18 ng/ml NGAL was obtained. It was suggested that BSA would be washed off during the AG incubation

step and would contribute to the impedance decrease. Further experimentation is required to fully assess the performance of the biosensor.

In summary, it was possible to observe different steps during SPE functionalization using different redox probes. The MAB biorecognition is sustained after surface attachment and linearity was observed when the biosensor was incubated with different NGAL concentrations. This proves that EIS is robust enough for biosensing applications however more detailed insight is required regarding the processes that occur at the WE-solution interface.

FUTURE PERSPECTIVES

Optimization of different functionalization steps proved to be challenging however an increase in biosensing performance could be obtained. Optimization of the MAB coupling procedure such as EDC and NHS concentration or reaction pH could lead to an increase in MAB surface coverage and thus less interference and better signal stability.

Optimization of the assay by using secondary antibodies to increase specificity and decrease the chances of false positives. Different blocking agents could also be tested such as polyethylene glycol or different alkanethiols to cover gaps in the monolayer.

Since BSA blocking proved problematic an optimized protocol regarding BSA concentration, rinsing and the use of surfactants could also be developed.

Testing the response of the biosensor in complex samples such as urine or plasma is imperative for validation purposes. Once an optimized and highly reproducible platform is obtained its performance in real applications scenario has to be validated.

Integration of the sensor in a microfluidic system could provide a faster response to the analyte, continuous detection and POC operation which are a few of the main advantages of electrochemical techniques aside from the low cost of operation.

BIBLIOGRAPHY

- [1] D. R. Thévenot, K. Toth, R. A. Durst, and G. S. Wilson, “Electrochemical biosensors: recommended definitions and classifications: International Union of Pure and Applied Chemistry: Physical Chemistry Division, Commission I.7 (Biophysical Chemistry); Analytical Chemistry Division, Commission V.5 (Electroanalytical Chemistry).1,” *Biosensors and Bioelectronics*, vol. 16, no. 1, pp. 121–131, 2001, ISSN: 0956-5663. DOI: [https://doi.org/10.1016/S0956-5663\(01\)00115-4](https://doi.org/10.1016/S0956-5663(01)00115-4).
- [2] P. Estrela, N. Bhalla, P. Jolly, N. Formisano, and P. Estrela, “Introduction to biosensors,” *Essays in Biochemistry*, vol. 60, no. 1, pp. 1–8, Jun. 2016. DOI: [10.1042/EBC20150001](https://doi.org/10.1042/EBC20150001).
- [3] J. Daniels and N. Pourmand, “Label-free impedance biosensors: Opportunities and challenges,” *Electroanalysis*, vol. 19, no. 12, pp. 1239–1257,
- [4] L. Yang and A. Guiseppi-Elie, *Impedimetric Biosensors for Nano- and Microfluidics*, D. Li, Ed. Springer US, 2008, pp. 811–823, ISBN: 978-0-387-48998-8.
- [5] J. Goode, J. Rushworth, and P. Millner, “Biosensor regeneration: A review of common techniques and outcomes,” *Langmuir : the ACS journal of surfaces and colloids*, vol. 31, Nov. 2014. DOI: [10.1021/la503533g](https://doi.org/10.1021/la503533g).
- [6] G. Gauglitz, “Analytical evaluation of sensor measurements,” *Analytical and Bioanalytical Chemistry*, vol. 410, no. 1, pp. 5–13, 2018, ISSN: 1618-2650. DOI: [10.1007/s00216-017-0624-z](https://doi.org/10.1007/s00216-017-0624-z).
- [7] B. D. Malhotra and M. A. Ali, “Chapter 1 - nanomaterials in biosensors: Fundamentals and applications,” in *Nanomaterials for Biosensors*, ser. Micro and Nano Technologies, B. D. Malhotra and M. A. Ali, Eds., William Andrew Publishing, 2018, pp. 1–74, ISBN: 978-0-323-44923-6.
- [8] D. A. Armbruster and T. Pry, “Limit of blank, limit of detection and limit of quantitation,” *The Clinical biochemist. Reviews*, vol. 29 Suppl 1, no. Suppl 1, S49–S52, 2008, ISSN: 0159-8090.
- [9] I. Palchetti and M. Mascini, “Biosensor technology: A brief history,” P. Malcovati, A. Baschiroto, A. d’Amico, and C. Natale, Eds., pp. 15–23, 2010.
- [10] N. J. Ronkainen, H. B. Halsall, and W. R. Heineman, “Electrochemical biosensors,” *Chem. Soc. Rev.*, vol. 39, pp. 1747–1763, 2010.
- [11] A. P. F. Turner, “Biosensors: Sense and sensibility,” *Chem. Soc. Rev.*, vol. 42, pp. 3184–3196, 2013.
- [12] P. Mehrotra, “Biosensors and their applications – a review,” *Journal of Oral Biology and Craniofacial Research*, vol. 6, no. 2, pp. 153–159, 2016.
- [13] V. Hodnik and G. Anderluh, “Toxin Detection by Surface Plasmon Resonance,” *Sensors*, vol. 9, no. 3, pp. 1339–1354, 2009, ISSN: 1424-8220. DOI: [10.3390/s9031339](https://doi.org/10.3390/s9031339).
- [14] T. Bryan, X. Luo, P. R. Bueno, and J. J. Davis, “An optimised electrochemical biosensor for the label-free detection of c-reactive protein in blood,” *Biosensors*

- and Bioelectronics*, vol. 39, no. 1, pp. 94–98, 2013, ISSN: 0956-5663. DOI: <https://doi.org/10.1016/j.bios.2012.06.051>.
- [15] E. P. Randviir and C. E. Banks, “Electrochemical impedance spectroscopy: An overview of bioanalytical applications,” *Anal. Methods*, vol. 5, pp. 1098–1115, 2013. DOI: [10.1039/C3AY26476A](https://doi.org/10.1039/C3AY26476A).
- [16] J. Cecchetto, F. C. Carvalho, A. Santos, F. C. Fernandes, and P. R. Bueno, “An impedimetric biosensor to test neat serum for dengue diagnosis,” *Sensors and Actuators B: Chemical*, vol. 213, pp. 150–154, 2015, ISSN: 0925-4005. DOI: <https://doi.org/10.1016/j.snb.2015.02.068>.
- [17] M. Braiek, K. Bekir, A. Chrouda, B. Mrabet, A. Bakhrouf, A. Maaref, and N. Jaffrezic-Renault, “An electrochemical immunosensor for detection of staphylococcus aureus bacteria based on immobilization of antibodies on self-assembled monolayers-functionalized gold electrode,” *Biosensors*, vol. 2, pp. 417–26, Oct. 2012. DOI: [10.3390/bios2040417](https://doi.org/10.3390/bios2040417).
- [18] K. Mahato, S. Kumar, A. Srivastava, P. K. Maurya, R. Singh, and P. Chandra, “Chapter 14 - Electrochemical Immunosensors: Fundamentals and Applications in Clinical Diagnostics,” in *Handbook of Immunoassay Technologies*, S. K. Vashist and J. H. Luong, Eds., Academic Press, 2018, pp. 359–414, ISBN: 978-0-12-811762-0. DOI: <https://doi.org/10.1016/B978-0-12-811762-0.00014-1>.
- [19] C. R. Nave, *Hyperphysics*, 2021. [Online]. Available: <http://hyperphysics.phy-astr.gsu.edu/hbase/hframe.html>.
- [20] M. E. Orazem, *Electrochemical impedance spectroscopy*, Hoboken, New Jersey, 2017.
- [21] G. instruments, *Basics of electrochemical impedance spectroscopy*. [Online]. Available: <https://www.gamry.com/application-notes/EIS/basics-of-electrochemical-impedance-spectroscopy/>.
- [22] B.-Y. Chang and S.-M. Park, “Electrochemical impedance spectroscopy,” *Annual Review of Analytical Chemistry*, vol. 3, no. 1, pp. 207–229, 2010. DOI: [10.1146/annurev.anchem.012809.102211](https://doi.org/10.1146/annurev.anchem.012809.102211).
- [23] C. Berggren, B. Bjarnason, and G. Johansson, “Capacitive biosensors,” *Electroanalysis*, vol. 13, no. 3, pp. 173–180, 2001. DOI: [https://doi.org/10.1002/1521-4109\(200103\)13:3<173::AID-ELAN173>3.0.CO;2-B](https://doi.org/10.1002/1521-4109(200103)13:3<173::AID-ELAN173>3.0.CO;2-B).
- [24] M. Li, D.-W. Li, G. Xiu, and Y.-T. Long, “Applications of screen-printed electrodes in current environmental analysis,” *Current Opinion in Electrochemistry*, vol. 3, no. 1, pp. 137–143, 2017, ISSN: 2451-9103. DOI: <https://doi.org/10.1016/j.coelec.2017.08.016>.
- [25] A. A. Karyakin, G. V. Presnova, M. Y. Rubtsova, and A. M. Egorov, “Oriented immobilization of antibodies onto the gold surfaces via their native thiol groups,” *Analytical Chemistry*, vol. 72, no. 16, pp. 3805–3811, 2000. DOI: [10.1021/ac9907890](https://doi.org/10.1021/ac9907890).
- [26] R. O. Kadara, N. Jenkinson, and C. E. Banks, “Characterisation of commercially available electrochemical sensing platforms,” *Sensors and Actuators B: Chemical*, vol. 138, no. 2, pp. 556–562, 2009, ISSN: 0925-4005. DOI: <https://doi.org/10.1016/j.snb.2009.01.044>.
- [27] W. H. Organization, *Diabetes*. [Online]. Available: <https://www.who.int/news-room/fact-sheets/detail/diabetes>.

- [28] “Wearable bioimpedance for continuous and context-aware clinical monitoring,” in *2020 42nd Annual International Conference of the IEEE Engineering in Medicine Biology Society (EMBC)*, 2020, pp. 3985–3988. DOI: 10.1109/EMBC44109.2020.9175298.
- [29] M. H. Jung, K. Namkoong, Y. Lee, Y. Koh, K. Eom, H. Jang, W. Jung, J. Bae, and J. Park, “Wrist-wearable bioelectrical impedance analyzer with miniature electrodes for daily obesity management,” *Scientific Reports*, vol. 11, Jan. 2021. DOI: 10.1038/s41598-020-79667-3.
- [30] W. Azzam, “Self-assembled monolayers on gold made from organothiols containing an oligophenyl-backbone,” Ph.D. dissertation, Ruhr-Universität Bochum, 2003.
- [31] D. Mandler and S. Kraus-Ophir, “Self-assembled monolayers (sams) for electrochemical sensing,” *Journal of Solid State Electrochemistry*, vol. 15, pp. 1535–1558, Jul. 2011. DOI: 10.1007/s10008-011-1493-6.
- [32] K. Tsugimura, H. Ohnuki, H. Wu, H. Endo, D. Tsuya, and M. Izumi, “Oriented antibody immobilization on self-assembled monolayers applied as impedance biosensors,” *Journal of Physics: Conference Series*, vol. 924, p. 012015, Nov. 2017. DOI: 10.1088/1742-6596/924/1/012015.
- [33] A. Karyakin, G. Presnova, M. Rubtsova, and A. Egorov, “Oriented immobilization of antibodies onto the gold surfaces via their native thiol groups,” *Analytical chemistry*, vol. 72, pp. 3805–11, Sep. 2000. DOI: 10.1021/ac9907890.
- [34] C.-S. Chen, K.-N. Chang, Y.-H. Chen, C.-K. Lee, B. Lee, and A. Lee, “Development of a label-free impedance biosensor for detection of antibody–antigen interactions based on a novel conductive linker,” *Biosensors bioelectronics*, vol. 26, pp. 3072–6, Feb. 2011. DOI: 10.1016/j.bios.2010.11.051.
- [35] B. C. Rocha, S. Paul, and H. Vashisth, “Role of entropy in colloidal self-assembly,” *Entropy*, vol. 22, no. 8, 2020, ISSN: 1099-4300.
- [36] K. Baek, I. Hwang, I. Roy, D. Shetty, and K. Kim, “Self-assembly of nanostructured materials through irreversible covalent bond formation,” *Accounts of Chemical Research*, vol. 48, pp. 2221–2229, Apr. 2015. DOI: 10.1021/acs.accounts.5b00067.
- [37] E. Barry and Z. Dogic, “Entropy driven self-assembly of nonamphiphilic colloidal membranes,” *Proceedings of the National Academy of Sciences*, vol. 107, no. 23, pp. 10348–10353, 2010, ISSN: 0027-8424. DOI: 10.1073/pnas.1000406107.
- [38] J. Kim, “Investigations of thiolated self-assembled monolayers on gold substrates by ftir with specular reflectance,” *Pike technologies*,
- [39] R. W. Corkery, “Langmuir blodgett (lb) multilayer films,” *Langmuir*, vol. 13, no. 14, pp. 3591–3594, 1997. DOI: 10.1021/la9701743.
- [40] N. instruments, *Langmuir films*. [Online]. Available: <https://www.nanoscience.com/techniques/langmuir-films/>.
- [41] M. Cohen-Atiya and D. Mandler, “Studying thiol adsorption on Au, Ag and HgI surfaces by potentiometric measurements,” *Journal of Electroanalytical Chemistry*, vol. 550-551, pp. 267–276, 2003, Thin Organic Films, ISSN: 1572-6657. DOI: [https://doi.org/10.1016/S0022-0728\(02\)01145-2](https://doi.org/10.1016/S0022-0728(02)01145-2).

- [42] C. Vericat, M. E. Vela, G. Benitez, P. Carro, and R. C. Salvarezza, "Self-assembled monolayers of thiols and dithiols on gold: New challenges for a well-known system," *Chem. Soc. Rev.*, vol. 39, pp. 1805–1834, 2010. DOI: 10.1039/B907301A.
- [43] A. Ulman, "Formation and structure of self-assembled monolayers," *Chemical Reviews*, vol. 96, no. 4, pp. 1533–1554, 1996. DOI: 10.1021/cr9502357.
- [44] D. Schwartz, "Mechanism and kinetics of self assembled monolayer formation," *Annual review of physical chemistry*, vol. 52, pp. 107–37, Feb. 2001. DOI: 10.1146/annurev.physchem.52.1.107.
- [45] J. Liu, B. Schüpbach, A. Bashir, O. Shekhah, A. Nefedov, M. Kind, A. Terfort, and C. Wöll, "Structural characterization of self-assembled monolayers of pyridine-terminated thiolates on gold," *Phys. Chem. Chem. Phys.*, vol. 12, pp. 4459–4472, 2010. DOI: 10.1039/B924246P.
- [46] C. D. Bain, E. B. Troughton, Y. T. Tao, J. Evall, G. M. Whitesides, and R. G. Nuzzo, "Formation of monolayer films by the spontaneous assembly of organic thiols from solution onto gold," *Journal of the American Chemical Society*, vol. 111, no. 1, pp. 321–335, 1989. DOI: 10.1021/ja00183a049.
- [47] C. H. Cho, J. H. Kim, D.-K. Song, T. J. Park, and J. P. Park, "An affinity peptide-incorporated electrochemical biosensor for the detection of neutrophil gelatinase-associated lipocalin," *Biosensors and Bioelectronics*, vol. 142, 2019, ISSN: 0956-5663. DOI: <https://doi.org/10.1016/j.bios.2019.111482>.
- [48] K. M. Schmidt-Ott, "Neutrophil gelatinase-associated lipocalin as a biomarker of acute kidney injury—where do we stand today?" *Nephrology Dialysis Transplantation*, vol. 26, no. 3, pp. 762–764, Mar. 2011, ISSN: 0931-0509. DOI: 10.1093/ndt/gfr006.
- [49] M. Neves, H. Nouws, A. Santos-Silva, and C. Delerue-Matos, "Neutrophil gelatinase-associated lipocalin detection using a sensitive electrochemical immunosensing approach," *Sensors and Actuators B: Chemical*, vol. 304, p. 127 285, 2020, ISSN: 0925-4005. DOI: <https://doi.org/10.1016/j.snb.2019.127285>.
- [50] P. Danvirutai, M. Ekpanyapong, A. Tuantranont, E. Bohez, S. Anutrakulchai, A. Wisitsoraat, and C. Srichan, "Ultra-sensitive and label-free neutrophil gelatinase-associated lipocalin electrochemical sensor using gold nanoparticles decorated 3d graphene foam towards acute kidney injury detection," *Sensing and Bio-Sensing Research*, vol. 30, p. 100 380, 2020, ISSN: 2214-1804. DOI: <https://doi.org/10.1016/j.sbsr.2020.100380>.
- [51] A. Butterworth, E. Blues, P. Williamson, M. Cardona, L. Gray, and D. Corrigan, "SAMComposition and Electrode Roughness Affect Performance of a DNA Biosensor for Antibiotic Resistance," *Biosensors*, vol. 9, p. 22, Feb. 2019. DOI: 10.3390/bios9010022.
- [52] V. Lacour, K. Moumanis, W. M. Hassen, C. Elie-Caille, T. Leblois, and J. J. Dubowski, "Formation Kinetics of Mixed Self-Assembled Monolayers of Alkanethiols on GaAs(100)," *Langmuir*, vol. 35, no. 13, pp. 4415–4427, 2019. DOI: 10.1021/acs.langmuir.7b00929.
- [53] Z. Grabarek and J. Gergely, "Zero-length crosslinking procedure with the use of active esters," *Analytical Biochemistry*, vol. 185, no. 1, pp. 131–135, 1990, ISSN: 0003-2697. DOI: [https://doi.org/10.1016/0003-2697\(90\)90267-D](https://doi.org/10.1016/0003-2697(90)90267-D).

- [54] A. Lomant and G. Fairbanks, "Chemical probes of extended biological structures: Synthesis and properties of the cleavable protein cross-linking reagent [35s]dithiobis(succinimidyl propionate)," *Journal of Molecular Biology*, vol. 104, no. 1, pp. 243–261, 1976, ISSN: 0022-2836. DOI: [https://doi.org/10.1016/0022-2836\(76\)90011-5](https://doi.org/10.1016/0022-2836(76)90011-5).
- [55] H. Mojarradi, "Coupling of substances containing a primary amine to hyaluronan via carbodiimide-mediated amidation," Ph.D. dissertation, Uppsala Universitet, 2010.
- [56] M. A. Gilles, A. Q. Hudson, and C. Borders, "Stability of water-soluble carbodiimides in aqueous solution," *Analytical Biochemistry*, vol. 184, no. 2, pp. 244–248, 1990, ISSN: 0003-2697. DOI: [https://doi.org/10.1016/0003-2697\(90\)90675-Y](https://doi.org/10.1016/0003-2697(90)90675-Y).
- [57] P.-H. Lin and B.-R. Li, "Antifouling strategies in advanced electrochemical sensors and biosensors," *Analyst*, vol. 145, pp. 1110–1120, 2020. DOI: 10.1039/C9AN02017A.
- [58] Y. Huang, M. C. Bell, and I. I. Suni, "Impedance biosensor for peanut protein ara h 1," *Analytical Chemistry*, vol. 80, no. 23, pp. 9157–9161, 2008. DOI: 10.1021/ac801048g.
- [59] A. Santos, "Fundamentals and applications of impedimetric and redox capacitive biosensors," *Journal of Analytical Bioanalytical Techniques*, vol. S7, Jan. 2014. DOI: 10.4172/2155-9872.S7-016.
- [60] J. Tkac, T. Bertók, L. Lorencova, E. Chocholova, E. Jane, A. Vikartovská, and P. Kasák, "Electrochemical impedance spectroscopy-based biosensors: Mechanistic principles, analytical examples for assay of protein cancer biomarkers and challenges towards commercialization," *ChemElectroChem*, vol. 6, Sep. 2018. DOI: 10.1002/ce1c.201800848.
- [61] S. Chandra, N. Barola, and D. Bahadur, "Biosensor for early detection of cervical cancer," *Chemical communications (Cambridge, England)*, vol. 47, pp. 11258–60, Sep. 2011. DOI: 10.1039/c1cc14547a.
- [62] L. Fischer, M. Tenje, A. Heiskanen, N. Masuda, J. Castillo-Leon, A. Bentien, J. Emnéus, M. Jakobsen, and A. Boisen, "Gold cleaning methods for electrochemical detection applications," *Microelectronic Engineering*, vol. 86, pp. 1282–1285, Apr. 2009. DOI: 10.1016/j.mee.2008.11.045.
- [63] J. A. Ribeiro, E. Silva, P. S. Moreira, and C. M. Pereira, "Electrochemical characterization of redox probes at gold screen-printed electrodes: Efforts towards signal stability," *ChemistrySelect*, vol. 5, no. 17, pp. 5041–5048, 2020. DOI: <https://doi.org/10.1002/slct.202001411>.
- [64] R. Carvalhal, R. Sanches-Freire, and L. Kubota, "Polycrystalline gold electrodes: A comparative study of pretreatment procedures used for cleaning and thiol self-assembly monolayer formation," *Electroanalysis*, vol. 17, no. 14, pp. 1251–1259, 2005. DOI: <https://doi.org/10.1002/elan.200403224>.
- [65] R. S. Nicholson and I. Shain, "Theory of stationary electrode polarography. single scan and cyclic methods applied to reversible, irreversible, and kinetic systems.," *Analytical Chemistry*, vol. 36, no. 4, pp. 706–723, 1964. DOI: 10.1021/ac60210a007.
- [66] M. P. Siswana, K. I. Ozoemena, and T. Nyokong, "Electrocatalysis of asulam on cobalt phthalocyanine modified multi-walled carbon nanotubes immobilized

- on a basal plane pyrolytic graphite electrode,” *Electrochimica Acta*, vol. 52, no. 1, pp. 114–122, 2006, ISSN: 0013-4686. DOI: <https://doi.org/10.1016/j.electacta.2006.03.090>.
- [67] E. Cossar, M. S. Houache, Z. Zhang, and E. A. Baranova, “Comparison of electrochemical active surface area methods for various nickel nanostructures,” *Journal of Electroanalytical Chemistry*, vol. 870, p. 114246, 2020, ISSN: 1572-6657. DOI: <https://doi.org/10.1016/j.jelechem.2020.114246>.
- [68] E. Bahadır and M. Sezgintürk, “A comparative study of short chain and long chain mercapto acids used in biosensor fabrication: A VEGF-R1-based immunosensor as a model system,” *Artificial Cells, Nanomedicine, and Biotechnology*, vol. 44, Oct. 2014. DOI: [10.3109/21691401.2014.962743](https://doi.org/10.3109/21691401.2014.962743).
- [69] R. Mendes, R. Freire, C. Fonseca, S. Neves, and L. Kubota, “Characterization of self-assembled thiols monolayers on gold surface by electrochemical impedance spectroscopy,” *Journal of The Brazilian Chemical Society - JBCS*, vol. 15, Nov. 2004. DOI: [10.1590/S0103-50532004000600011](https://doi.org/10.1590/S0103-50532004000600011).
- [70] S. Campuzano, M. Pedrero, C. Montemayor, E. Fatás, and J. M. Pingarrón, “Characterization of alkanethiol-self-assembled monolayers-modified gold electrodes by electrochemical impedance spectroscopy,” *Journal of Electroanalytical Chemistry*, vol. 586, no. 1, pp. 112–121, 2006, ISSN: 1572-6657. DOI: <https://doi.org/10.1016/j.jelechem.2005.09.007>.
- [71] S. Ansar, S. Chakraborty, and C. Kitchens, “pH-Responsive Mercaptoundecanoic Acid Functionalized Gold Nanoparticles and Applications in Catalysis,” *Nanomaterials*, vol. 8, p. 339, May 2018. DOI: [10.3390/nano8050339](https://doi.org/10.3390/nano8050339).
- [72] E. Li, Z. Du, and S. Yuan, “Properties of a water layer on hydrophilic and hydrophobic self-assembled monolayer surfaces: A molecular dynamics study,” *Science China Chemistry*, vol. 56, Jun. 2013. DOI: [10.1007/s11426-013-4835-7](https://doi.org/10.1007/s11426-013-4835-7).
- [73] J. Maciel, M. C. Martins, and M. Barbosa, “The stability of self-assembled monolayers with time and under biological conditions,” *Journal of biomedical materials research. Part A*, vol. 94, pp. 833–43, Sep. 2010. DOI: [10.1002/jbm.a.32746](https://doi.org/10.1002/jbm.a.32746).
- [74] I. Ciani, H. Schulze, D. K. Corrigan, G. Henihan, G. Giraud, J. G. Terry, A. J. Walton, R. Pethig, P. Ghazal, J. Crain, C. J. Campbell, T. T. Bachmann, and A. R. Mount, “Development of immunosensors for direct detection of three wound infection biomarkers at point of care using electrochemical impedance spectroscopy,” *Biosensors and Bioelectronics*, vol. 31, no. 1, pp. 413–418, 2012, ISSN: 0956-5663. DOI: <https://doi.org/10.1016/j.bios.2011.11.004>.
- [75] L. Liu, D. Deng, Y. Xing, S. Li, B. Yuan, J. Chen, and N. Xia, “Activity analysis of the carbodiimide-mediated amine coupling reaction on self-assembled monolayers by cyclic voltammetry,” *Electrochimica Acta*, vol. 89, pp. 616–622, 2013, ISSN: 0013-4686. DOI: <https://doi.org/10.1016/j.electacta.2012.11.049>.
- [76] A. Ahmad and E. Moore, “Electrochemical immunosensor modified with self-assembled monolayer of 11-mercaptoundecanoic acid on gold electrodes for detection of benzo[a]pyrene in water,” *The Analyst*, vol. 137, Oct. 2012. DOI: [10.1039/c2an35236b](https://doi.org/10.1039/c2an35236b).
- [77] G.-Z. Garyfallou, O. Ketebu, S. Şahin, E. B. Mukaetova-Ladinska, M. Catt, and E. H. Yu, “Electrochemical detection of plasma immunoglobulin as a biomarker

- for alzheimer's disease," *Sensors*, vol. 17, no. 11, 2017, ISSN: 1424-8220. DOI: 10.3390/s17112464.
- [78] A. Qureshi, J. H. Niazi, S. Kallemudi, and Y. Gurbuz, "Label-free capacitive biosensor for sensitive detection of multiple biomarkers using gold interdigitated capacitor arrays," *Biosensors and Bioelectronics*, vol. 25, no. 10, pp. 2318–2323, 2010, ISSN: 0956-5663. DOI: <https://doi.org/10.1016/j.bios.2010.03.018>.
- [79] L. Srisombat, A. C. Jamison, and T. R. Lee, "Stability: A key issue for self-assembled monolayers on gold as thin-film coatings and nanoparticle protectants," *Colloids and Surfaces A: Physicochemical and Engineering Aspects*, vol. 390, no. 1, pp. 1–19, 2011, ISSN: 0927-7757. DOI: <https://doi.org/10.1016/j.colsurfa.2011.09.020>.
- [80] G. Baralia, A.-S. Duwez, B. Nysten, and A. Jonas, "Kinetics of exchange of alkanethiol monolayers self-assembled on polycrystalline gold," *Langmuir*, vol. 21, pp. 6825–6829, Aug. 2005. DOI: 10.1021/1a050245v.
- [81] I. Tetko, J. Gasteiger, R. Todeschini, A. Mauri, D. Livingstone, P. Ertl, V. Palyulin, E. Radchenko, N. Zefirov, A. Makarenko, V. Tanchuk, and V. Prokopenko, "Virtual computational chemistry laboratory – design and description," *Journal of computer-aided molecular design*, vol. 19, pp. 453–463, Jul. 2005. DOI: 10.1007/s10822-005-8694-y.
- [82] S. Vogt, Q. Su, C. Gutierrez-Sanchez, and G. Nöll, "A critical view on electrochemical impedance spectroscopy (eis) using the ferri/ferrocyanide redox couple at gold electrodes," *Analytical chemistry*, vol. 88, Mar. 2016. DOI: 10.1021/acs.analchem.5b04814.
- [83] J. A. Ribeiro, E. Silva, P. S. Moreira, and C. M. Pereira, "Electrochemical characterization of redox probes at gold screen-printed electrodes: Efforts towards signal stability," *ChemistrySelect*, vol. 5, no. 17, pp. 5041–5048, 2020. DOI: <https://doi.org/10.1002/slct.202001411>.
- [84] X. Hua, H.-L. Xia, and Y.-T. Long, "Revisiting a classical redox process on a gold electrode by operando ToF-SIMS: where does the gold go?" *Chem. Sci.*, vol. 10, pp. 6215–6219, 2019. DOI: 10.1039/C9SC00956F.
- [85] F. Damos, R. Luz, and L. Kubota, "Determination of thickness, dielectric constant of thiol films, and kinetics of adsorption using surface plasmon resonance," *Langmuir : the ACS journal of surfaces and colloids*, vol. 21, pp. 602–9, Feb. 2005. DOI: 10.1021/1a0487038.
- [86] L. Li, C. Li, Z. Zhang, and E. Alexov, "On the dielectric "constant" of proteins: Smooth dielectric function for macromolecular modeling and its implementation in delphi," *Journal of chemical theory and computation*, vol. 9, pp. 2126–2136, Apr. 2013. DOI: 10.1021/ct400065j.
- [87] M. C. Rodríguez, A.-N. Kawde, and J. Wang, "Aptamer biosensor for label-free impedance spectroscopy detection of proteins based on recognition-induced switching of the surface charge," *Chemical communications (Cambridge, England)*, vol. 14, pp. 4267–9, Oct. 2005. DOI: 10.1039/b506571b.
- [88] M. Steinitz, "Quantitation of the Blocking Effect of Tween 20 and Bovine Serum Albumin in ELISA Microwells," *Analytical Biochemistry*, vol. 282, no. 2, pp. 232–238, 2000, ISSN: 0003-2697. DOI: <https://doi.org/10.1006/abio.2000.4602>.
- [89] T. F. Scientific, *Ngal human elisa kit*. [Online]. Available: <https://www.thermofisher.com/elisa/product/NGAL-Human-ELISA-Kit/KIT036>.

APPENDIX

A.1 Rationalization of complex numbers

For a given pair of complex numbers $a = a_r + ja_j$ and $b = b_r + jb_j$ which are ordered pairs of real and imaginary numbers (a,b) proposing a solution to a problem which no real number can satisfy with the complex conjugates $\bar{a} = a_r - ja_j$ and $\bar{b} = b_r - jb_j$, have the following relationships:

$$\begin{aligned}
 a + b &= b + a \\
 ab &= ba \\
 x(a + b) &= xa + xb \\
 x(ab) &= (xa)b \\
 a + b &= (a_r + b_r) + j(a_j + b_j) \\
 a - b &= (a_r - b_r) + j(a_j - b_j) \\
 ab &= (a_r b_r - a_j b_j) + j(a_r b_j + a_j b_r) \\
 a\bar{a} &= a_r^2 + a_j^2 \\
 \frac{a}{b} &= \frac{a\bar{b}}{b\bar{b}} = \frac{(a_r b_r + a_j b_j) + j(a_r b_j - a_j b_r)}{b_r^2 + b_j^2}
 \end{aligned} \tag{A.1}$$

A.2 Chloridization of the pseudo-reference silver electrode

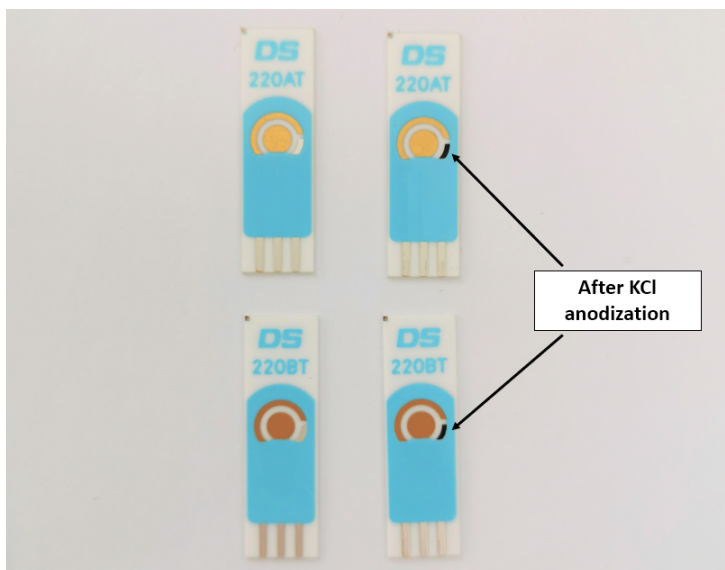


Figure A.1: The pseudo-reference silver electrode before and after anodic oxidation in the presence of 1M KCl. The changes include the formation of a black coloured layer on the surface of the electrode.

A.3 Equivalent circuits and data fitting

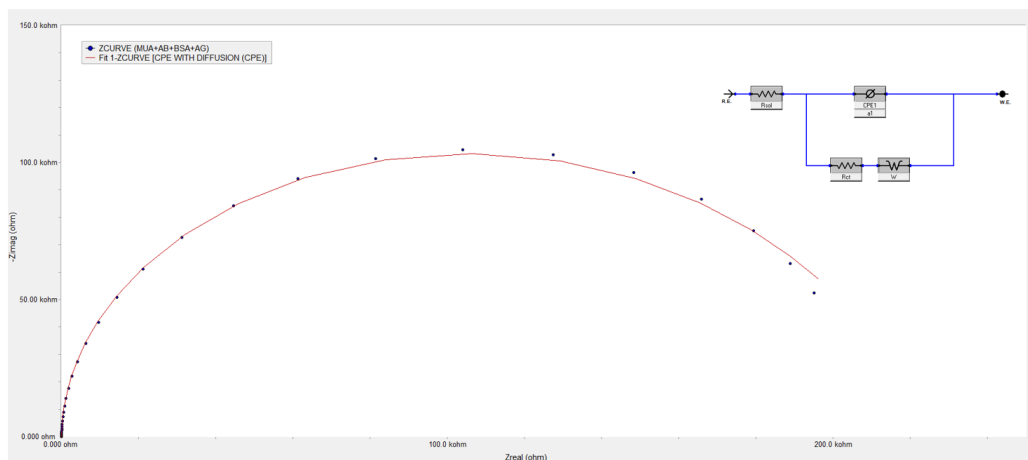


Figure A.2: EIS data fitting using a Randles modified circuit with mixed kinetics and charge transfer control. Nyquist plot of a modified BT SPE. Measurements were carried out in 5mM ferro-/ferricyanide redox couple solution.

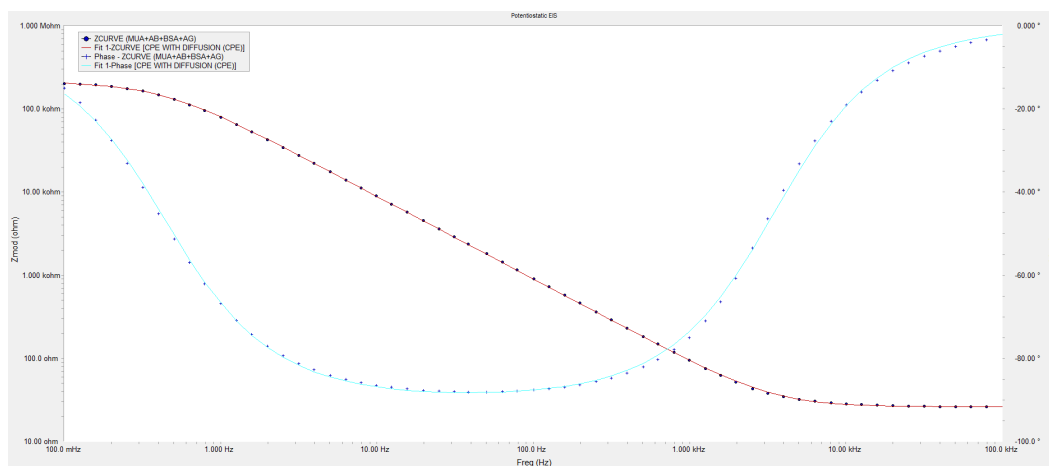


Figure A.3: Bode plot of a modified BT SPE showcasing the change in phase angle at high to mid frequencies and the change in impedance modulus. Measurements were carried out in 5mM ferro-/ferricyanide redox couple solution.

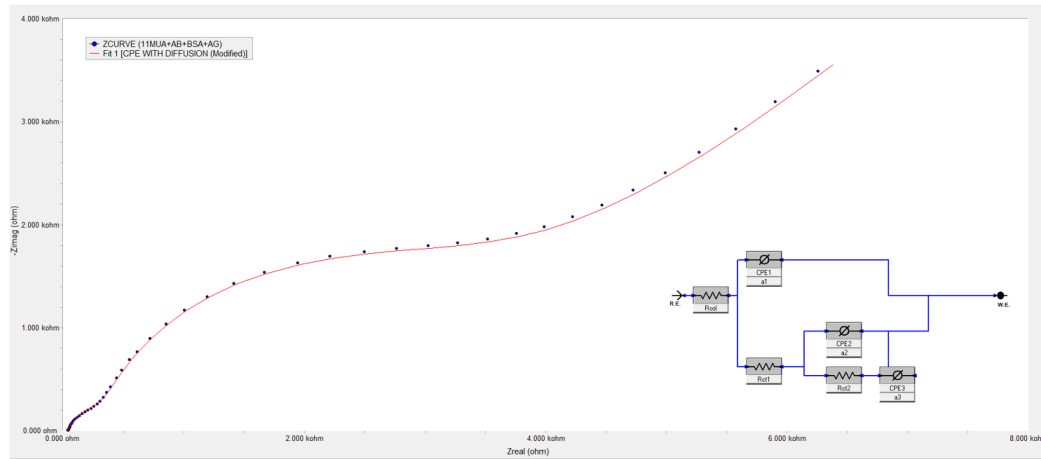


Figure A.4: EIS data fitting using a Randles modified circuit with two RC time constants (double layer and monolayer capacitance). Nyquist plot of a modified BT SPE. Measurements were carried out in 1mM FDM electrolyte solution.

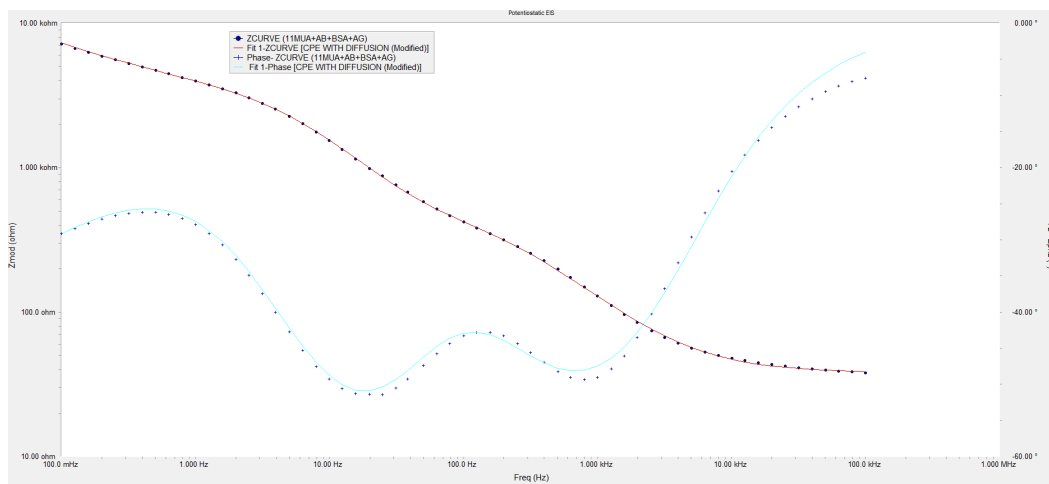


Figure A.5: Bode plot of a modified BT SPE showcasing the change in phase angle at high and low frequencies indicating a parallel or series arrangement of two RC circuits and the change in impedance modulus. Measurements were carried out in 1mM FDM electrolyte solution.